

Dynamic Finite Element Modeling and Analysis of Blast-resistant Sandwich Structures

Linhui Zhang, Ph.D.

University of Connecticut, 2012

Blast-resistant composites and structures are gaining more and more academic and industrial interests currently. The metal sandwich structure is proven to perform better than the monolithic plate with the same mass under blast loading. Besides, the foam or foam-like cores with stacking of graded layers can further mitigate the blast effects. In this work, the dynamic responses of corrugated sandwich plates with various homogeneous and graded core arrangements under shock tube loading are investigated by finite element method. By comparing the maximum back face deflection, maximum back face velocity, plastic energy absorption, stress history and contact force, the corrugated sandwich plate with the gradually graded core has a better overall performance.

The parametric study on unit-cell corrugated and trapezoid sandwich structures with given mass and various core arrangements subjected to idealized air-blast loading is also carried out. The sandwich structures with graded cores can prevent the structure to get fully crushed. It is also shown that the trapezoid sandwich structures have larger impact tolerance, but the trapezoid sandwich structures are more sensitive to the initial geometric imperfections than corrugated sandwich structures.

Due to the benefits of the graded cores, a modified rule of mixture and linear strain-rate dependence are used to derive the rate-dependent elastic-plastic constitutive relation for functionally graded (FG) material. The derived constitutive relations are implemented in ABAQUS/Explicit through a VUMAT subroutine to simulate the dynamic response of a FG plate subjected to shock tube loading.

Dynamic Finite Element Modeling and Analysis of Blast-resistant Sandwich Structures

Linhui Zhang

B.E., Tongji University, 2007

M.S., University of Connecticut, 2010

A Dissertation

Submitted in Partial Fulfillment of the

Requirements for the Degree of

Doctor of Philosophy

at the

University of Connecticut

2012

UMI Number: 3533976

All rights reserved

INFORMATION TO ALL USERS

The quality of this reproduction is dependent upon the quality of the copy submitted.

In the unlikely event that the author did not send a complete manuscript and there are missing pages, these will be noted. Also, if material had to be removed, a note will indicate the deletion.

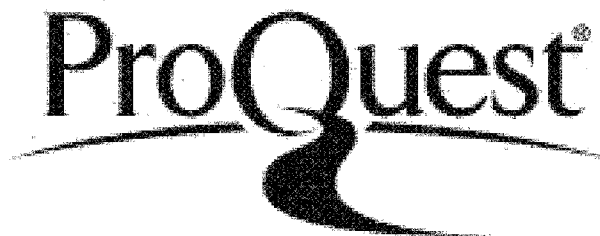


UMI 3533976

Published by ProQuest LLC 2012. Copyright in the Dissertation held by the Author.

Microform Edition © ProQuest LLC.

All rights reserved. This work is protected against unauthorized copying under Title 17, United States Code.



ProQuest LLC
789 East Eisenhower Parkway
P.O. Box 1346
Ann Arbor, MI 48106-1346

Copyright by

Linhui Zhang

2012

ii

APPROVAL PAGE

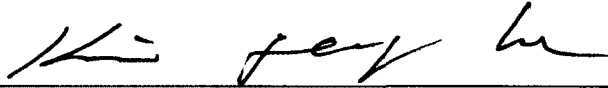
Doctor of Philosophy Dissertation

Dynamic Finite Element Modeling and Analysis of Blast-resistant Sandwich Structures

Presented by

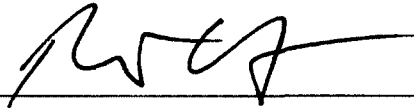
Linhui Zhang, B.E., M.S.

Major Advisor



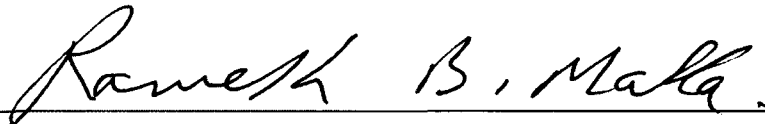
Jeong-Ho Kim

Associate Advisor



Rainer Hebert

Associate Advisor



Ramesh B. Malla

University of Connecticut

2012

Acknowledgements

I would like to state my sincere and utmost gratitude to my advisor, Dr. Jeong-Ho Kim for his constant support and encouragement. I came to United States with a bachelor degree and little research experience. Lots of improvements have occurred both in my research and life under his guidance. I could not have imagined having a better advisor and mentor, and with his insightful guidance and the knowledge he bestowed me, I am able to achieve my PhD. I wish him the best of luck in his life and professional endeavors.

I would like to thank my associate advisor Dr. Ramesh B. Malla for all his great suggestions on my PhD study and arranging the qualifying exam for me. Many thanks must go to my associate advisor Dr. Rainer Hebert for all his support on my research project.

I am very thankful for the financial support from Department of Homeland Security through the project “Advanced Composite Materials for Blast and Fire Resistance”. I also want to credit the support from the Center for Resilient Transportation Infrastructure at University of Connecticut directed by Prof. Michael Accorsi. The Department of the Civil and Environmental Engineering, University of Connecticut, including all the faculty members, staffs and students deserve a credit for their effort in providing a great ambience for good study and research.

Last, but not least, I want to express my gratitude to my parents. Their self-less love and tremendous support are the momentum for me to achieve my dream.

Table of Contents

1. Introduction	1
1.1 Effects of explosions on structures and human	1
1.2 Blast waves	4
1.3 Fluid-structure interaction	6
1.4 Blast mitigation strategies	9
1.5 Experimental methods	10
1.6 Research objectives	11
1.7 Organization of the dissertation	13
2. Dynamic Finite Element Analysis of Sandwich Plates with Various Corrugated Core Arrangements	15
2.1 Introduction	15
2.2 Corrugated sandwich plates with various core arrangements	17
2.3 Quasi-static analysis of corrugated sandwich plates	19
2.3.1 Quasi-static testing of corrugated sandwich plates	19
2.3.2 Quasi-static finite element modeling of corrugated sandwich plates	20
2.3.3 Results and discussion	22
2.3.3.1 Compression load-deflection curve	22
2.3.3.2 Energy quantities	27
2.3.3.3 Comparison and discussion	29
2.4 Shock tube testing of corrugated sandwich plates	30
2.5 Finite element modeling of corrugated sandwich plates subjected to shock tube loading	35

2.5.1	Finite element modeling	35
2.5.2	Rate-dependent material property obtained by SHPB testing and its implementation into ABAQUS	37
2.5.3	Loading approximation	39
2.6	Results and discussion of corrugated sandwich plates subjected to shock tube loading	40
2.6.1	Deformed shapes and mid-span deflection histories	40
2.6.2	Velocity histories at the center of front and back faces	51
2.6.3	Energy plots	54
2.6.4	Von Mises stress histories at critical locations	57
2.6.5	Contact reaction force between support and corrugated sandwich plate ..	59
2.7	Concluding remarks	62
3	A Parametric Study on Blast-resistant Corrugated and Trapezoid Sandwich Structures	64
3.1	Introduction	64
3.2	Unit-cell corrugated and trapezoid sandwich structures with various cores	66
3.2.1	Unit-cell corrugated sandwich structures	66
3.2.2	Unit-cell trapezoid sandwich structures	68
3.2.3	Material properties	70
3.3	Dynamic responses of unit-cell corrugated and trapezoid sandwich structures with various core arrangements under idealized blast loading	72
3.3.1	Idealized blast loading	72
3.3.2	Finite element modeling	73

3.3.3	Maximum core compression under different initial velocities	74
3.3.3.1	Unit-cell corrugated sandwich structures	74
3.3.3.2	Unit-cell trapezoid sandwich structures	78
3.3.3.3	Comparison on the maximum core compressions of unit-cell corrugated and trapezoid sandwich structures	82
3.3.4	Maximum compressive reaction force at the back face under different initial velocities	82
3.3.5	Energy plots	85
3.3.6	Strain rate dependence	89
3.4	Effects of geometric imperfections	91
3.4.1	Geometric imperfection shapes obtained from buckling analysis	92
3.4.1.1	Geometric imperfection shapes for unit-cell corrugated sandwich structure with BBBB core arrangement	92
3.4.1.2	Geometric imperfection shapes for unit-cell trapezoid sandwich structure with BBBB core arrangement	93
3.4.2	Comparison on the geometric imperfection sensitivity of corrugated and trapezoid sandwich structures	94
3.4.3	Effects of geometric imperfections on the dynamic response of unit-cell sandwich structures with trapezoid BBBB core arrangement	97
3.5	Concluding remarks	100
4	Finite Element Procedure on the Dynamic Response of Rate-dependent Functionally Graded Steel Plates Subjected to Dynamic Air Pressure Loads ..	102
4.1	Introduction	102

4.2 Strain-rate dependent models for FGM and numerical implementations	105
4.2.1 Strain-rate dependent material model	105
4.2.2 Split-Hopkinson pressure bar tests	107
4.2.3 Hypothetic functionally graded plate	108
4.2.4 Rate-dependent FGM model	110
4.2.5 VUMAT implementation of rate-dependent FGM model	114
4.3 Shock tube testing on dynamic responses of a monolithic plate	116
4.4 Dynamic finite element modeling	119
4.5 Finite element results and discussion	121
4.5.1 Dynamic response of steel 1018	121
4.5.2 Dynamic response of functionally graded plate	124
4.6 Concluding remarks	128
5 Conclusions and Future Work	130
Appendix – Functionally Graded Material Composed of Two Ductile Constituent Materials with Power-law Strain Hardening Model	131
References	137

List of Figures

1.1	The World Trade Center burning in the September 11 attack in 2001 [1]	2
1.2	The Alfred P. Murrah Federal Building in Oklahoma City after the terrorist attack of April 19, 1995 [2]	2
1.3	USS Cole after bombing attack [5]	3
1.4	The free-field overpressure-time history at a fixed location close to explosive center [10].....	4
1.5	Taylor’s plot for assessing fluid-structure interaction [22, 23]	8
1.6	The shock tube facility in University of Rhode Island [47]	11
1.7	Unit-cell models of the (a) corrugated and (b) trapezoid structures	13
2.1	Corrugated sandwich plate sample	18
2.2	Die for the manufacture of corrugated layers	19
2.3	Quasi-static testing on corrugated sandwich structures	20
2.4	Finite element model of 1/4 corrugated sandwich plate	21
2.5	Constitutive curves for substrate and core materials	22
2.6	Compression load-deflection curve of AAAA core arrangement	23
2.7	Compression load-deflection curve of BBBB core arrangement	24
2.8	Compression load-deflection curve of CCCC core arrangement.....	24
2.9	Compression load-deflection curve of AABC core arrangement	25
2.10	Compression load-deflection curve of AACC core arrangement	26
2.11	Compression load-deflection curve of ABBC core arrangement	26
2.12	Compression load-deflection curve of ABCC core arrangement	27

2.13	Energy plots for (a) AAAA (b) BBBB (c) CCCC (d) AABC (e) AACC (f) ABBC and (g) ABCC core arrangements	29
2.14	The shock tube facility to generate controlled blast loading [47]	31
2.15	(a) Fixture of the corrugated sandwich plate during shock tube testing (b) a schematic plot of shock tube testing	31
2.16	The muzzle setup [53]	32
2.17	Typical measured shock tube pressure profile [53]	33
2.18	Reflected pressure profile measured by the sensor during shock tube testing for (a) AAAA, BBBB and CCCC (b) AABC, AACC, ABBC and ABCC core arrangements	34
2.19	Placement of camera system w.r.t the shock tube and specimen [53]	35
2.20	Finite element modeling of the corrugated sandwich plates	36
2.21	Stress-strain curves of steel 1018 at different strain rates	38
2.22	Stress-strain curves of steel 1008 at different strain rates	38
2.23	Spatial distribution of the shock tube loading	39
2.24	(a) Deformed shapes for AAAA core arrangement at critical times (b) Mid-span deflection histories of front and back face for AAAA core arrangement	41
2.25	(a) Deformed shapes for BBBB core arrangement at critical times (b) Mid-span deflection histories of front and back face for BBBB core arrangement	43
2.26	(a) Deformed shapes for CCCC core arrangement at critical times (b) Mid-span deflection histories of front and back face for CCCC core arrangement	44
2.27	(a) Deformed shapes for AABC core arrangement at critical times (b) Mid-span deflection histories of front and back face for AABC core arrangement	45

2.28 (a) Deformed shapes for AACC core arrangement at critical times (b) Mid-span deflection histories of front and back face for AACC core arrangement	47
2.29 (a) Deformed shapes for ABBC core arrangement at critical times (b) Mid-span deflection histories of front and back face for ABBC core arrangement	48
2.30 (a) Deformed shapes for ABCC core arrangement at critical times (b) Mid-span deflection histories of front and back face for ABCC core arrangement	49
2.31 Velocity histories for (a) AAAA (b) BBBB (c) CCCC (d) AABC (e) AACC (f) ABBC and (g) ABCC core arrangements	52
2.32 Plastic energy absorbtion by substrates and core for (a) AAAA (b) BBBB (c) CCCC (d) AABC (e)AACC (f) ABBC and (g) ABCC core arrangements	55
2.33 Von Mises stress histories at the center of front and back face for (a) AAAA (b) BBBB (c) CCCC (d) AABC (e) AACC (f) ABBC and (g) ABCC core arrangements	59
2.34 Contact reaction force between the specimen and support for (a) AAAA (b) BBBB (c) CCCC (d) AABC (e) AACC (f) ABBC and (g) ABCC core arrangements	60
3.1 Unit-cell corrugated sandwich structures with (a) BBBB (b) AACC (c) ABBC and (d) Gradually graded core arrangements	68
3.2 Unit-cell trapezoid sandwich structures with (a) BBBB (b) AACC (c) ABBC and (d) Gradually graded core arrangements	70
3.3 Stress-strain curves of steel 1018 at different strain rates	71
3.4 Stress-strain curves of steel 1008 at different strain rates	71
3.5 Maximum core compression of corrugated BBBB arrangement under initial velocity: (a) 10m/s (b) 20m/s (c) 30m/s (d) 40m/s and (e) 50m/s	75

3.6	Maximum core compression of corrugated AACC arrangement under initial velocity: (a) 10m/s (b) 20m/s (c) 30m/s (d) 40m/s and (e) 50m/s	76
3.7	Maximum core compression of corrugated ABBC arrangement under initial velocity: (a) 10m/s (b) 20m/s (c) 30m/s (d) 40m/s and (e) 50m/s	76
3.8	Maximum core compression of corrugated gradually graded core arrangement under initial velocity: (a) 10m/s (b) 20m/s (c) 30m/s (d) 40m/s and (e) 50m/s	77
3.9	Maximum core compressions for unit-cell corrugated sandwich structures with various cores subjected to different initial velocities	78
3.10	Maximum core compression of trapezoid BBBB arrangement under initial velocity: (a) 10m/s (b) 30m/s (c) 50m/s (d) 70m/s and (e) 90m/s	79
3.11	Maximum core compression of trapezoid AACC arrangement under initial velocity: (a) 10m/s (b) 30m/s (c) 50m/s (d) 70m/s and (e) 90m/s	79
3.12	Maximum core compression of trapezoid ABBC arrangement under initial velocity: (a) 10m/s (b) 30m/s (c) 50m/s (d) 70m/s and (e) 90m/s	80
3.13	Maximum core compression of trapezoid gradually graded core arrangement under initial velocity: (a) 10m/s (b) 30m/s (c) 50m/s (d) 70m/s and (e) 90m/s	81
3.14	Maximum core compressions for unit-cell trapezoid sandwich structures with various cores subjected to different initial velocities	81
3.15	Maximum reaction force at the back face of unit-cell corrugated sandwich structures with various cores subjected to different initial velocities	83
3.16	Maximum reaction force at the back face of unit-cell trapezoid sandwich structures with various cores subjected to different initial velocities	85

3.17 Plastic energy histories for unit-cell corrugated sandwich structures with various cores under initial velocity: (a) 10m/s (b) 20m/s (c) 30m/s and (d) 40m/s	86
3.18 Plastic energy histories for unit-cell trapezoid sandwich structures with various cores under initial velocity: (a) 10m/s (b) 30m/s (c) 50m/s and (d) 70m/s	88
3.19 Plastic energy w.r.t compressive strain for unit-cell corrugated BBBB sandwich structures under average compressive strain rate: (a) 264.62/s (b) 419.62/s (c) 864.23/s and (e) 1116.49/s	90
3.20 Plastic energy w.r.t compressive strain for unit-cell trapezoid BBBB sandwich structures under average compressive strain rate: (a) 444.95/s (b) 863.44/s (c) 1114.89/s and (d) 1824.16/s	91
3.21 Imperfection shapes for unit-cell corrugated sandwich structure with BBBB core arrangement obtained from buckling analysis: (a) Mode I (b) Mode II and (c) Mode III	93
3.22 Imperfection shapes for unit-cell trapezoid sandwich structure with BBBB core arrangement obtained from buckling analysis: (a) Mode I (b) Mode II and (c) Mode III	93
3.23 Imperfection shapes for unit-cell corrugated sandwich structure with BBBB core arrangement introduced to dynamic analysis: (a) Mode I (b) Mode II and (c) Mode III	94
3.24 Imperfection shapes for unit-cell trapezoid sandwich structure with BBBB core arrangement introduced to dynamic analysis: (a) Mode I (b) Mode II and (c) Mode III	95

3.25	Maximum core compressions for unit-cell corrugated sandwich structure with BBBB core arrangement with and without geometric imperfection subjected to different initial velocities	96
3.26	Maximum core compressions for unit-cell trapezoid sandwich structure with BBBB core arrangement with and without geometric imperfection subjected to different initial velocities	97
3.27	Maximum core compressions for trapezoid BBBB core arrangement with Mode I imperfections subjected to different initial velocities	98
3.28	Maximum core compressions for trapezoid BBBB core arrangement with Mode II imperfections subjected to different initial velocities	99
3.29	Maximum core compressions for trapezoid BBBB core arrangement with Mode III imperfections subjected to different initial velocities	100
4.1	Comparison on strain-rate dependent models	106
4.2	Stress-strain curves of steel 1018 at different strain rates	108
4.3	Stress-strain curves of steel A36 at different strain rates [80]	109
4.4	A schematic plot of linearly graded FG steel plate	109
4.5	Concept of modified rule of mixture at a fixed strain rate	111
4.6	Flow chart of VUMAT implementation in ABAQUS	116
4.7	(a) Dynamic air pressure load generated by the shock tube; (b) shock tube testing setup	118
4.8	Deformation history of Steel 1018 plate during shock tube testing	118
4.9	3D Finite element mesh for both monolithic and FGM plates (No. of Elements: 24576; No. of Nodes: 29961)	119

4.10	Spatial distribution of the dynamic air pressure loading	120
4.11	Comparison of displacement histories of the center point in Steel 1018 plate	122
4.12	Energy histories of a monolithic plate (steel 1018) subjected to dynamic air pressure load	124
4.13	Displacement histories for the center point of four material configurations. All are the FEM results	125
4.14	Von Mises stress contours at the time of maximum deformation: (a) Steel 1018 plate at 1.54ms; (b) Steel A36 plate at 1.66ms; (c) FG plate at 1.60ms; (d) Plate with effective material at 1.60ms	126
4.15	Time histories of von Mises stresses at the center of (a) front face and (b) back face	127
4.16	Energy histories of plates with four material models: (a) External work (b) Internal energy (c) Kinetic energy (d) Plastic dissipation	128
A.1	Concept of modified rule of mixture	132

List of Tables

2.1 Load to start crushing and relative density for all the core arrangements	30
2.2 Maximum back face deflection of corrugated sandwich plates	51
2.3 Maximum back face velocity of corrugated sandwich plates	54
2.4 Plastic energy absorption distribution after the corrugated plates reach a stable status	57
2.5 Impulse transmitted from sandwich plate to one support till 4ms	61
3.1 Layer thickness for unit-cell corrugated sandwich structures	67
3.2 Layer thickness for unit-cell trapezoid sandwich structures	69
4.1 Material parameters for constituent materials	112
A.1 Material parameters for constituent materials	133

Chapter 1 - Introduction

This dissertation is concerned with blast mitigation strategies by utilizing sandwich structures and functionally graded (FG) materials. This chapter describes the fundamentals of the blast effects and mechanism, summarizes the blast mitigation strategies, proposes the research methods and objectives, and outlines the scientific contributions of this work.

1.1 Effects of explosions on structures and human

The significant increase of blasts and explosions on the buildings, public transportation systems, and military infrastructures are gaining more and more attentions. Recent terrorist attacks on the public buildings and transportation systems have caused severe structure damages and lots of death. The most famous examples include the September 11 event on the Twin Towers of World Trade Center (Figure 1.1), the truck bomb in front of the Alfred P. Murrah Federal Building (Figure 1.2) in Oklahoma City, the explosions of bombs on four commuter trains in Madrid, Spain, on March 11, 2004[3] and the series of small bomb attacks in London in the month of July, 2005 [4]. Thousands of lives were lost during these tragedies. Besides, the military devices are also the main targets to the explosions. The examples include the USS Cole bombing (Figure 1.3) on October 12, 2000 and the improved explosion devices (IEDs) in Iraq and Afghanistan.



Figure 1.1 The World Trade Center burning in the September 11 attack in 2001 [1]

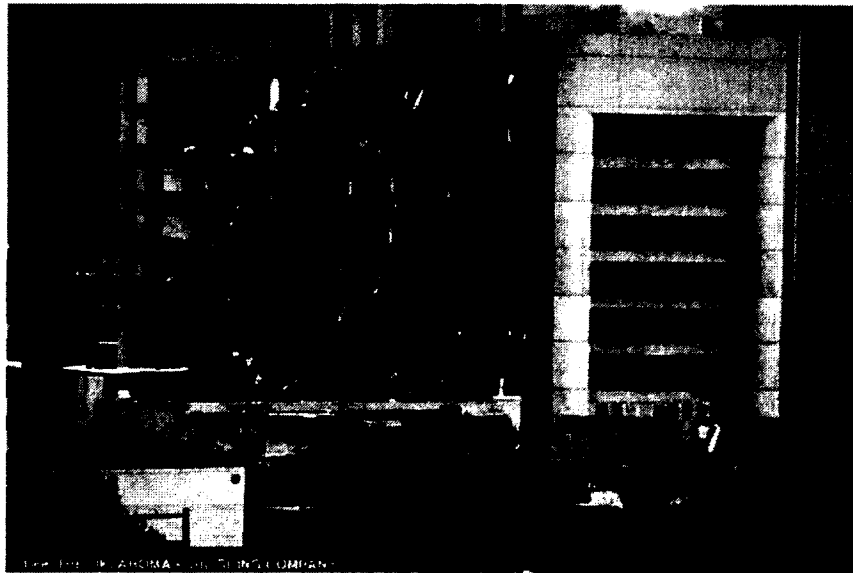


Figure 1.2 The Alfred P. Murrah Federal Building in Oklahoma City after the terrorist attack of April 19, 1995 [2]



Figure 1.3 USS Cole after bombing attack [5]

In order to protect these infrastructures, military devices and human beings, the phenomena of the blast and explosion should be understood well. The explosion is the release of large amounts of chemical, mechanical and nuclear energy in a very short time in the time duration on the order of 10^{-6} to 10^{-3} seconds [6]. The energy is released mainly in the form of blast wave, heat, light and sound. The blast wave consist highly compressed air traveling radially outward from the source at very high velocities, when it reaches the building and other infrastructures, the loading on the structure is usually considered as a blast pressure loading which has a huge value up to 100MPa [7] or even higher in nuclear explosions. The blast wave contains up to 95% of the total energy in the conventional high-energy explosions [8], while the rest of the energy is dissipated in the form of thermal radiation, light generation and sound. The effects of the blast waves are the main interest in this work. In the following section, the blast wave generated during blast and explosions is discussed in details.

1.2 Blast waves

As the other waves, the blast wave carries energy and travels through a medium, for example air and water. Blast waves are characterized by an abrupt, nearly discontinuous change in the characteristics of the medium [9]. Across the shock, there is always rapid increase in pressure. If a sensor is placed at a fixed location close to an explosion, the typical free-field overpressure profile is shown in Figure 1.4. The overpressure refers to the difference between the static pressure and the ambient atmospheric pressure here. The free-field overpressure profile has the positive phase with peak overpressure value P_s and time duration t_o , and the negative phase with peak overpressure value P_s^- and time duration t_o^- [10].

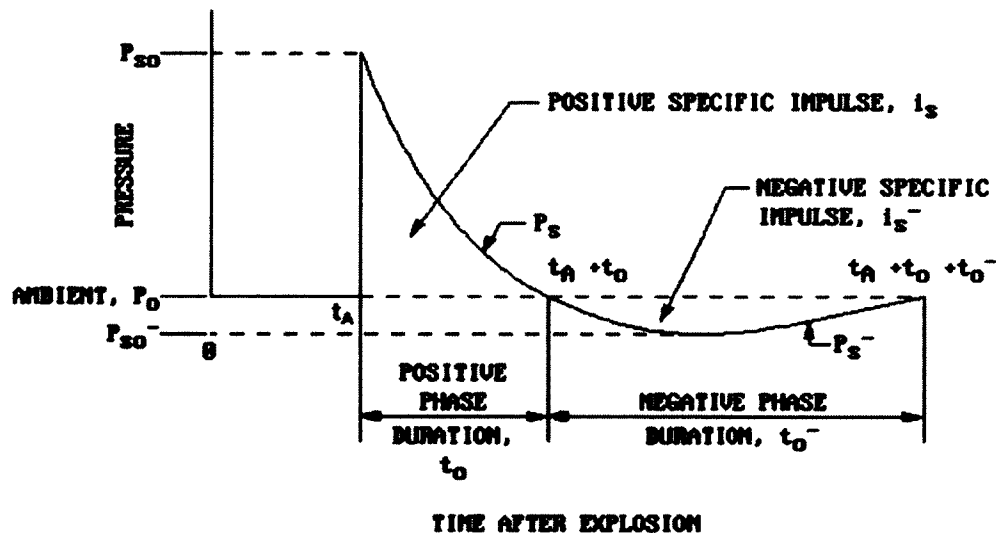


Figure 1.4 The free-field overpressure-time history at a fixed location close to explosive center [10]

The most important parameter describing the blast wave is the peak overpressure value P_s . It is related to the energy released during the explosions. The scaling laws for explosions were first derived by Taylor [11, 12].

$$L = C_1(\gamma) \left(\frac{E_0 t^2}{\rho_0} \right)^{\frac{1}{5}} \quad (1.1)$$

$$P_s = C_2(\gamma) \frac{E_0}{L^3} \quad (1.2)$$

where E_0 is the energy released during explosions, L is the distance between the explosive center and the blast wave front, ρ_0 is the ambient atmospheric density, γ is the ratio of the specific heats of air, and C_1 , C_2 are constants depending on the medium properties. Neumann obtained the similar solutions as these results of Taylor [13]. Since then, a number of exact solutions for strong explosions were developed [14, 15 and 16].

Brode [17, 18] proposed a formula giving the peak overpressure P_s in terms of the scaled distance $z = r/W^{\frac{1}{3}}$ where r is the distance from the explosion center to the point of interest and W is the TNT equivalent of the explosive material:

$$P_s = \begin{cases} \frac{6.7}{z^3} + 1, & P_s > 10 \text{ atm} \\ \frac{0.975}{z} + \frac{1.455}{z^2} + \frac{5.85}{z^3} - 0.019, & 0.1 \text{ atm} \leq P_s \leq 10 \text{ atm} \end{cases} \quad (1.3)$$

The common explosive materials can be measured with equivalent amount of TNT.

Besides the commonly used relations between the peak overpressure w.r.t released energy, between the peak overpressure w.r.t the scaled distance, the overpressure

profile w.r.t time is also important. There are a number of models [19, 20] to approximate the pressure profile shown in Figure 1.4. A commonly used mode is the exponential model which can be written as:

$$P(t) = P_s e^{-\frac{t}{t_o}} \quad (1.4)$$

Where P_s refers to the peak overpressure value and t_o is the decay time which is chosen by maintaining the same peak overpressure and same impulse of the positive phase.

$$I = \int_0^{t_o} P(t) dt \quad (1.5)$$

There are also many more complicated models to provide better match with the experimental or real pressure profile. If the time duration of blast pressure pulse is short compared to the response time of the plate, the pressure pulse can be replaced by the impulse [21].

1.3 Fluid-structure interaction

The fluid-structure interaction benefits the structure to withstand blast loading, since it can reduce the impulse transmitted to the structure. Here, we assume a pressure pulse with the free-field momentum I_o . If the blast wave travels to a rigid wall, the momentum transmitted to the rigid wall is around $2I_o$. But the movement of the structure can relieve the pressure acting on it, and then reduce the impulse transmitted to the structure, as a result to mitigate the effects of blast on structures.

Taylor used the solution for a one-dimensional wave pulse impinging on a solid to find the momentum transmitted to the plate by blast pulse [22]. The back face of the plate is not restrained. A pressure pulse with profile as $p = P_s e^{-t/t_0}$ is considered. Then the corresponding free-field momentum per unit area is $I_0 = \int_0^{\infty} p dt = P_s t_0$. Due to the deformation of the plate, when the pressure pulse reaches the plate, part of it gets reflected. In Taylor's theory, the momentum transmitted to the plate per unit area can be obtained by:

$$\frac{I}{I_0} = 2q^{\frac{q}{1-q}} \quad (1.6)$$

where $q = t_0/t_*$. The time scale t_* in this relation characterizing the fluid-plate interaction is defined as,

$$t_* = \frac{\rho h}{\rho_f c_f} \quad (1.7)$$

Where, ρ is the material density for the plate, h is the plate thickness, ρ_f is the density of the fluid and c_f is the speed of sound in the fluid. The momentum ratio (I/I_0) between the imparted impulse and the initial impulse as a function of time scale ratio t_0/t_* is plotted in Figure 1.5.

Generally, Taylor's theory predicts that under the same pressure pulse, lighter structure acquires less transmitted impulse than the heavier structure. Here, we also want to compare the fluid-structure interaction effects in air and water by assuming

the same plate located in both air and water and subjected to the same blast pressure pulse. Since the density for water is much larger than that of air (almost thousand times larger), the time scale ratio q is much larger in the water than in the air. As a result, the transmitted impulse is much smaller in water. The fluid-structure interaction effect is more obvious in water blast than that in air blast. But the limitation of Taylor's model is that it neglects the nonlinear fluid compressibility.

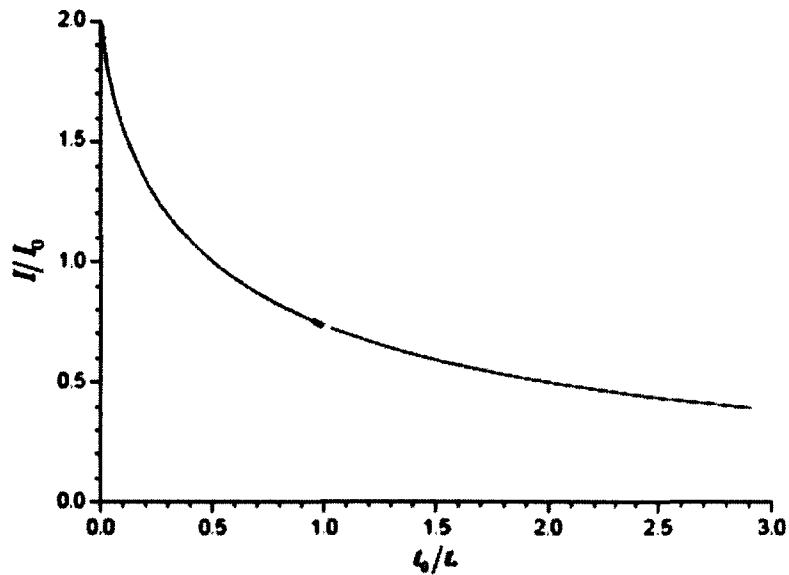


Figure 1.5 Taylor's plot for assessing fluid-structure interaction [22, 23]

Kambouchev *et al* investigated the nonlinear compressibility effects in fluid-structure interaction and their applications on the air-blast loading of structures [24]. They found that the effect of nonlinear compressibility can further enhance the mitigation of transmitted impulse provided by fluid-structure interaction effects in the linear range, especially for the high-density blast waves. It shows that the fluid-structure interaction doesn't only benefit the water blast, but also benefit the structures under high-intensity air blast waves.

1.4 Blast mitigation strategies

Blast mitigation methods are gaining more and more interest in both industry and research field. In addition to operational strategies, such as keeping sufficient distance between targets and public area, there are also many technical recommendations on the structure optimization and blast-resistant materials. The main technical suggestions are the continuity of structures, reserve strength in excess of live loads, redundancy in load bearing paths and increased energy absorption [25, 26]. These concepts can be realized by the metal-foams [27], sandwich structures [28] and polymers [29].

This work focuses on utilizing sandwich structures to mitigate the blast effects on the structures. Lots of publications focus on the advanced blast-resistant behavior of sandwich structures with different cores, such as trapezoid, honeycomb, tetrahedral, pyramidal and so on [23, 30-34]. Xue and Hutchinson first compared the dynamic responses of sandwich plates and monolithic plates with the same material and total mass [33]. In their original work, the fluid-structure interaction is neglected. Later, Xue and Hutchinson optimized the sandwich structures based on the Taylor's fluid-structure interaction theory with given face-sheet/core assembly with specific mass per unit area and subject to a prescribed momentum impulse per area [23]. In Xue and Hutchinson's work, they considered two phases: the fluid-structure interaction phase which has very short time duration and the structure response phase. Fleck and Deshpande brought up a three-phase analytical model for sandwich beams: 1) the fluid structure interaction phase: the impulse transmitted to the beam is calculated; 2) the core compression phase: the total momentum is conserved and the energy is

reduced due to the core compression in the sandwich beam; and 3) beam bending and longitudinal stretching phase: after the densification of the core, the sandwich beams performs similar as the monolithic beams [34]. However, the experiments from previous work show that the separation of these phases cannot be assumed for all the cases and coupling between II and III phases can exist [35, 36].

The objective of sandwich beam or plate is to minimize the back face deflection, minimize the core compression, increase the energy absorption and reduce the support reactions [37]. The works of Tilbrook *et al* [37] and Liang *et al* [38] found that the soft core with a low transverse strength reduces the transmitted impulse during the fluid-structure interaction stage for water blast and increases the coupling between core compression phase and beam bending phase. But the soft core can get fully crushed and give a very high support reaction.

1.5 Experimental methods

There are mainly three experimental methods to investigate the dynamic response of the structures subjected to blasts.

- 1) The use of projectiles to simulate the blast loading. The high-intensity pressure pulse is generated by different kinds of projectiles [39, 40]. This type of approximation of blasts basically doesn't consider the fluid-structure interaction.
- 2) Field blast testing. There have been lots of papers published on the field blast testing on structure, especially lots on the ultra-high performance fibred concrete [41-43]. But the limitation of the real blast testing is the cost, danger and reproducibility.

3) Shock tube testing. In this work, the shock tube testing is used as the experimental tool to investigate the blast-resistant behavior of the sandwich plates and carried out at the University of Rhode Island (Prof. Arun Shukla), shown in Figure 1.6. The shock tube is divided into a high-pressure driver section and a low-pressure driven section, which are separated by a destructible diaphragm [44-46]. The pressure difference between these two sections becomes higher when pressurizing the high-pressure driver section. When the pressure difference reaches a critical value, the diaphragm ruptures and the resulting rapid release of gas forms a one-dimensional shock wave front. When the shock wave reaches the specimen, the dynamic air pressure load is applied to the specimen. This is a method that is easy to control and takes the fluid-structure interaction into consideration.



Figure 1.6 The shock tube facility in University of Rhode Island [47]

1.6 Research objectives

It has been proven that the sandwich structures outperform the monolithic structures with the same mass when subjected to blast or impact loadings. There are relatively fewer researches done on the sandwich structures with graded cores. An experimental investigation on sandwich beams with a piece-wise functionally graded core was performed by Avila [48]. The work of Apetre *et al.* on the impact damage of sandwich structures with a graded core has shown that a reasonable core design can

effectively reduce the shear forces and strains within the structures [49]. Shukla *et al.* performed shock tube experiment to study the dynamic response of sandwich panels with E-Glass Vinyl Ester (EVE) composite face sheets and stepwise graded foam cores [44, 50-51]. The shock tube testing results indicated that monotonically increasing the wave impedance of the foam core from the front (facing shock tube loading) to the back and reducing the wave impedance mismatch between successive foam layers can greatly enhance the overall blast resistance of sandwich composites.

In the first part of this work, we focus on investigating the effect of various homogeneous and graded core arrangements on the blast-resistant behavior of the corrugated sandwich plates subjected to shock tube loading. The corrugated sandwich made of steel has two substrates on front and back and four corrugated layers in the core. The thicknesses of these corrugated layers are different, which leads to different core arrangements by following different orders of these corrugated layers. The shock tube testing was conducted on the corrugated sandwich plates with various core arrangements. And the finite element method is also utilized to simulate the dynamic response of corrugated sandwich structures subjected to shock tube loading with fluid-structure interaction approximation.

Following that, a parametric study on the one-dimensional crushing of unit-cell corrugated and trapezoid sandwich structures with give mass and different graded core arrangements under idealized blast loading is also carried out. The unit cells of corrugated and trapezoid sandwich structures with a graded core arrangement are shown in Figure 1.7. The main objective of this parametric study is to find out the effect of the graded core arrangement, the comparison between the impact tolerances,

and the comparison between initial geometric imperfection sensitivity of corrugated and trapezoid sandwich structures.

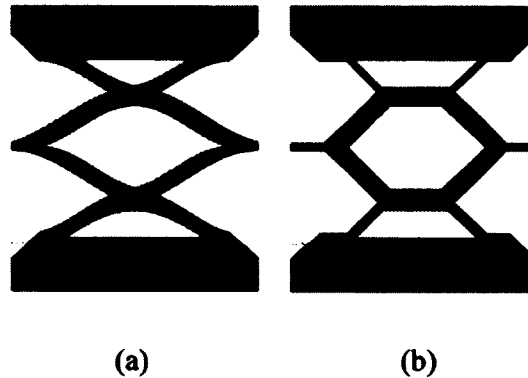


Figure 1.7 Unit-cells of the (a) Corrugated and (b) Trapezoid sandwich structures

Based on the first two parts of research, we found the utilization of graded cores benefits the blast-resistant performance of the sandwich structures. We want to extend the stepwise graded core to the core made with functionally graded material. In the last part of this research, a modified rule of mixture and linear strain-rate dependence are used to derive the rate-dependent elastic-plastic constitutive relations for a functionally graded material (FGM) based on the constitutive relations for its constituent materials. The derived constitutive relations for FGM are implemented in ABAQUS/Explicit through a VUMAT subroutine. The developed FGM model and its implementation in finite element procedure promote the simulations on the dynamic or impact responses of structures made of FGM.

1.7 Organization of the dissertation

The dissertation is organized as follows: Chapter 1 introduces the background of the research, the effects of blast on structures, the mechanism of the blast wave and fluid-structure interaction, the research methods and the objectives of this work. Chapter 2

mainly talks about the dynamic responses of sandwich plates with different corrugated core arrangements subjected to shock tube loading and the quasi-static responses are also investigated. The quasi-static testing and shock tube testing are used as the experimental tools and the finite element simulation is utilized as the simulation tool in Chapter 2. Chapter 3 carries out a parametric study on the one-dimensional crushing behavior of unit-cell corrugated and trapezoid sandwich structures with a given mass and different core arrangements. And the geometric imperfection analysis is also carried out. Due to the advantages of utilizing graded cores, a rate-dependent FGM model and its implementation into finite element procedure through a VUMAT subroutine are developed in Chapter 4 to investigate the dynamic response of rate-dependent functionally graded steel plates subjected to dynamic loads. Chapter 5 concludes the work.

Chapter 2 - Dynamic Finite Element Analysis of Sandwich Plates with Various Corrugated Core Arrangements

2.1 Introduction

The blasts and explosions can lead to extreme damage to the structures and human beings. The most famous examples include the September 11 attacks, the bombing in Federal building of Oklahoma City, and a lot others. The blast wave, heat and fire generated during the blasts and explosions are the main causes of damage and the blast wave is the main concern in this work. To mitigate the damage caused by blast and explosions, the main technology recommendations are the continuity of structures, reserve strength in excess of live loads, redundancy in load bearing paths and increased energy absorption [25, 26]. These concepts can be realized by the metal-foams [27], sandwich structures [28] and polymers [29].

This work focuses on utilizing sandwich structures to mitigate the blast effects. Many works have been published on the advanced blast-resistant behavior of sandwich structures with different cores, such as the trapezoid, corrugated, honeycomb, tetrahedral, trusses and pyramidal cores [23, 30-34]. Xue and Hutchinson showed that the sandwich plates outperform the corresponding monolithic plates with the same material and total mass subjected to blast loading [33]. In that work, the fluid-structure interaction is neglected. Later, Xue and Hutchinson optimized the sandwich structures based on the Taylor's theory with given face-sheet/core assembly with specific mass per unit area and subject to a prescribed momentum impulse per area [23]. Fleck and Deshpande brought up a three-phase analytical model for sandwich

beams which is adopted in lots of publications: 1) the fluid structure interaction phase; 2) core compression phase and 3) beam bending and longitudinal stretching phase [34]. The experiments from previous work show that the separation of these phases cannot be assumed for all the cases and II and III phases can be coupled [35, 36].

The objective of sandwich plate design and optimization is to minimize the back face deflection, minimize the core compression, increase the energy absorption and reduce the support reactions [37]. The works of Tilbrook *et al.* [37] and Liang *et al.* [38] found that the soft core with a low transverse strength reduces the transmitted impulse during the fluid-structure interaction stage for water blast and increases the coupling between core compression phase and beam bending phase. But the soft core can get fully crushed and give a very high support reaction.

There are relatively fewer researches done on the blast-resistant structures with graded foam or foam-like and polymer cores. An experimental investigation on sandwich beams with a piece-wise functionally graded (density) core was performed by Avila [48]. The work of Apetre *et al.* on the impact damage of sandwich structures with a graded core has shown that a reasonable core design can effectively reduce the shear forces and strains within the structures [49]. Shukla *et al.* performed shock tube experiment to study the dynamic response of sandwich panels with E-Glass Vinyl Ester (EVE) composite face sheets and stepwise graded foam cores [44, 50-51]. The shock tube testing results indicated that monotonically increasing the wave impedance of the foam core from the front (facing shock tube loading) to the back and reducing the wave impedance mismatch between successive foam layers can greatly enhance the overall blast resistance of sandwich composites.

But little work has been done on the blast responses of corrugated sandwich plates, and such plates with graded cores. In this work, the dynamic responses of corrugated sandwich plates with various homogeneous and graded core arrangements under blast loading are investigated by shock tube testing and finite element simulation. Besides, the quasi-static behavior of the corrugated structures is also investigated.

This chapter is organized as follows: Section 2.2 describes the corrugated sandwich plate samples with various core arrangements. Section 2.3 talks about the quasi-static experiment and finite element simulation of the corrugated sandwich plates. Section 2.4 presents the shock tube testing on the corrugated sandwich plates and Section 2.5 describes the finite element modeling to investigate the dynamic response of the corrugated layers subjected to shock tube loading. Section 2.6 discusses the finite element simulation and shock tube testing results. Section 2.7 concludes this chapter.

2.2 Corrugated sandwich plates with various core arrangements

The corrugated sandwich plate in this work is designed to be attached to the main structure components in order to mitigate the damage lead by the blast pressure. The corrugated sandwich plate is composed of two substrates, which are also called front (facing the loading) substrate, back substrate, and four corrugated layers, shown in Figure 2.1. The substrates have the same dimensions, 2in in width, 8in in length and 3mm in thickness.



Figure 2.1 Corrugated sandwich plate sample

The corrugated layers are curved by a circular die, shown in Figure 2.2, but after the die is removed, the shape of the corrugated layers is approximately a half-sine curve rather than a circular curve. The height of each corrugated layer is around 6mm. The thicknesses for the four corrugated layers are not uniform and three different thicknesses are considered here. In the following sections, A refers to 0.03in, B refers to 0.02in and C refers to 0.01in. By following different orders of the four corrugated layers, seven arrangements of the corrugated sandwich plates are taken into consideration in this chapter. Nominating the layers from the back face to front face (facing the loading), the seven arrangements can be written as AAAA, BBBB, CCCC, AABC, AACC, ABBC and ABCC. Note that the corrugated layer closer to the back face should be thicker (check paper [50] for more information).

The substrates are made of steel 1018 as received, while the corrugated layers are made of steel 1008 after heating to 900C and furnace cooling. The material properties and its implementation into finite element simulation will be discussed in details in section 2.3.2 and section 2.5.2. The substrates and the corrugated layers are welded together through both ends of the surfaces in contact.



Figure 2.2 Die for the manufacture of corrugated layers

2.3 Quasi-static analysis of corrugated sandwich plates

In the first stage, the quasi-static behavior of the corrugated sandwich plates was investigated.

2.3.1 Quasi-static testing of corrugated sandwich plates

The quasi-static testing on the corrugated sandwich structures was performed by Prof. Hebert's group at University of Connecticut. The corrugated sandwich plate specimen was placed on two rigid supports with a span of 6in and symmetric with respect to the axis of punch, shown in Figure 2.3. The circular punch with a diameter of 1.5in applied compression load to the corrugated sandwich plate during the quasi-static testing. The compression load was applied to the specimen at a constant increasing rate of 1KN/min. The compression load applied to the specimen and the deflections of the corrugated structure were recorded. Two specimens were tested for the each arrangement of the corrugated sandwich plates to keep reliability. Note that the BBBB arrangement wasn't tested.

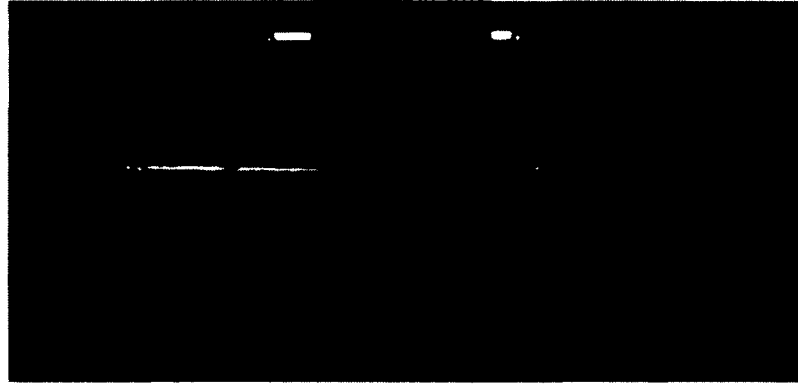


Figure 2.3 Quasi-static testing on corrugated sandwich structures

2.3.2 Quasi-static finite element modeling of corrugated sandwich plates

The quasi-static finite element modeling was solved by ABAQUS/Standard solver. Due to the symmetry of the corrugated sandwich plates, the quarter model was built to save computational time, shown in Figure 2.4. The corrugated model was meshed by C3D8I element, which is the first-order fully integrated C3D8 element enhanced by incompatible modes to improve its bending behavior [83]. The formulation of the first-order fully integrated elements leads to extra shear strain in bending, which is called parasitic shear. The incompatible elements can not only improve the bending behavior but can also reduce the computational time compared to second-order elements. The corrugated layers and the substrates were modeled as tied together during the simulation and no fracture or damage was considered. The support and the punch were modeled as rigid shells meshed with discrete rigid elements. The contacts between the plate and the rigid support, between the plate and the punch were modeled as frictionless in the tangential direction and hard contact in the normal direction. Since solving contact problem in ABAQUS/Standard can cause severe convergence problem, automatic stabilization was used in the contact definition [52].

The punch only had one degree of freedom (DOF) in the z-direction and all the other DOFs were constrained. The loading, which had “smooth” amplitude defined in ABAQUS, was applied on the punch in the simulation. In the quasi-static analysis, the parameter time is to find out the magnitude of the load, doesn’t refer to the real time.

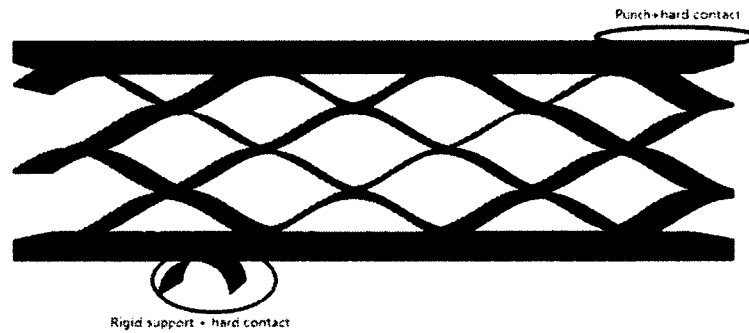


Figure 2.4 Finite element model of 1/4 corrugated sandwich plate

The material properties of the substrate (steel 1018) and the core (steel 1008) were measured by quasi-static testing from Prof. Hebert. The quasi-static stress-strain curves were obtained at a rate of $10^{-3}/s$ in compression. For the elastic region we use well-known material properties for steel such as Young’s modulus=190GPa, Poisson’s ratio=0.3. The bilinear hardening model for steel 1008 and power-law hardening model for steel 1018 were selected and curve-fitted based on the testing data, shown in Figure 2.5. The power-law model for steel 1018 is

$$\sigma = 370 \left(\frac{\varepsilon}{0.00195} \right)^{\frac{1}{8}} MPa \quad (2.1)$$

And that for steel 1008 is

$$\sigma = 200 + 400\varepsilon_p MPa \quad (2.2)$$

Where ε refers to the true strain of steel 1018 and ε_p refers to the equivalent plastic strain of steel 1008.

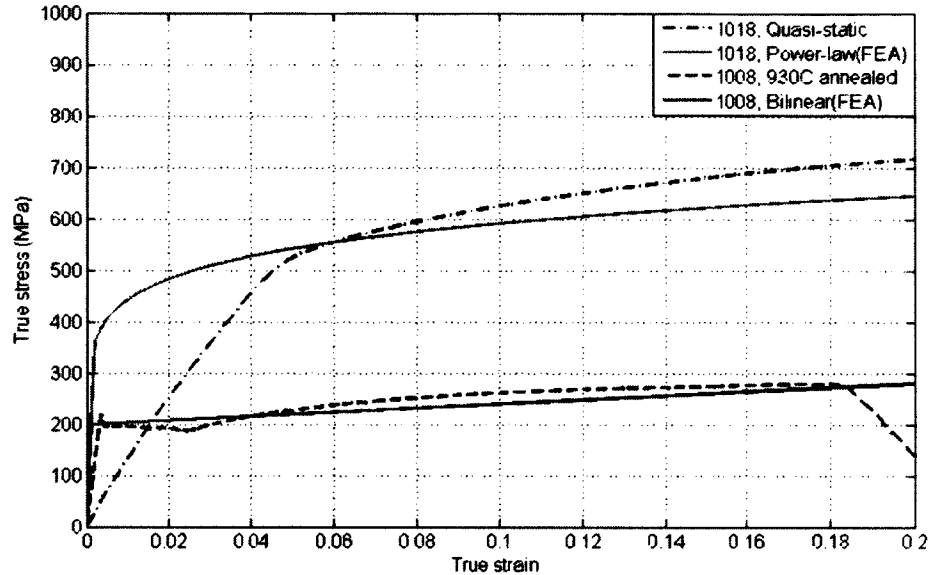


Figure 2.5 Constitutive curves for substrate and core materials

2.3.3 Results and discussion

2.3.3.1 Compression load-deflection curve

The central deflection of the front (facing the punch) face and the corresponding load applied on the structure were recorded from the testing results. Then the compression load-deflection curves were plotted in dotted lines and compared with the simulation results in this section. And the deformation shapes at critical locations are also plotted.

Figure 2.6 shows the compression load-deflection curve for core arrangement AAAA. The deformation of AAAA begins with the overall plate bending as a whole piece. The structure starts to crush layer by layer when the compression load reaches 8775N and no increase in the compression load is observed in the simulation. From the

testing results, the load magnitude to start the crush is lower than the simulation predicted and maintains almost constant. The reason for the load magnitude difference should be the uncertainties in the testing, such as the geometric imperfections and welding conditions between layers.

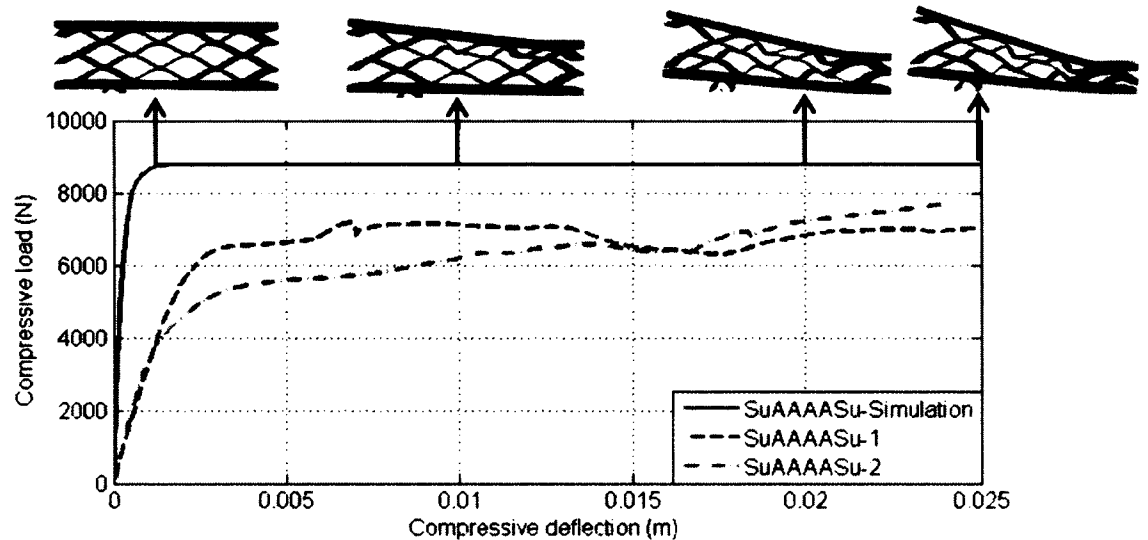


Figure 2.6 Compression load-deflection curve of AAAA core arrangement

Figure 2.7 plots the compression load-deflection curve for core arrangement BBBB. The quasi-static testing wasn't carried out for the BBBB core arrangement. The simulation results of BBBB are quite similar to that of AAAA, except that the load magnitude to start crushing is much smaller, which is around 3857N. We also found that the plate bending and core compression of the corrugated sandwich plate are coupled during the whole process. During the crushing layer by layer, the compression load is increased by a little amount.

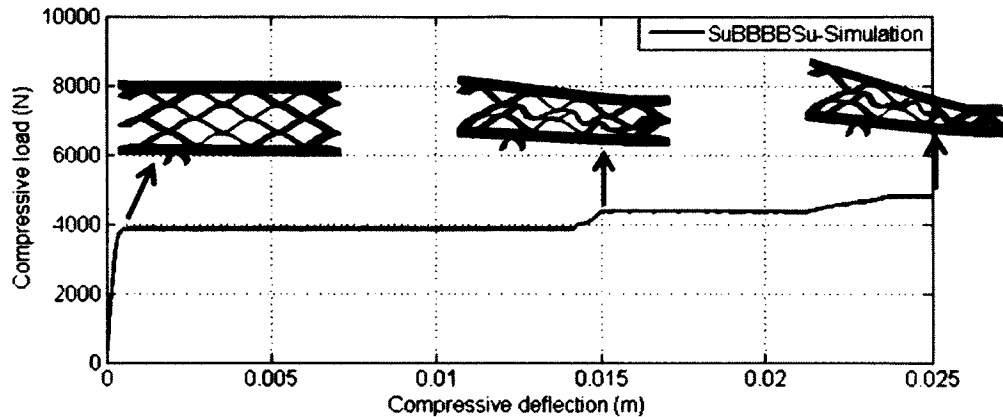


Figure 2.7 Compression load-deflection curve of BBBB core arrangement

Figure 2.8 shows the compression load-deflection curve for CCCC core arrangement. The CCCC arrangement start to crush at a very small load which is around 1159N and the plate bending isn't obvious at the beginning. After the core section gets fully densification, the crushed structure will bend as a monolithic plate. The plate bending phase and bending phase are approximately decoupled for CCCC core arrangement. The load magnitude in simulation is larger than that obtained from testing, which is due to the geometric imperfections and bonding conditions.

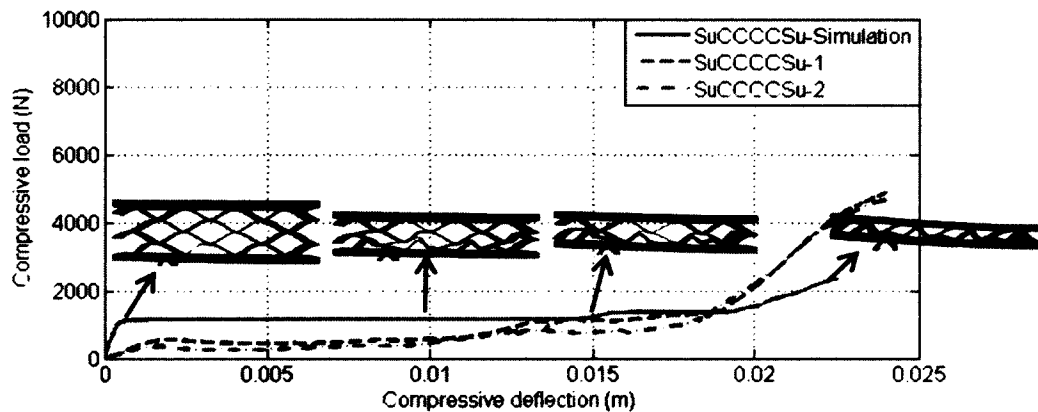


Figure 2.8 Compression load-deflection curve of CCCC core arrangement

For the AABC arrangement, the core is composed with layers with different thicknesses. The crushing happens layer by layer from the front to the back which has the same trend as the testing results, as shown in Figure 2.9. We also find that the layers crush gradually, which is not like the sudden crushing that happens in the arrangement with the uniform corrugated layers. The load for the C layer in the front to get crushed is around 3328N. After the C layer crushed, the plate bending and compression of the layers are coupled.

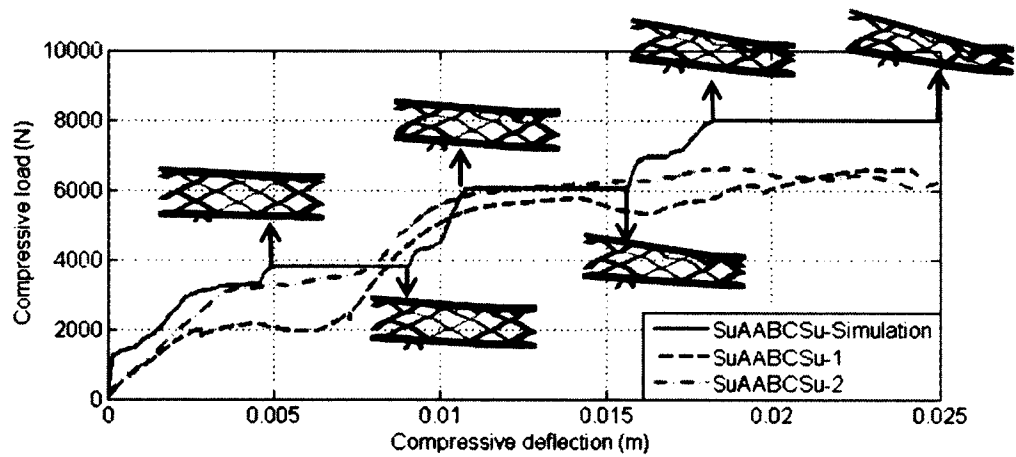


Figure 2.9 Compression load-deflection curve of AABC core arrangement

Figure 2.10 shows the compression load-deflection curve for AACC core arrangement. In this arrangement, we can see that the sudden crush happens for the front two C layers and the compression load to initiate the crushing is around 1241N. Then the corrugated sandwich plate with AACC core arrangement bends as a monolithic plate. At the end, the crush in A layer happens.

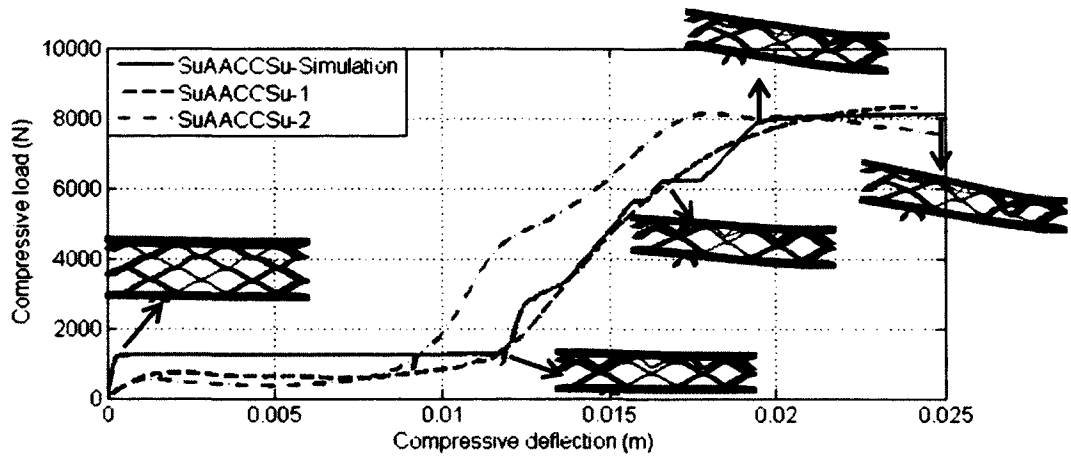


Figure 2.10 Compression load-deflection curve of AACC core arrangement

Figure 2.11 shows the compression load-deflection curve for ABBC core arrangement. Similar to the AABC arrangement, the crushing starting from the front C layer also happens gradually and spreads out layer by layer. The load magnitude for C layer to initiate crushing is around 2820N. After C layer crushed, the plate bending and core compression are coupled.

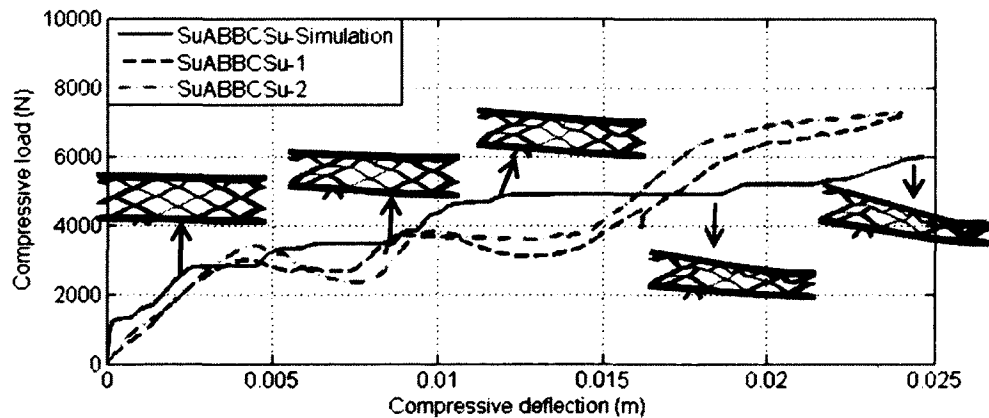


Figure 2.11 Compression load-deflection curve of ABBC core arrangement

Figure 2.12 shows the compression load-deflection curve for ABCC core arrangement. Its behavior is similar to that for AACC. The front two C layers get crushed first and the load to start the crush is around 1177N. After the crush of the C layers, the structure behaves bending as a monolithic plate and core compression at the same time.

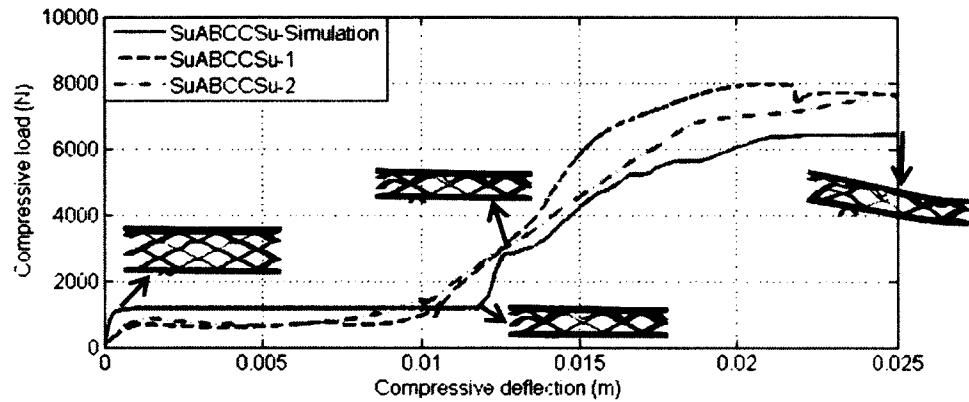
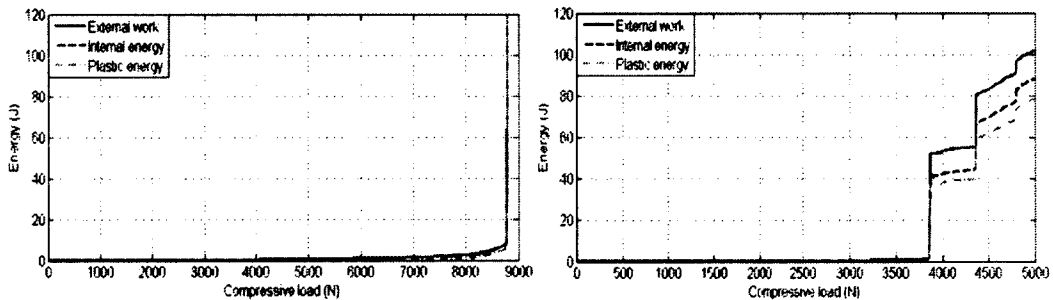


Figure 2.12 Compression load-deflection curve of ABCC core arrangement

2.3.3.2 Energy quantities

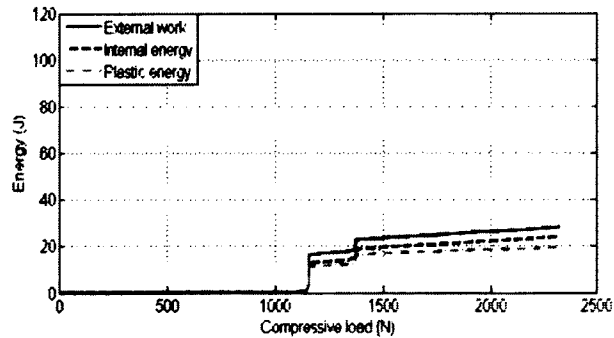
The external work, the internal energy and plastic energy of all the seven core arrangements obtained from the simulation are plotted versus the applied compression load in the following Figure 2.13. The energy distribution and the crushing can be clearly seen from these figures. The jump in the energy plots indicates that the crush is happening. As mentioned before, the difference between the external work and the internal energy is the energy dissipated to stabilize the contact problem in ABAQUS/Standard solver to avoid convergence problem.

Figure 2.13 shows the energy plots versus the compression load for all the seven core arrangements. The crush happens immediately at load 8775N for AAAA core arrangement and only one jump is found in the energy plots. For BBBB and CCCC core arrangements, there are multiple jumps in the energy plots. For all the arrangements with different corrugated layers, there are multiple jumps in the energy plots, which indicate that the crush happens layer by layer. For AACC and ABCC, the loads to start the crushing are very small, similar to that for CCCC. After the two C layers get crushed, the energy smoothly increases as the load goes up, which means the back layers maintains their strength. For ABBC and AABC, the loads to start the crushing are larger than these arrangements with two C layers at the front (facing the punch). The jumps in the energy plots of ABBC and AABC core arrangement are more significant than that of AACC and ABCC core arrangements.



(a)

(b)



(c)

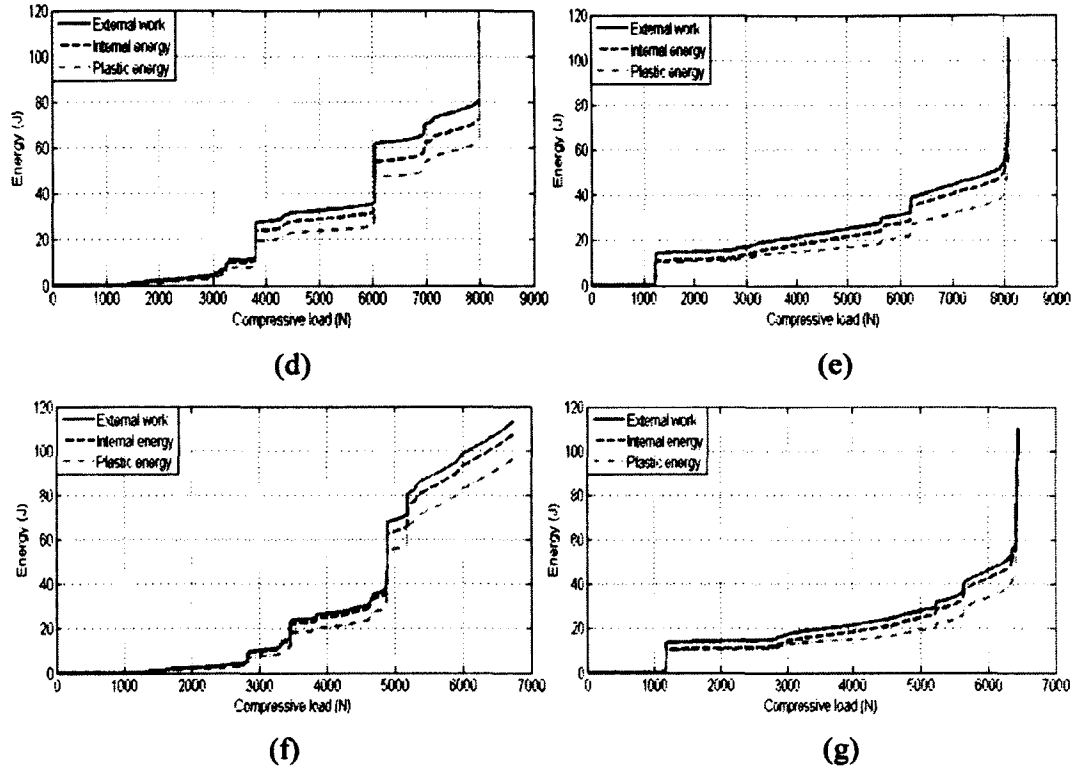


Figure 2.13 Energy plots for (a) AAAA (b) BBBB (c) CCCC (d) AABC (e) AACC (f) ABBC and (g) ABCC core arrangements

2.3.3.3 Comparison and discussion

The load at the beginning of the crushing and the relative density with respect to AAAA for all the core arrangements are summarized in Table 2.1. For the sandwich plates with uniform corrugated layers, the load to start crushing decreases as the relative density decreases. AAAA core arrangement requires the largest load and CCCC core arrangement requires the smallest load to start crushing. But that trend doesn't apply to the sandwich plates with graded corrugated layers. The sandwich plates with two C layers at the front (AACC and ABCC) start crushing at a very small compression load. Among the sandwich plates sharing the same relative density

(BBBB, AACC and ABBC), the load at the beginning of the crushing for BBBB is the largest and that for AACC is the smallest.

Table 2.1 Load to start crushing and relative density for all the core arrangements

Corrugated structure arrangement	Load at the beginning of crushing (N)	Relative density w.r.t AAAA
AAAA	8775	1
BBBB	3857	0.9224
CCCC	1159	0.8339
AABC	3328	0.9437
AACC	1241	0.9224
ABBC	2820	0.9224
ABCC	1177	0.9008

2.4 Shock tube testing of corrugated sandwich plates

The shock tube testing was performed by Prof. Shukla's group at University of Rhode Island and the shock tube apparatus is shown in Figure 2.14. The shock tube is divided into a high-pressure driver section and a low-pressure driven section, which are separated by a destructible diaphragm. The driver section is pressurized with high pressure Helium gas which created a pressure difference across the diaphragm. The pressure difference between these two sections becomes higher when pressurizing the high-pressure driver section. When the pressure difference reaches a critical value, the diaphragm ruptures and the resulting rapid release of gas forms a one-dimensional

shock wave front. When the shock wave reaches the specimen, the dynamic air pressure load is applied to the specimen [44-46].

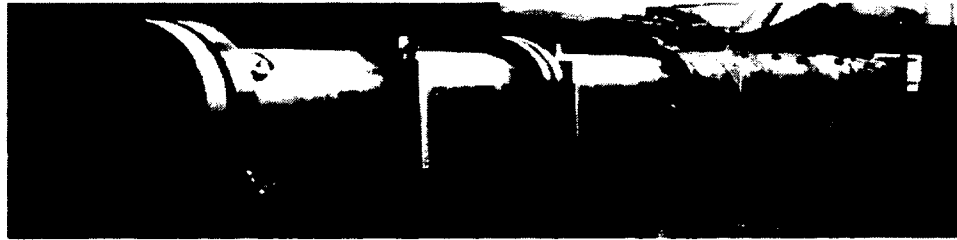


Figure 2.14 The shock tube facility to generate controlled blast loading [47]

The corrugated sandwich plate was simply supported and located with zero stand-off distance from the nozzle, shown in Figure 2.15. The diameter of the muzzle is 1.5in. The span between the two rigid supports was around 6in. Two wires were also used to bond the specimen to the support in order to avoid their separation during the shock tube testing. At least two specimens of each arrangement were tested to ensure reliability.

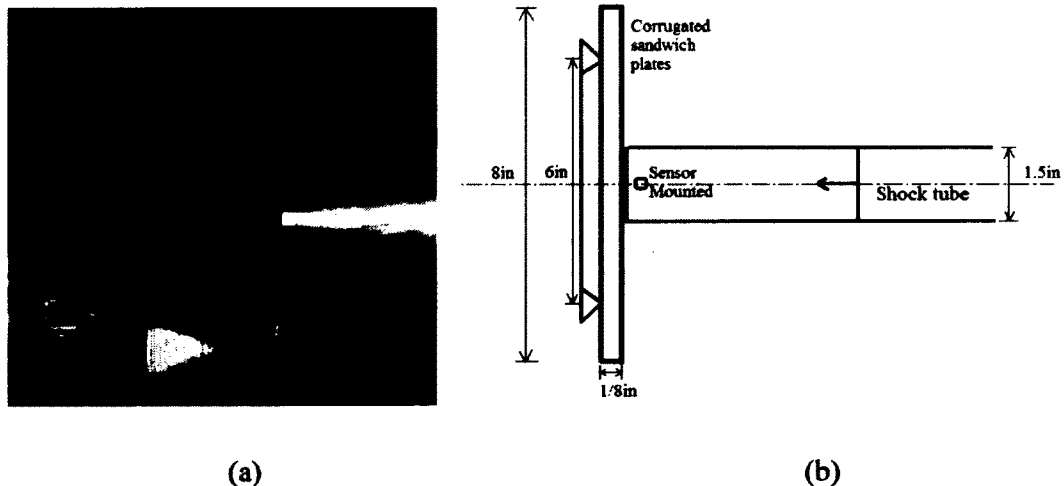


Figure 2.15 (a) Fixture of the corrugated sandwich plate during shock tube testing (b) a schematic plot of shock tube testing

There were two pressure transducers (PCB102A) mounted at the end of the muzzle section to record the incident and reflected pressure profiles. The first pressure sensor was mounted 20 mm away and the second was mounted 180 mm away from the muzzle, shown in Figure 2.16.

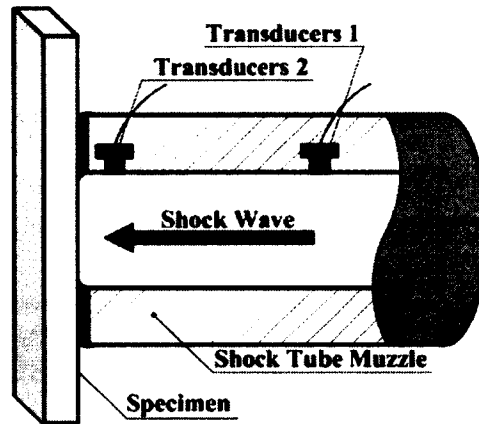


Figure 2.16 The muzzle setup [53]

A typical pressure profile including the incident shock pressure and reflected shock pressure measured during the shock tube testing is shown in Figure 2.17. In the following section, the reflected pressure measured by the first pressure sensor which was mounted 20mm away from the muzzle is used in the finite element modeling.

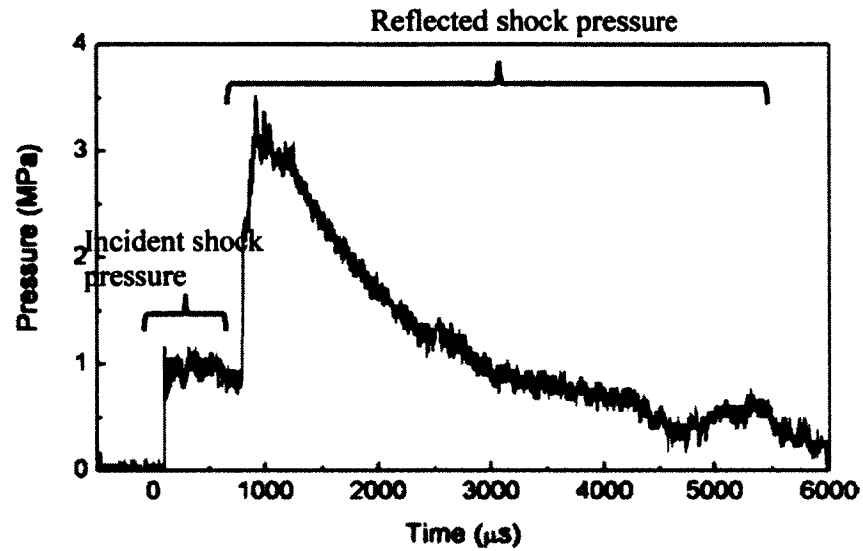
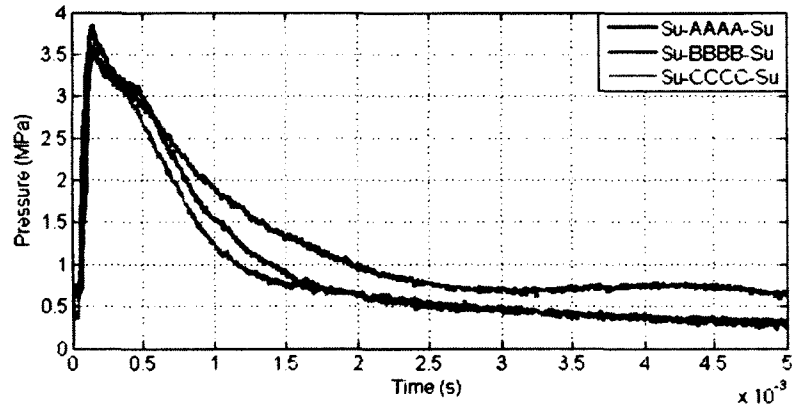
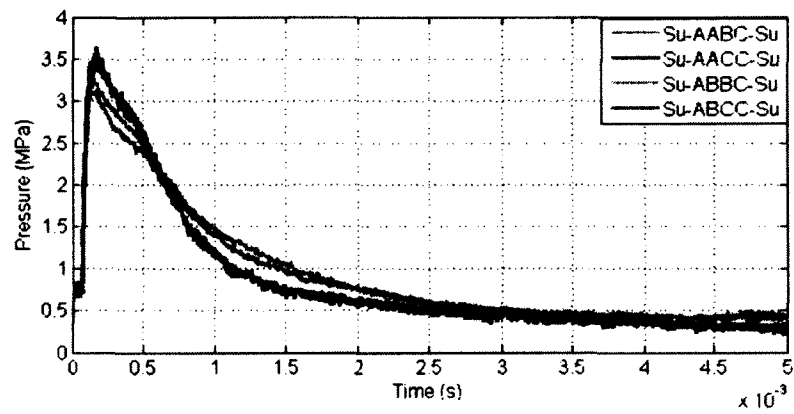


Figure 2.17 Typical measured shock tube pressure profile [53]

The incident peak pressure of the shock wave was chosen to be 0.70 MPa in this study, but due to the fluid-structure interaction happened during the shock tube testing, the reflected pressure profiles for different corrugated sandwich plates measured by the first sensor were different, shown in Figure 2.18. From Figure 2.18(a), we found that pressure for CCCC (soft core) has the smallest magnitude and time duration, while pressure for AAAA has largest magnitude and time duration. The soft core transmits less impulse than the strong core, which is consistent with Tilbrook's work [37]. For the sandwich plates with two C layers at the front side (facing the shock tube) (AACC and ABCC), the peak pressure magnitudes are larger than these of AABC and ABBC but time durations are smaller.



(a)



(b)

Figure 2.18 Reflected pressure profile measured by the sensor during shock tube testing for (a) AAAA, BBBB and CCCC (b) AABC, AACC, ABBC and ABCC core arrangements

A high-speed camera system was used to record the motion of the corrugated sandwich plates in order to determine the deflection and velocity histories. The camera system was placed perpendicular to the shock tube, shown in Figure 2.19. The camera was a Photron SA1 high-speed digital camera which has the ability to capture images at a framing rate of 20,000 fps with an image resolution of 512x512 pixels for

2 second time duration [53]. The deformed shapes, deflection and velocity histories at the center of the front and back faces were obtained based on the sequential images which are taken by the high-speed camera system during shock tube testing.

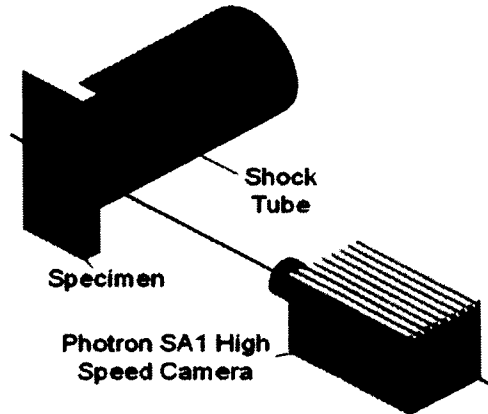


Figure 2.19 Placement of camera system w.r.t the shock tube and specimen [53]

2.5 Finite element modeling of corrugated sandwich plates subjected to shock tube loading

2.5.1 Finite element modeling

The commercial package ABAQUS was used in this work for the finite element simulations. Due to the symmetry of the corrugated structures, the quarter model was built to reduce computational time, shown in Figure 2.20. The corrugated model was meshed by C3D8I elements. The support was modeled as rigid body which was also meshed with C3D8I element. The C3D8I element is the first-order fully integrated C3D8 element enhanced by incompatible modes to improve its bending behavior. The formulation of the first-order fully integrated elements leads to extra shear strain in bending, which is called parasitic shear. The incompatible elements can not only improve the bending analysis but can also reduce the computational time compared to

second-order elements [83]. The total number of elements was around 58,000 and the total number of nodes was around 80,000. There were three layers of elements along the thickness direction of each corrugated layer.

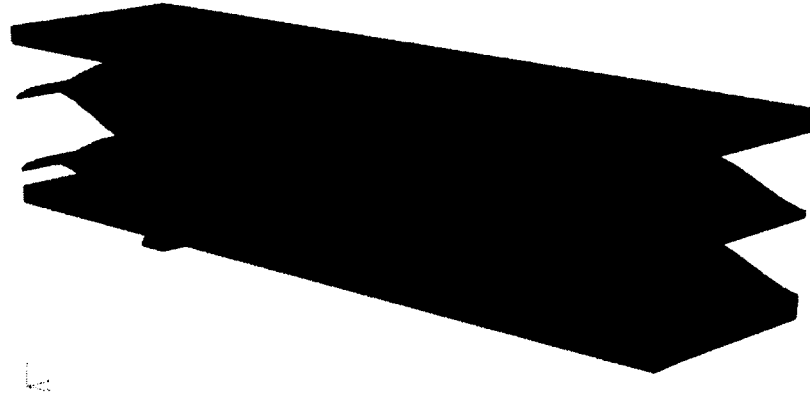


Figure 2.20 Finite element modeling of the corrugated sandwich plates

The contact between the specimen and the rigid support was defined as frictionless in the tangential direction and hard contact in the normal direction. Since there were wires bonding the support and specimen together, the separation between specimen and support was not allowed in the contact definition. The substrates and corrugated layers were modeled as tied together all the time during the simulation without considering the failure, such as debonding between layers and fracture damage.

Due to the high density dynamic air pressure loading during shock tube testing, the explicit algorithm was selected and its stability was guaranteed in this simulation. And for all the simulations, the energy balance was checked out. Besides, the damping in dynamic finite element simulation is very important. There are a number of built-in damping options available in ABAQUS: material damping, modal damping, structural damping and bulk viscosity. In ABAQUS/Explicit, bulk viscosity

is introduced to control high frequency oscillations [52]. Since oscillations at high frequencies were not obvious in our simulation, the default values of bulk viscosity were implemented. For the material damping, since the elastic-plastic material behavior was defined, there was no need to introduce additional material damping. The reason is that material damping is often insignificant when compared to the plastic dissipative effect, since the energy is mainly dissipated in the form of plastic deformation.

2.5.2 Rate-dependent material property obtained by SHPB testing and its implementation into ABAQUS

The Split-Hopkinson Pressure Bar (SHPB) Technique was used in this work to obtain the constitutive relations of steel 1018 for various high strain rates at room temperature. This methodology is popular for this type of test due to its ease of use and ability to decouple inertia from strain rate effects [54, 55]. Based upon the one-dimension wave propagation theory, the stress-strain curves for different strain rates can be obtained. The stress-strain curves of steel 1018 under strain rates (2000/s, 2500/s and 3100/s) obtained from SHPB tests as well as the quasi-static stress-strain curve obtained by quasi-static testing are shown in Figure 2.21. Based on the material properties of steel 1018 obtained by SHPB testing, the bilinear hardening curve with linear strain-rate dependence was selected for material model of steel 1018 used in the finite element simulation. The Young's modulus is 190G and the plastic model for steel 1018 implemented in the ABAQUS was defined as

$$\sigma = (500 + 200 \varepsilon^{p'}) (1 + 0.0003 \dot{\varepsilon}^{p'}) \text{MPa} \quad (2.3)$$

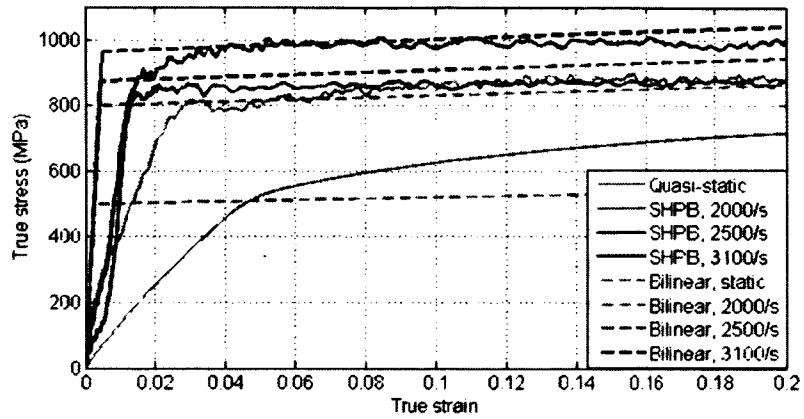


Figure 2.21 Stress-strain curves of steel 1018 at different strain rates

The quasi-static constitutive curve for steel 1008 was obtained by quasi-static testing and bilinear hardening model was also selected. Since steel 1008 and steel 1018 are both low-carbon steel, steel 1008 was assumed to share similar strain-hardening behavior and strain-rate dependence, shown in Figure 2.22. The Young's modulus is around 190G and the plastic model for steel 1008 implemented in the ABAQUS was defined as

$$\sigma = (200 + 400 \varepsilon^{pl})(1 + 0.0003 \dot{\varepsilon}^{pl}) \text{ MPa} \quad (2.4)$$

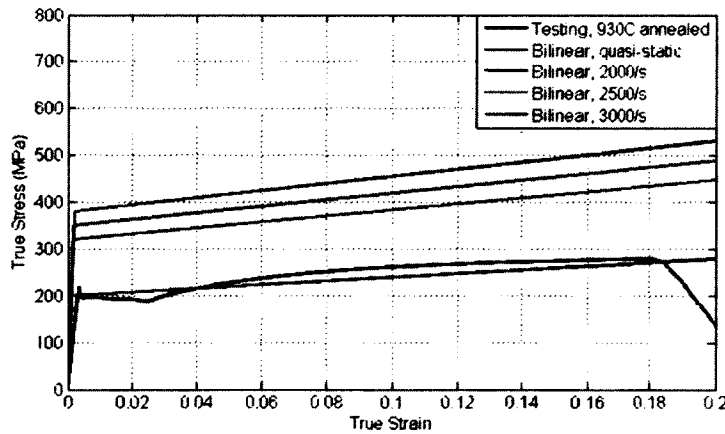


Figure 2.22 Stress-strain curves of steel 1008 at different strain rates

2.5.3 Loading approximation

Due to the fluid-structure interaction, it is very challenging to determine the spatial distribution of the pressure loading at each time increment from the shock tube experiment. We observe that when the plate undergoes large deformation, the actual loading area is extended to beyond the muzzle area and the pressure loading at the extended area decays as it moves outward from the shock tube muzzle (see the paper [56] for more information). In this part, we didn't not perform fluid-structure analysis but approximated the spatial distribution of the pressure load which may be able fit such interaction. In this work, the radius of the loading area was extended from 0.75in (radius of muzzle) to 1.5in, shown in Figure 2.23. The pressure load at the muzzle area was approximately the same as the measured pressure loading, as shown in Figure 2.18. And the pressure load in the extended area was assumed to have a linear decay behavior.

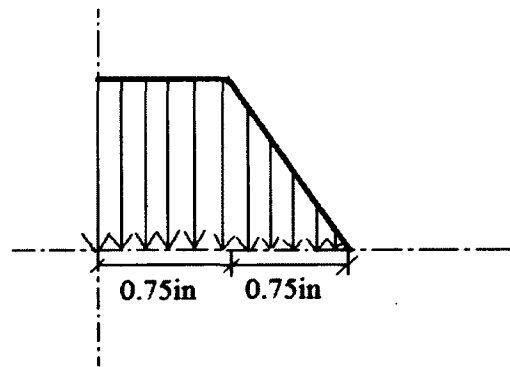


Figure 2.23 Spatial distribution of the shock tube loading

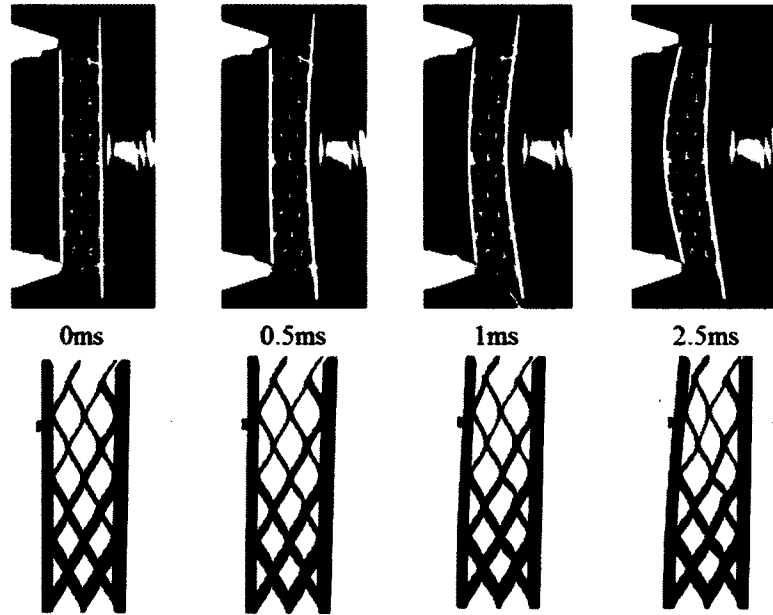
2.6 Results and discussion of corrugated sandwich plates subjected to shock tube loading

2.6.1 Deformed shapes and mid-span deflection histories

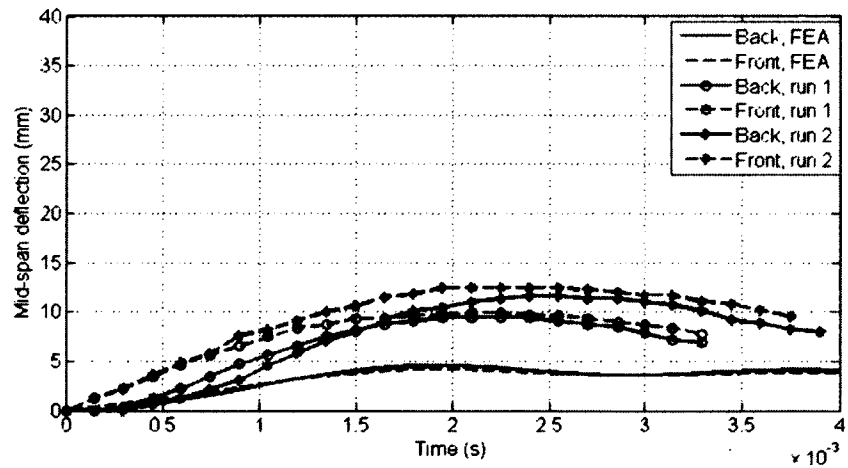
The high-speed camera system was able to record the real-time history of the shock tube testing by taking sequential photos at a framing rate of 20,000fps. The real-time deformed shapes of the each arrangement were obtained based on the sequential images and compared with these obtained from the finite element simulation at critical times. Besides, the deflection histories at the center of the front (facing the shock tube) and back faces for the corrugated sandwich plates was measured from the sequential photos and compared with these obtained from the finite element simulation. Overall, the simulation results match with testing results.

Figure 2.24 shows the deformed shapes and mid-span deflection histories for AAAA core arrangement at critical times. The simulation results show the same trend of the deformed shapes as the shock tube testing, shown in Figure 2.24(a). The compression of the core section is very little and happens mainly at the top and bottom regions of the specimen. We can see that the whole corrugated structure is dominated by the elastic plate bending. From the photos obtained by the high-speed camera system, the weld breakage in shear is found at the bottom and top most welds on the back face plate. The mid-span deflection histories of AAAA core arrangement are shown in Figure 2.24(b). The simulation results match very well with the testing results. The back face starts to deform around 0.2ms after the shock tube loading applied. The maximum deflections happen around 2.25ms in the experiment, while the maximum deflection happens around 2ms in the simulation. The maximum back face deflection obtained from the simulation is much smaller than that obtained from the testing. That

may be due to the pressure loading approximation, the difference in modeling the bonding between layers and geometric imperfection in the testing specimen.



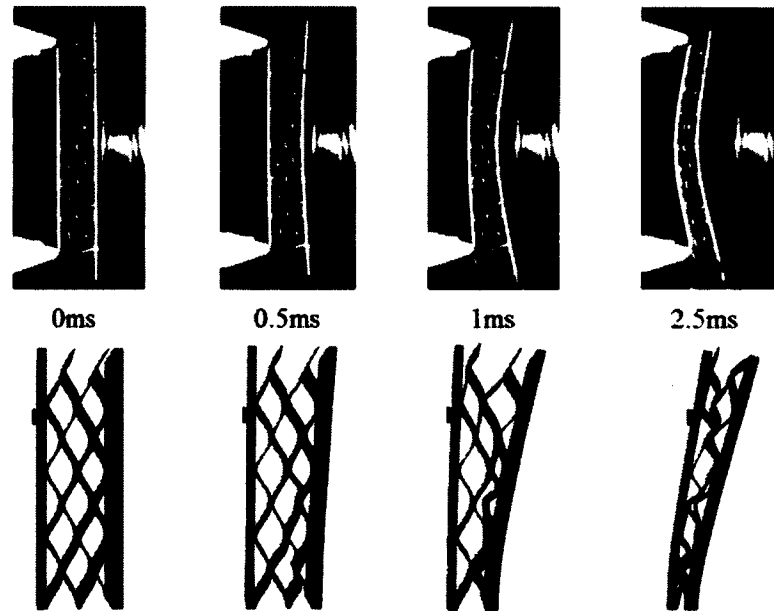
(a)



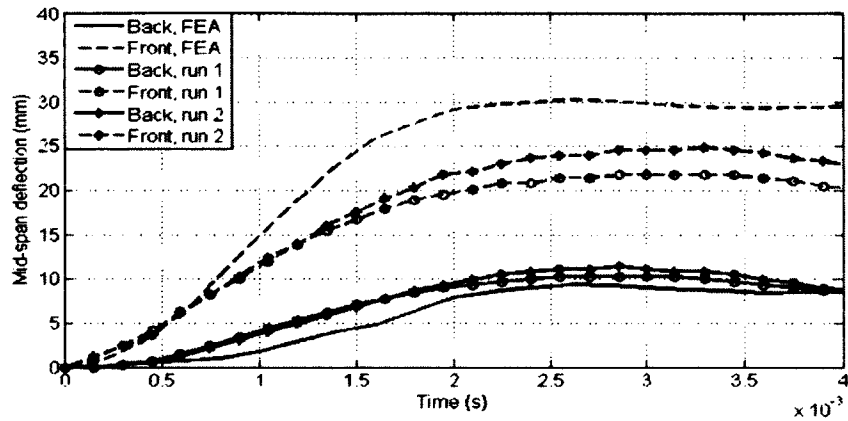
(b)

Figure 2.24 (a) Deformed shapes for AAAA core arrangement at critical times (b) Mid-span deflection histories of front and back face for AAAA core arrangement

Figure 2.25 shows the deformed shapes and mid-span deflection histories of BBBB core arrangement at critical times. Initially, the corrugated plate shows global elastic deformation. Since BBBB arrangement has uniform corrugated layers in the core, it is difficult to predict which layer is going to fail first, shown in Figure 2.25(a). But we can see from the simulation results and testing results that after crushing begin, the core crushing and plate bending are coupled. The back face starts to bend around 0.5ms after the initial front face deformation. At the beginning, the mid-span deflection histories of back and front face obtained from simulation and testing are similar, shown in Figure 2.25(b). After around 1ms, the deflection difference between simulation and testing gets larger. From the photos of the shock tube testing, the welding breakages are found, which lead to the deformation difference.



(a)

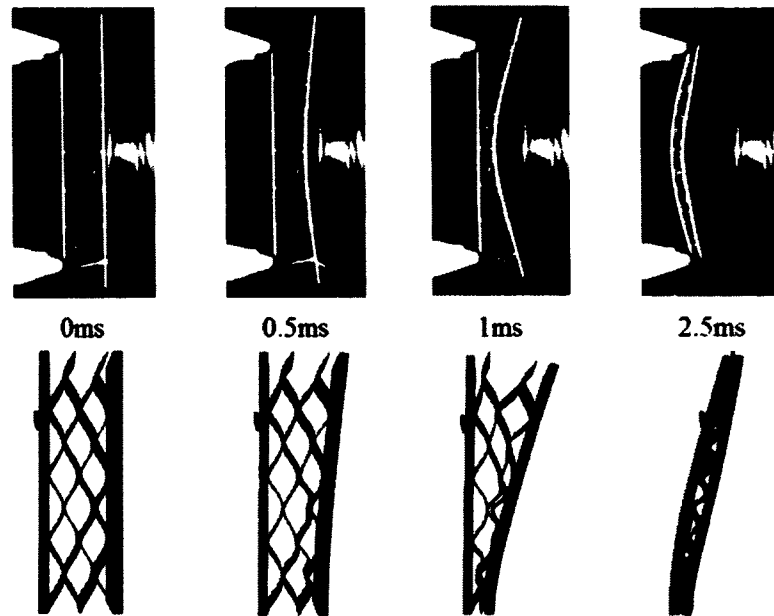


(b)

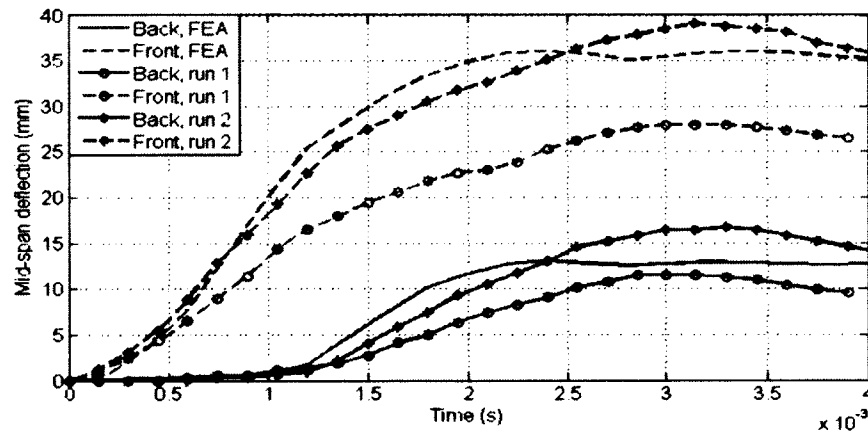
Figure 2.25 (a) Deformed shapes for BBBB core arrangement at critical times (b)

Mid-span deflection histories of front and back face for BBBB core arrangement

Figure 2.26 shows the deformed shapes and mid-span deflection histories for CCCC core arrangement at critical times. The simulation results match very well with the shock tube testing results. At the beginning, the CCCC case shows the core crushing in the corrugated layers happens much easier than AAAA and BBBB arrangements. That the crushing happens from the front face to the back face is observed from both simulation and testing. The crushing happens at the central region of the CCCC core first and then spread out to the top and bottom regions. After all the core section is fully collapsed which happens around 2.5ms, the plate behaves global bending as a monolithic plate. The core crushing and plate bending phases are decoupled in CCCC arrangement before its central region of the core gets fully crushed. The back face deflection starts to increase greatly around 1.1ms after the shock tube loading applied. The welding breakages are found all over the core section in the shock tube testing. These breakages may lead to the deflection difference, especially after 2.25ms.



(a)

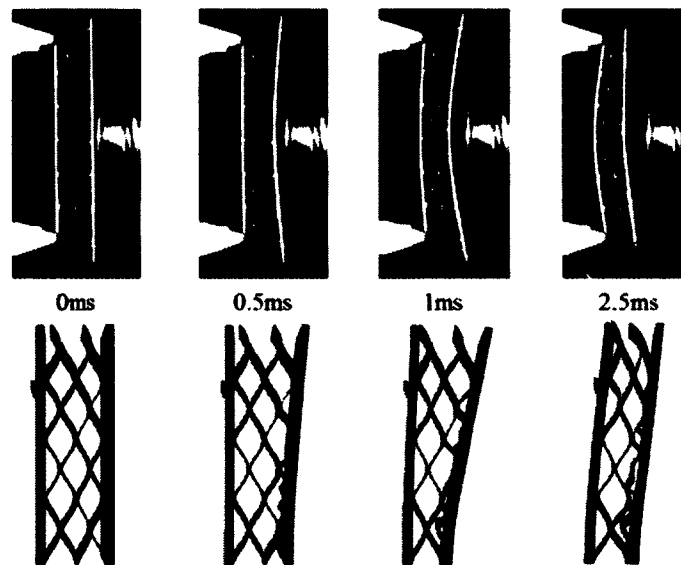


(b)

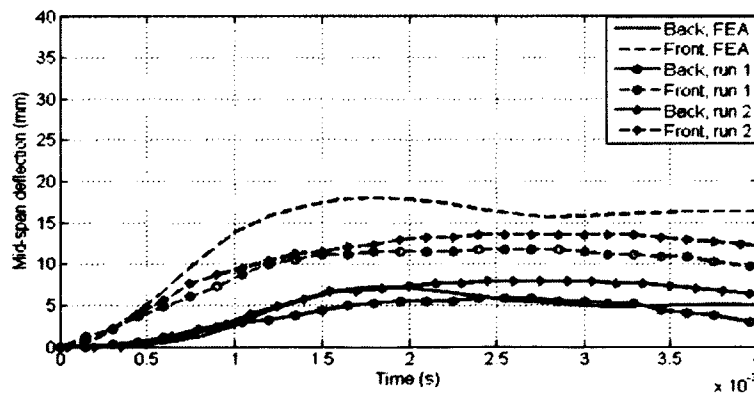
Figure 2.26 (a) Deformed shapes for CCCC core arrangement at critical times (b) Mid-span deflection histories of front and back face for CCCC core arrangement

The deformed shapes and mid-span deflection histories for the AABC core arrangement are shown in Figure 2.27. From simulation and testing, the C layer starts

crushing immediately and then B layer starts to collapse about 0.4ms after the C layer gets crushed. Till the end of the procedure, the A layers don't get crushed. The back face deflection starts to increase greatly around 0.7ms after the shock tube loading applied. After the C layer gets collapsed, the plate bending and corrugated layers' crushing are coupled. It is observed from the testing that the fracture damage and welding breakages mainly happen in the C layer. The deflection difference between simulation and testing gets larger after the damage happens.



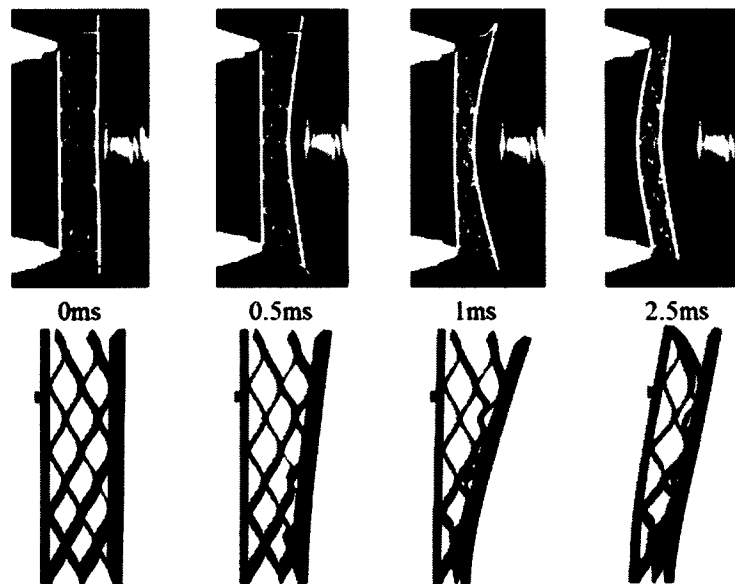
(a)



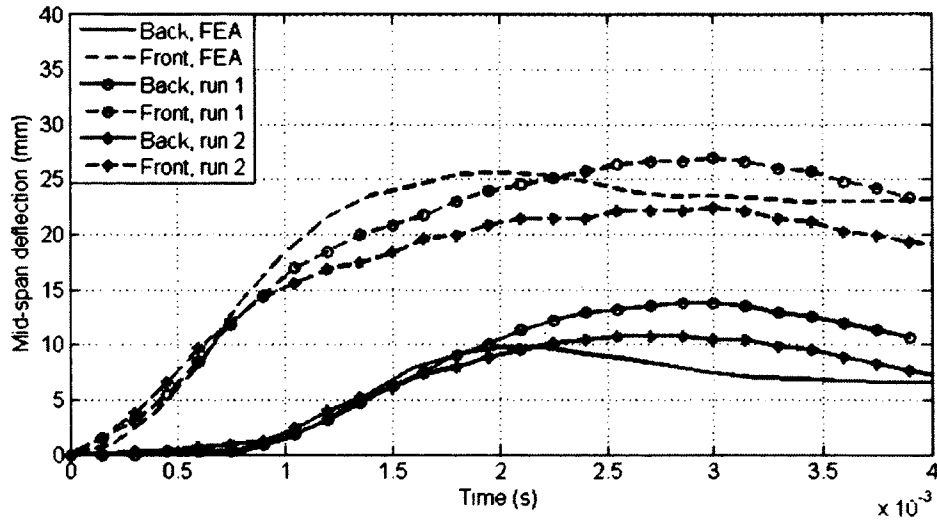
(b)

Figure 2.27 (a) Deformed shapes for AABC core arrangement at critical times (b)
Mid-span deflection histories of front and back face for AABC core arrangement

Figure 2.28 illustrates the deformed shapes and mid-span deflection histories for AACC core arrangement during shock tube testing and finite element simulation. C layers close to the front face start to crush very quickly. After the C layers get crushed, plate bending and core crushing are coupled. The back face deflection increases greatly around 0.85ms after the initial front face deflection. The only welding breakages are found on the back face from the shock tube testing.



(a)



(b)

Figure 2.28 (a) Deformed shapes for AACC core arrangement at critical times (b) Mid-span deflection histories of front and back face for AACC core arrangement

Figure 2.29 shows the deformed shapes and mid-span deflection histories of ABBC core arrangement at critical times obtained from the testing and finite element simulation. We found that the simulation results match with the testing results. In ABBC model, it is clear that the deformation of the corrugated layers happened layer by layer, from the front layer (C layer) to the back layer (A layer). The back face deflection happens around 0.7ms after the shock tube loading applied. From the photos from the shock tube testing, welding breakages and fracture are found at the C layer after it gets fully collapsed.

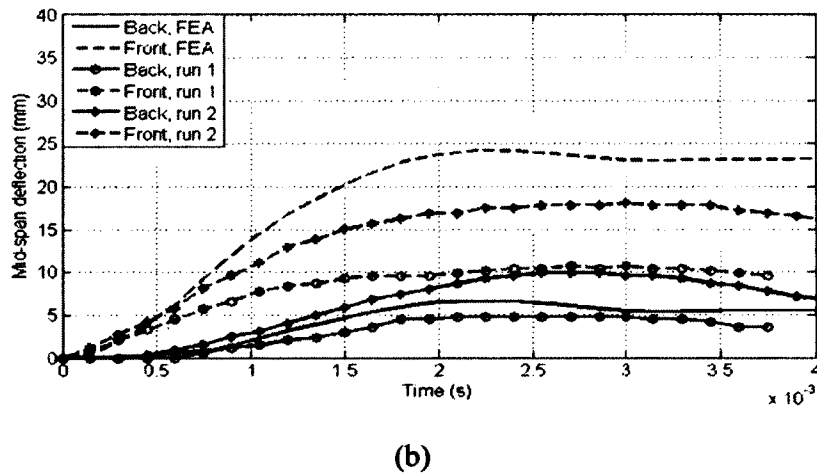
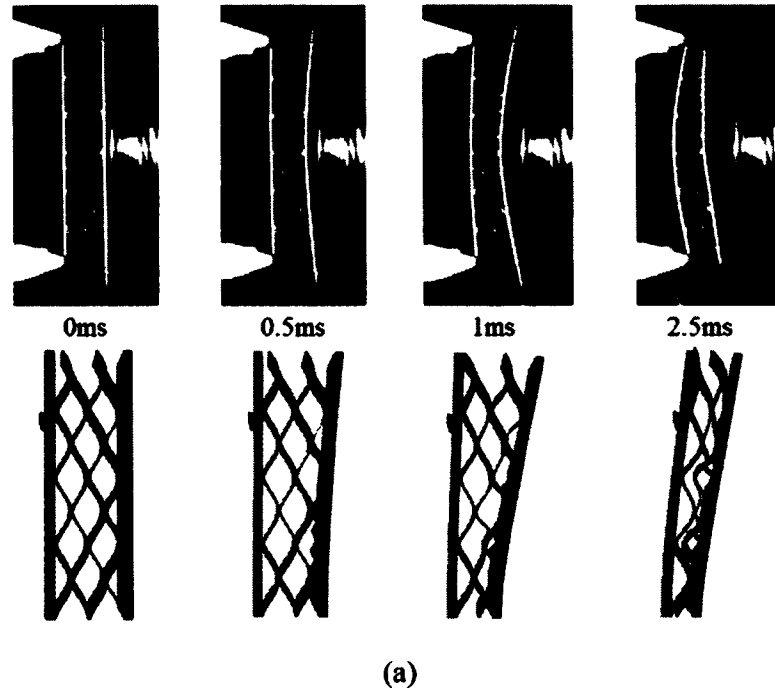
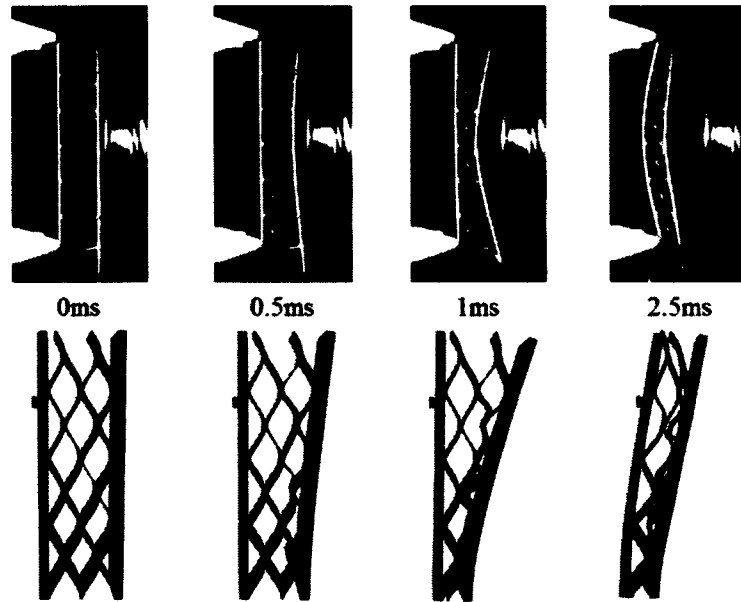


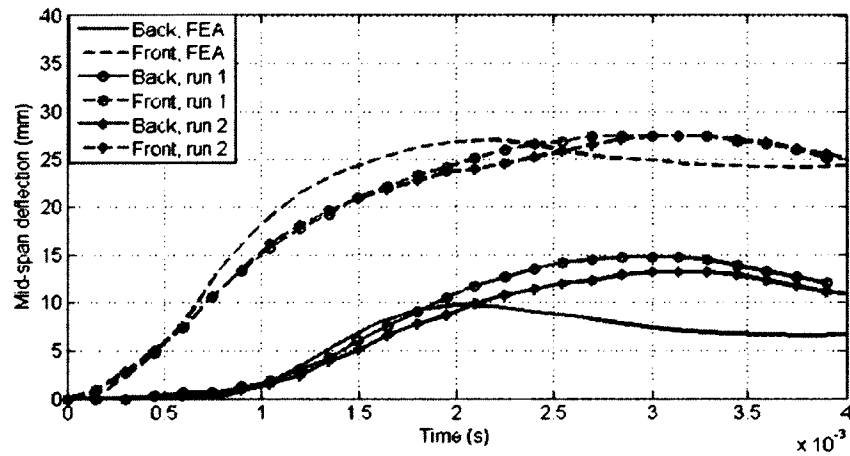
Figure 2.29 (a) Deformed shapes for ABBC core arrangement at critical times (b) Mid-span deflection histories of front and back face for ABBC core arrangement

The deformed shapes and back face deflection histories for ABCC core arrangement from shock tube testing and finite element simulation are shown in Figure 2.30. The front C layers get fully crushed first around time 1ms. After these two layers get crushed, the crushing in the back layers and the plate bending happen at the same

time. The back face deflection increases greatly around 0.85ms after the initial front face deflection. The only welding breakages are found at the back face sheet from the shock tube testing.



(a)



(b)

Figure 2.30 (a) Deformed shapes for ABCC core arrangement at critical times (b) Mid-span deflection histories of front and back face for ABCC core arrangement

We can see that all the deflection histories obtained from the simulations behave similarly to these from the shock tube testing, except that the deflection magnitude for AAAA core arrangement from simulation is much smaller than that from shock tube testing. One cause of this difference can be the limitation of the spatial distribution of pressure loading. From the real-time deformation photos, we can see that there is fracture happening during the shock tube testing. Since the fracture is not considered in the simulation, this can be another cause for the difference between simulation and testing for AAAA. Besides, the geometric imperfections in the specimen are not considered.

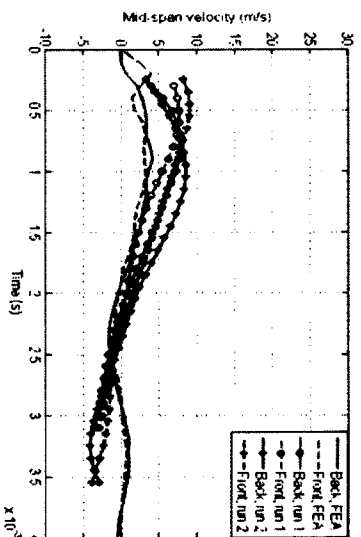
One key parameter evaluating the performance of the sandwich plates is the magnitude of the maximum back face deflection, which is summarized for all the arrangements in Table 2.2. The simulation results match well with testing results for all cases except for the AAAA arrangement and the causes are discussed. From the simulation, among the corrugated sandwich plates with uniform corrugated layers (AAAA, BBBB and CCCC), the AAAA has the smallest maximum back face deflection and the CCCC has the largest. Since the AAAA has the stronger core and mainly shows an elastic response, the simulation result for AAAA is reasonable. Notice that the arrangements BBBB, AACC and ABBC share the same relative density. Among these models sharing same relative density, the ABBC model which has the graded layers with gradually transition between layers has the smallest value of maximum back face deflection.

Table 2.2 Maximum back face deflection of corrugated sandwich plates

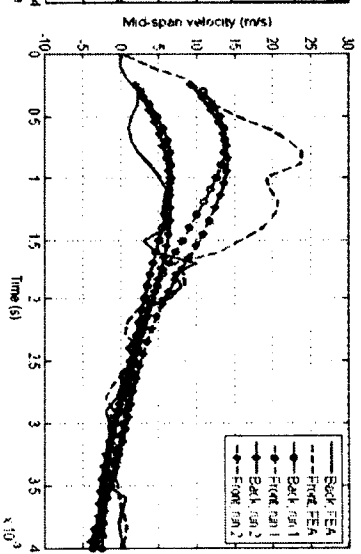
	AAAA	BBBB	CCCC	AABC	AACC	ABBC	ABCC
Back face deflection (BFD) from experiment (mm)	10.3	10.3	14.9	6.6	10.8	5.1	11.7
BFD from simulation(mm)	4.5	9.4	13.1	7.2	9.8	6.6	9.8

2.6.2 Velocity histories at the center of front and back faces

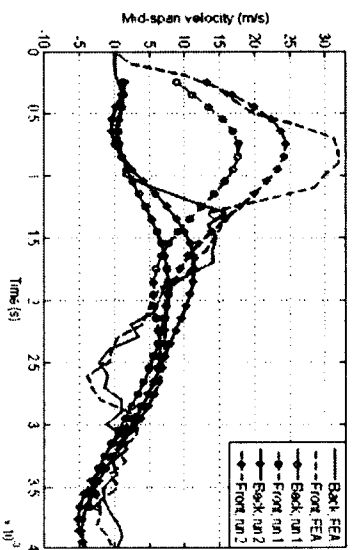
The velocity histories at the center of the front and back faces for the corrugated sandwich plates obtained from the shock tube testing and the finite element simulations are plotted and compared in Figure 2.31. Overall, the simulation results share the same trend with the testing results. For the corrugated model with uniform corrugated layers, the AAAA has the smallest magnitude of velocity and CCCC has the largest. The velocity was obtained by the derivatives of the deflection history plots, which leads to higher-order errors. As a result, the difference of the velocity histories between the simulation and testing is larger than that of the deflection histories.



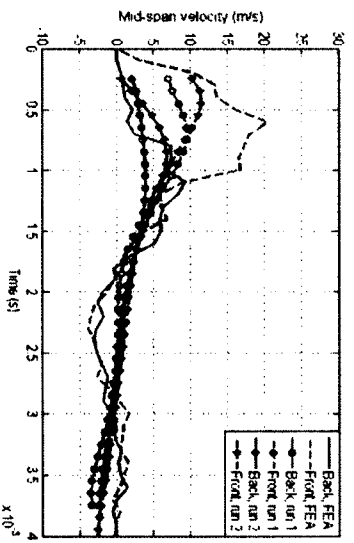
(a)



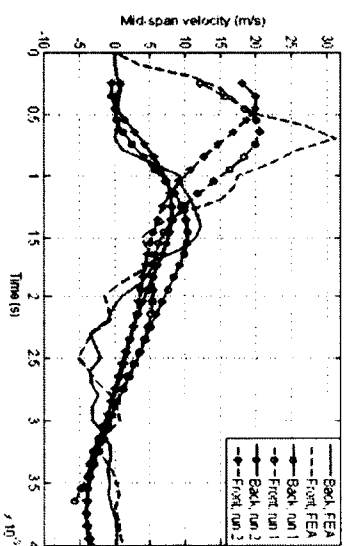
(b)



(c)



(d)



(e)

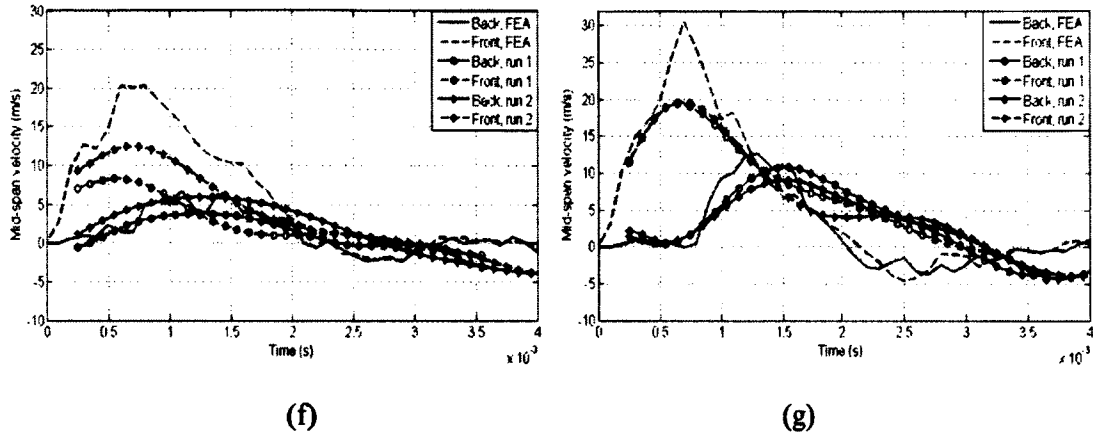


Figure 2.31 Velocity histories for (a) AAAA (b) BBBB (c) CCCC (d) AABC (e) AACC (f) ABBC and (g) ABCC core arrangements

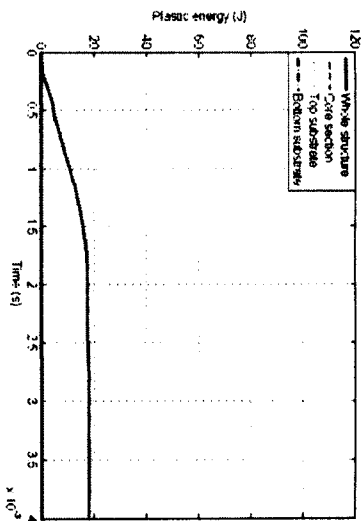
The maximum back face velocity is another important parameter to evaluate the corrugated sandwich plates. The maximum back-face velocities for all the arrangements are summarized in Table 2.3. We can see that the simulation results have the same trend as the testing results, except the AAAA case. In the simulation results, the AAAA has the smallest back face velocity among all the models. The difference between testing and simulation for AAAA arrangement may be due to the limitation of the loading approximation, the imperfection of the corrugated sandwich plates and uncertainties during the shock tube testing. It is also noticed that among the models sharing the same relative density (BBBB, AACC and ABBC), the ABBC with relatively smoothly graded core has the smallest value of back face velocity.

Table 2.3 Maximum back face velocity of corrugated sandwich plates

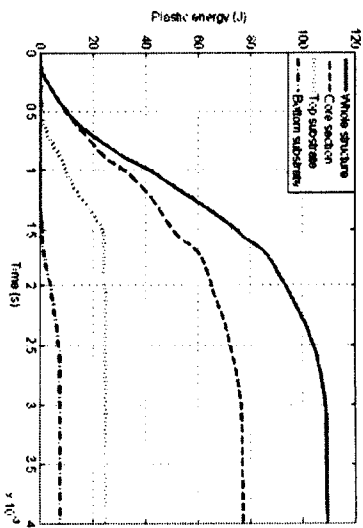
	AAAA	BBBB	CCCC	AABC	AACC	ABBC	ABCC
Back face velocity (BFV) from experiment (m/s)	8.2	6.6	9.5	5.4	9.2	4.9	10.0
BFD from simulation (m/s)	4.2	10.0	18.2	9.5	13.3	6.7	12.7

2.6.3 Energy plots

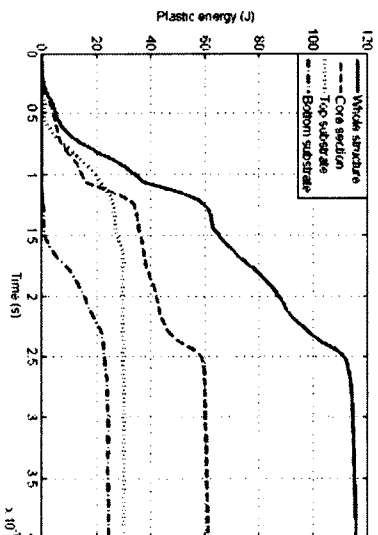
Figure 2.32 shows the plastic energy plots for the seven corrugated core arrangements obtained from the finite element simulation. For the corrugated sandwich plates with uniform corrugated layers, the AAAA arrangement absorbs the least energy and CCCC arrangement absorbs the most. The plastic energy absorbed by AAAA is all absorbed by the core section. And as the corrugated layers become thinner, the percentage of plastic energy absorbed by core section gets smaller, as seen in BBBB and CCCC core arrangements. Among the corrugated models with different corrugated layers, AABC and ABBC that with relatively smoothly graded layers absorb less plastic energy than the other two arrangements (AACC and ABCC). The values of the energy absorption for all the arrangement are summarized in Table 2.4.



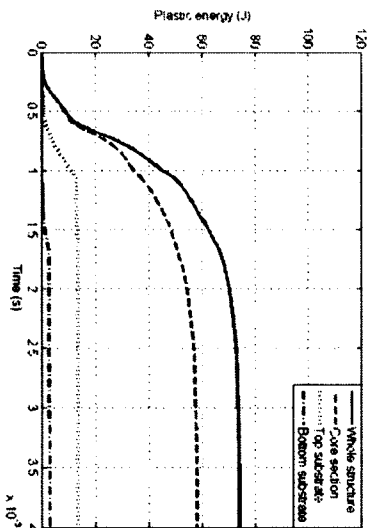
(a)



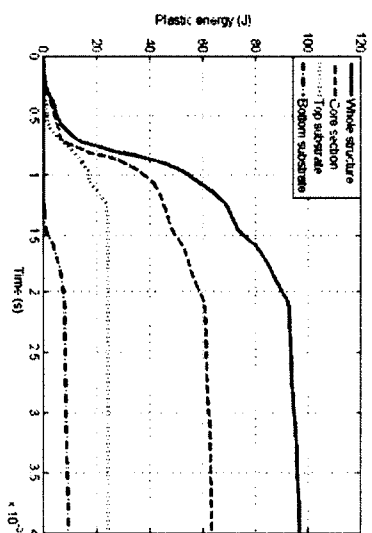
(b)



(c)



(d)



(e)

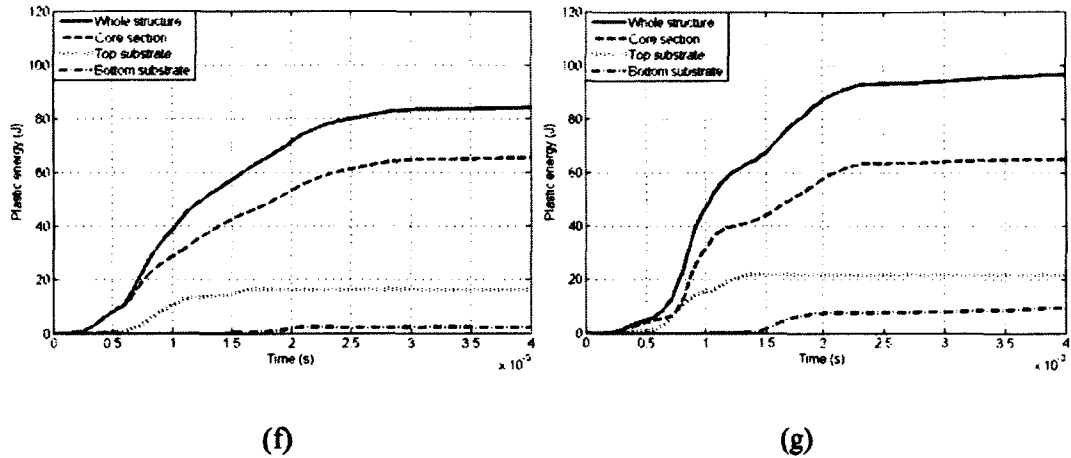


Figure 2.32 Plastic energy absorption by substrates and core for (a) AAAA (b) BBBB (c) CCCC (d) AABC (e) AACC (f) ABBC and (g) ABCC core arrangements

The plastic energy absorption distribution on the core section, front and back substrates are demonstrated in Table 2.4. For the corrugated sandwich plates composed of uniform layers, the percentage of plastic energy absorbed by core section reduce as the thickness of the layers reduces. Correspondingly, larger percent of plastic energy are absorbed by front and back substrates.

Among the sandwich plates with different corrugated layers, the plates with two C layers absorbs smaller percent of plastic energy in the core and leave more plastic energy absorbed by front and back substrates. For the plates sharing the same mass (BBBB, AACC and ABBC), the ABBC has smallest energy absorption percentage at the back substrate, which is desired in the design of sandwich plates.

Table 2.4 Plastic energy absorption distribution after the corrugated plates reach a stable status

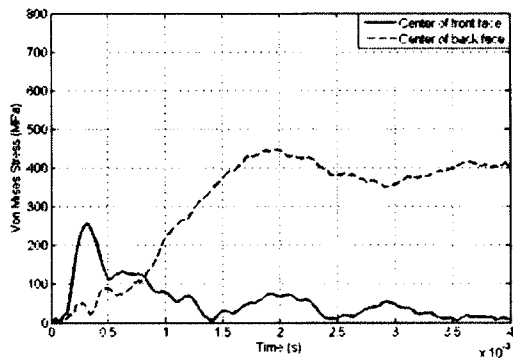
	Plastic energy absorption (J)	Percentage (%) absorbed by Core section	Percentage (%) absorbed by Front substrate	Percentage (%) absorbed by Back substrate
AAAA	18.0	100	0	0
BBBB	108.8	70.4	22.8	6.8
CCCC	115.1	52.7	26.2	21.1
AABC	73.8	78.5	17.9	3.6
AACC	95.8	65.6	25.2	9.2
ABBC	83.8	77.7	19.6	2.7
ABCC	95.5	67.9	22.9	9.2

2.6.4 Von Mises stress histories at critical locations

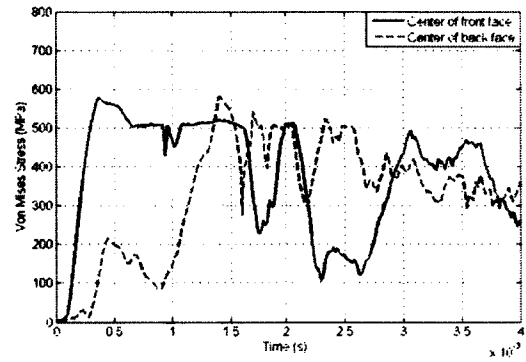
The von Mises stress histories at the center of front and back face for all the different arrangements are shown in Figure 2.33. For AAAA case, we can see that the von Mises stresses are below the yield stress for substrates, which shows that no yielding happens at the center of front and back faces. For all the other cases except AAAA, the von Mises stresses reach the yield stress of the substrate, which indicates that there is yielding at the center of the front and back faces.

For the AAAA arrangement, the stress wave reaches the back face immediately and the stress at the back face is much larger than that at the front face when the plate reaches a stable status. For the BBBB case, the von Mises stress at the front face reaches its maximum value immediately, and after a lag time around 0.25ms, the

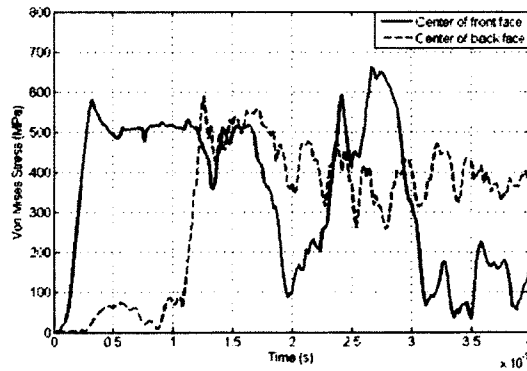
stress at the back face starts to increase. Similar behavior is found for CCCC case, but the lag time is even longer, which is around 1ms. For the sandwich plates with different corrugated layers, AABC and ABBC with relatively smoothly graded layers have a lag time smaller than that of AACC and ABCC. Besides, for BBBB and all the sandwich plates with different corrugated layers, the stresses for front and back faces become similar when the core's densification ends.



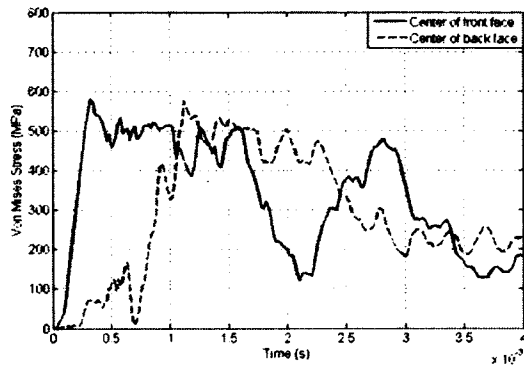
(a)



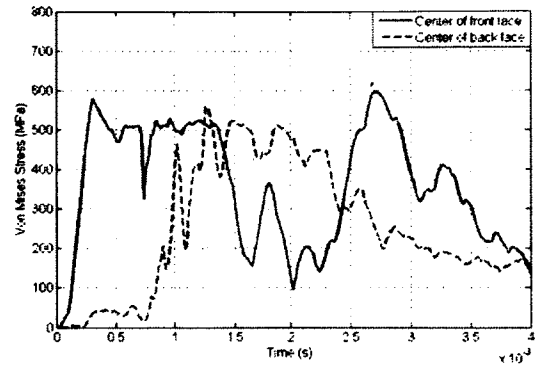
(b)



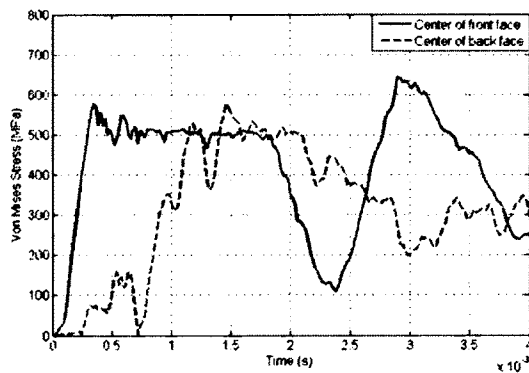
(c)



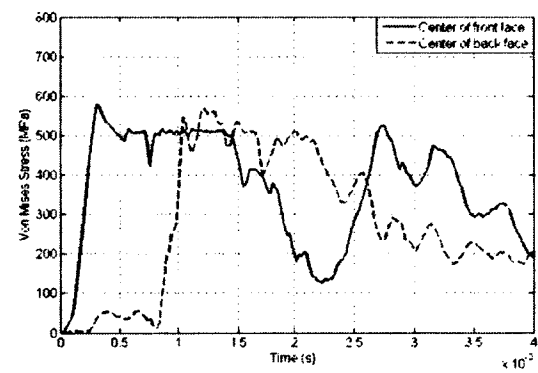
(d)



(e)



(f)



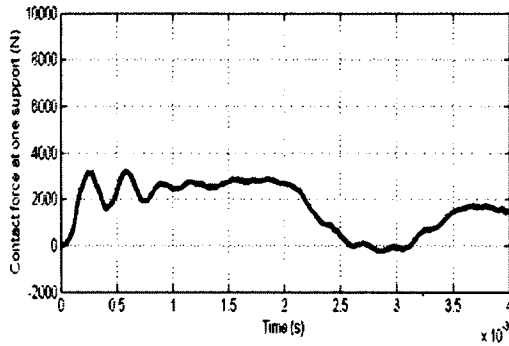
(g)

Figure 2.33 Von Mises stress histories at the center of front and back face for (a) AAAA (b) BBBB (c) CCCC (d) AABC (e) AACC (f) ABBC and (g) ABCC core arrangements

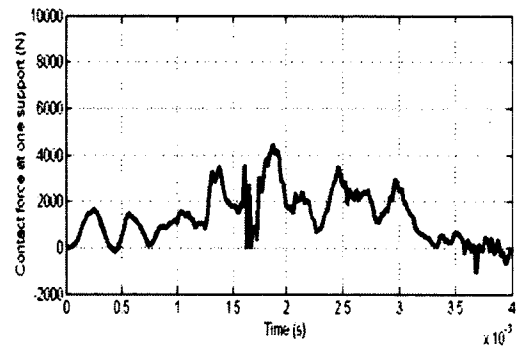
2.6.5 Contact reaction force between support and corrugated sandwich plate

The contact reaction force between the support and the specimen for all the arrangements are plotted in Figure 2.34. Since the separation in the normal direction between the support and the corrugated sandwich plate is not allowed, the contact force may have a negative value at some time. The AAAA case and ABBC case have smaller values of the maximum contact force. CCCC arrangement has the largest

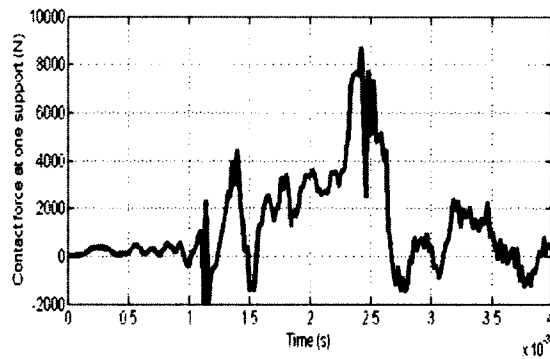
maximum contact force. But the contact force for AAAA reaches its maximum value much quicker than all the other arrangements. All the cases except AAAA arrangement reach maximum contact reaction force after their cores get crushed. At 4ms, the contact force for all the cases except AAAA are all approaching zero.



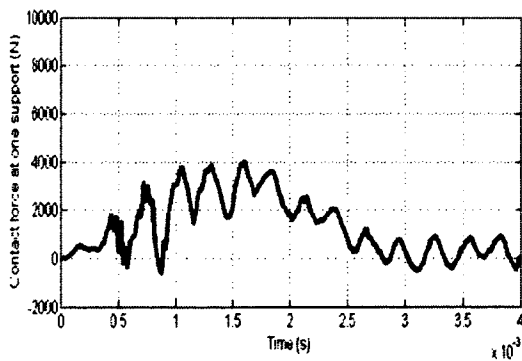
(a)



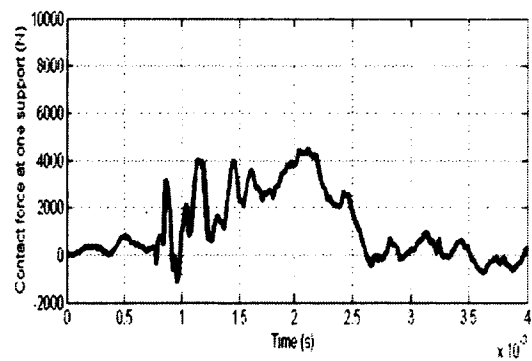
(b)



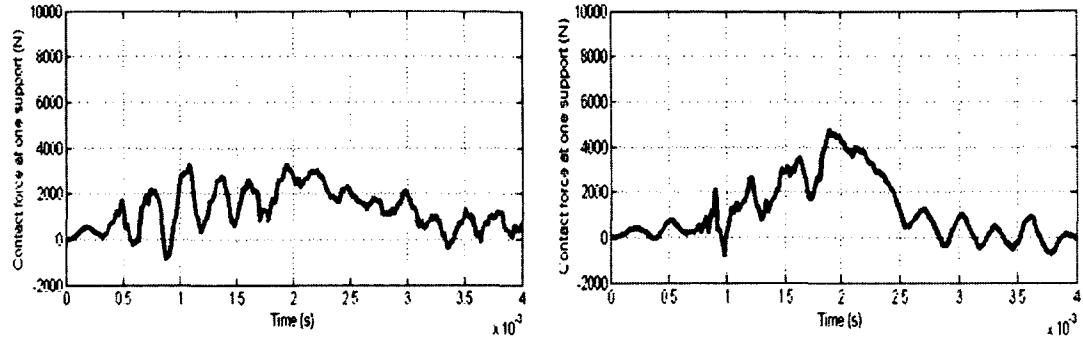
(c)



(d)



(e)



(f)

(g)

Figure 2.34 Contact reaction force between the specimen and support for (a) AAAA (b) BBBB (c) CCCC (d) AABC (e) AACC (f) ABBC and (g) ABCC core arrangements

Table 2.5 Impulse transmitted from sandwich plate to one support till 4ms

Corrugated structure arrangement	Transmitted impulse (Ns)
AAAA	6.6854
BBBB	5.2500
CCCC	4.9134
AABC	5.1536
AACC	4.6634
ABBC	5.1585
ABCC	4.6677

To better evaluate the contact between the support and corrugated sandwich plates, the impulse that transmitted from the plate to one support till 4ms are summarized in Table 2.5. For the sandwich plates with uniform corrugated layers, as the thickness of

the layers gets smaller, the impulse transmitted to the support is smaller. For the sandwich plates with different corrugated layers, the cases with two C layers transmit less impulse to the support than the other two cases. Generally, soft cores transmit less impulse to the support.

2.7 Concluding remarks

This work focuses on the dynamic finite element analysis on sandwich plates with different corrugated layer arrangements under blast loading generated by shock tube facility. The validation data obtained from the shock tube testing by the group of Prof. Shukla is also included in this work. The back face deflection, back face velocity, plastic energy absorption, von Mises stress and the contact force for all the corrugated sandwich plates are discussed. From the discussions, we found the following facts:

- 1) **Maximum back face deflection:** For the sandwich plates with uniform corrugated layers, stronger core leads to smaller maximum back face deflection. Among the sandwich plates sharing the same mass (BBBB, AACC and ABBC), the ABBC with relatively smoothly graded core has the smallest maximum back face deflection.
- 2) **Maximum back face velocity:** For the sandwich plates with uniform corrugated layers, stronger core leads to smaller maximum back face velocity. Among the sandwich plates sharing the same mass (BBBB, AACC and ABBC), the ABBC core arrangement has the smallest maximum back face velocity.
- 3) **Plastic energy absorption:** Among the sandwich plates with uniform corrugated layers, softer core leads to larger amount of plastic energy absorption, but smaller

percentage of plastic energy absorption in the core section. For the sandwich plates with different corrugated layers, the cases with two C layers at the front absorb more plastic energy and smaller percent of the plastic energy is absorbed in the core. Among all the cases, the ABBC case with relatively smoothly graded corrugated layers absorbs the least plastic energy in the back substrate.

- 4) Von Mises stress histories at the center of front and back faces: Sandwich plates with soft cores delays the stress wave to reach the back face. The front and back face don't yield for AAAA arrangement, while those for all the other cases reach the yielding status.
- 5) Contact force and impulse transmitted to support: The AAAA and ABBC have smaller magnitude of maximum contact force between sandwich plate and support. Among the sandwich plates with uniform corrugated layers, softer core leads to smaller impulse transmitted to the support.

Overall, the ABBC sandwich plate with relatively smoothly graded corrugated layers benefits the performance of the sandwich plates under shock tube loading.

Besides, the quasi-static analysis and testing are also carried out on corrugated sandwich plates. Compression load-deflection curves and energy plots are compared and discussed. For the sandwich plates with uniform corrugated layers, the load to start crushing decreases as the relative density decreases. For the sandwich structures sharing the same relative density (BBBB, AACC and ABBC), the loads to initiate the crushing for BBBB is the largest and that for AACC is the smallest.

Chapter 3 - A Parametric Study on Blast-resistant Corrugated and Trapezoid Sandwich Structures

3.1 Introduction

The blast-resistant composites or structures are gaining more and more industrial and academic interests. The blast-resistant composites and structures mainly include the metal-foams [27], sandwich structures [28] and polymers [29]. This work focuses on utilizing sandwich structures to mitigate the blast effects on the structures. Many works have been published on the advanced blast-resistant behavior of sandwich structures with different cores, such as the trapezoid, corrugated, honeycomb, tetrahedral, trusses and pyramidal cores [23, 30-34].

The majority of these works are on the dynamic responses of sandwich beam or plate subjected to blast loading. Fleck and Deshpande brought up a three-phase analytical model for sandwich beam: 1) the fluid structure interaction phase; 2) core compression phase and 3) beam bending and longitudinal stretching phase [34]. The objective of sandwich plate design and optimization is to minimize the back face deflection, minimize the core compression, increase the energy absorption and reduce the support reactions [37]. The works of Liang *et al.* [38] and Tilbrook *et al.* [37] found that the soft core with a low transverse strength reduces the transmitted impulse during the fluid-structure interaction stage for water blast and increases the coupling between core compression phase and beam bending phase. But the soft core can get fully crushed and give a very high support reaction.

A few researches have been done on the blast-resistant structures with graded foam or foam-like and polymer cores. An experimental investigation on sandwich beams with a piece-wise functionally graded (density) core was performed by Avila [48]. The work of Apetre *et al.* on the impact damage of sandwich structures with a graded core has shown that a reasonable core design can effectively reduce the shear forces and strains within the structures [49]. Shukla *et al.* performed shock tube experiment to study the dynamic response of sandwich panels with E-Glass Vinyl Ester (EVE) composite face sheets and stepwise graded foam cores [44, 50, 51]. The shock tube testing results indicated that monotonically increasing the wave impedance of the foam core from the front (facing shock tube loading) to the back and reducing the wave impedance mismatch between successive foam layers can greatly enhance the overall blast resistance of sandwich composites.

But there are relatively fewer researches on the one-dimensional crushing of the sandwich structures subjected to uniform blast loading. Xue and Hutchinson investigated the crushing behavior of unit-cell square honeycomb sandwich cores with consideration of geometric imperfections and brought up a continuum model for the core [57]. Ferri *et al.* proposed a two-step representation model for unit cell X-core sandwich panels [58].

In this work, the dynamic responses of the unit-cell corrugated and trapezoid sandwich structures with various core arrangements under idealized air-blast load are investigated and discussed. Besides, the geometric sensitivity of the corrugated and trapezoid sandwich structures is also discussed.

The work is organized as follows: Section 3.2 describes the unit-cell sandwich structures with various corrugated and trapezoid core arrangements. Section 3.3 investigates dynamic responses of unit-cell corrugated and trapezoid sandwich structures under idealized blast loading. Section 3.4 talks about the effect of geometric imperfection on the corrugated and trapezoid sandwich unit cells with BBBB arrangement. And Section 3.5 concludes this work.

3.2 Unit-cell corrugated and trapezoid sandwich structures with various cores

The sandwich structures are designed to attach to the main structural components to mitigate the damage lead by blasts and explosions. The sandwich structures are composed of two substrates on the front (facing the blast loading) and back, and a core section with corrugated layers or trapezoid layers in between. In the previous chapter, the dynamic responses of corrugated sandwich plates under shock tube loading are investigated. In this chapter, the unit cells of the sandwich structures are considered and more details of the sandwich structures are demonstrated in the following.

3.2.1 Unit-cell corrugated sandwich structures

The unit-cell sandwich structures with different corrugated core arrangements with same mass are demonstrated in Figure 3.1. The unit-cell corrugated sandwich structures have two substrates on front and back and the dimensions for the substrates are 26.8mm in length, 25.4mm in width and 3mm in thickness.

The core of the sandwich structures are composed of four corrugated layers. The corrugated layers are curved by a circular die, but after the die is removed, the shape

of the corrugated layers is approximately a half-sine curve rather than a circular curve. The height of each corrugated layer is around 6mm. The thicknesses for the four corrugated layers are not uniform. In the following sections, for the corrugated sandwich structures, A refers to 0.03in (0.75mm), B refers to 0.02in (0.5mm) and C refers to 0.01in (0.25mm). By following different orders of the corrugated layers with various thicknesses and keeping the same mass for all the models, three arrangements of the corrugated sandwich plates used in Chapter 2 are taken into consideration. Nominating the layers from the back substrate to front (facing the blast loading) substrate, the three arrangements can be written as BBBB, AACC and ABBC. Note that the corrugated layer closer to the back face is thicker (check paper [50] for more information). Besides, the sandwich structure with stepwise graded corrugated core arrangement is added into consideration in this chapter. The thicknesses for the corrugated layers in gradually graded model from the back substrate to front substrate are 0.8mm, 0.6mm, 0.4mm and 0.2mm respectively. The thicknesses of the corrugated layers for the four models are summarized in Table 3.1. The height of the unit-cell corrugated sandwich structures is 26mm.

Table 3.1 Layer thickness for unit-cell corrugated sandwich structures

	Layer thickness from back to front (mm)			
BBBB	0.5	0.5	0.5	0.5
AACC	0.75	0.75	0.25	0.25
ABBC	0.75	0.5	0.5	0.25
Gradually graded core	0.8	0.6	0.4	0.2

The substrates are made of steel 1018 as received, while the corrugated layers are made of steel 1008 after heating to 900C and furnace cooling. The material properties and its implementation into finite element simulation will be discussed in details in section 3.2.3. The substrates and the corrugated layers are welded together without damage and fracture consideration.

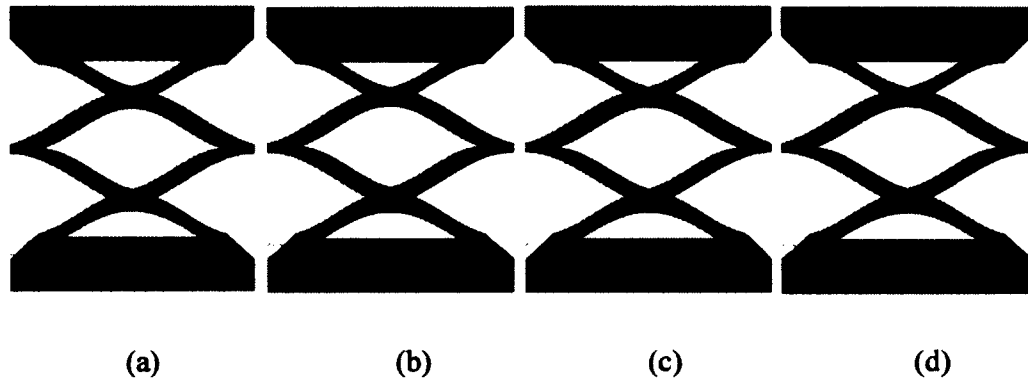


Figure 3.1 Unit-cell corrugated sandwich structures with (a) BBBB (b) AACC (c) ABBC and (d) Gradually graded core arrangements

3.2.2 Unit-cell trapezoid sandwich structures

The unit-cell sandwich structures with trapezoid cores have the same substrates, shown in Figure 3.2. Instead, the layers of the core are trapezoid, which can be manufactured by folding steel plates. The height of the trapezoid layers are also 6mm, the same as corrugated layers. Three different thicknesses for the trapezoid layers following the same ratios for the corrugated layers are considered and the masses for the trapezoid layers are kept the same as that for the corresponding corrugated layers. So for the sandwich structures with trapezoid layers, A refers to 0.633mm, B refers to 0.422mm and C refers to 0.211mm for the thicknesses. Similarly, the gradually graded trapezoid core arrangement is also considered in this work. The thicknesses

for the trapezoid layers from the back substrate to front substrate are 0.675mm, 0.506mm, 0.338mm and 0.169mm respectively. The thicknesses of the trapezoid layers for the four models are summarized in Table 3.2. The height of the unit-cell corrugated sandwich structures is 25.7mm.

Table 3.2 Layer thickness for unit-cell trapezoid sandwich structures

	Layer thickness from back to front (mm)			
BBBB	0.422	0.422	0.422	0.422
AACC	0.633	0.633	0.211	0.211
ABBC	0.633	0.422	0.422	0.211
Gradually graded core	0.675	0.506	0.338	0.169

The substrates are made of steel 1018 as received, while the corrugated layers are made of steel 1008 after heating to 900C and furnace cooling. The material properties and its implementation into finite element simulation will be discussed in details in section 3.2.3. The substrates and the corrugated layers are welded together without damage and fracture consideration.

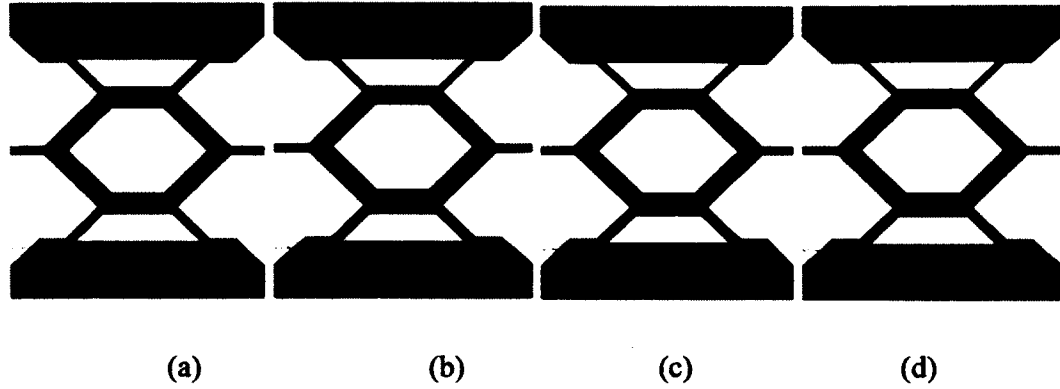


Figure 3.2 Unit-cell trapezoid sandwich structures with (a) BBBB (b) AACC (c) ABBC and (d) Gradually graded core arrangements

3.2.3 Material properties

The Split-Hopkinson Pressure Bar (SHPB) Technique was used in this work to obtain the constitutive relations of steel 1018 for various high strain rates at room temperature. This methodology is popular for this type of test due to its ease of use and ability to decouple inertia from strain rate effects [54, 55]. Based upon the one-dimension wave propagation theory, the stress-strain curves for different strain rates can be obtained. The stress-strain curves of steel 1018 under strain rates (2000/s, 2500/s and 3100/s) obtained from SHPB tests as well as the quasi-static stress-strain curve obtained by quasi-static testing are shown in Figure 3.3. Based on the material properties of steel 1018 obtained by SHPB testing, the bilinear hardening curve with linear strain-rate dependence is selected for material model of steel 1018 used in the finite element simulation. The Young's modulus is 190G and the plastic model for steel 1018 implemented in the ABAQUS/CAE is defined as

$$\sigma = (500 + 200 \varepsilon^{pl})(1 + 0.0003 \dot{\varepsilon}^{pl}) MPa \quad (3.1)$$

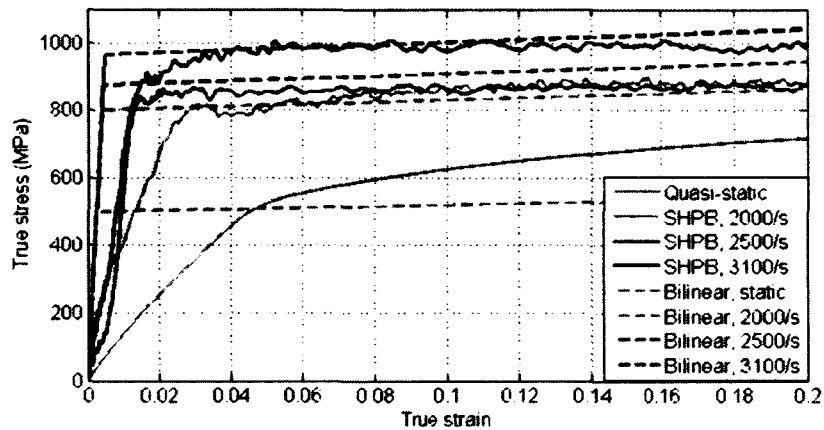


Figure 3.3 Stress-strain curves of steel 1018 at different strain rates

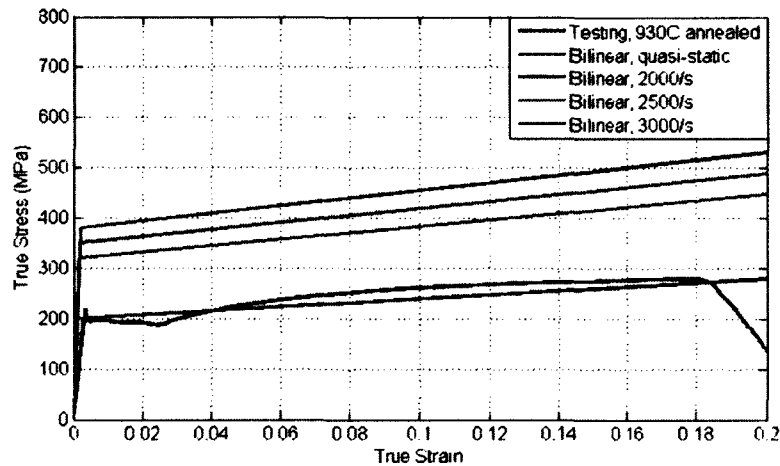


Figure 3.4 Stress-strain curves of steel 1008 at different strain rates

The quasi-static constitutive curve for steel 1008 was obtained by quasi-static testing and bilinear hardening model is also selected. Since steel 1008 and steel 1018 are both low-carbon steel, steel 1008 is assumed to share similar strain-hardening behavior and strain-rate dependence, shown in Figure 3.4. The Young's modulus is around 190G and the plastic model for steel 1008 implemented in the ABAQUS/CAE is defined as

$$\sigma = (200 + 400 \varepsilon^{p'}) (1 + 0.0003 \dot{\varepsilon}^{p'}) \text{ MPa} \quad (3.2)$$

3.3 Dynamic responses of unit-cell corrugated and trapezoid sandwich structures with various core arrangements under idealized blast loading

3.3.1 Idealized blast loading

The results presented in this work will be for the dynamic responses of unit-cell sandwich structures subjected to impulsive blast-type loads. Generally, the time history for the blast pressure is an exponential decaying curve and has a very short time duration in the order of 10^{-6} to 10^{-3} seconds [6]. If the period of the pressure pulse acting on the structure is short compared to the response time of the plate, the pressure pulse imposed on the structure can be replaced by an initial impulse [21]. Previously, Taylor [22, 59] used the solution for a one-dimensional wave pulse impinging on a solid to compute the momentum transmitted to the free-standing plate by the blast pulse. Based on Taylor's theory, the fluid-structure interaction doesn't affect much on the momentum transmitted to the plates subjected to typical air blast, since the response time for the plate is much larger than the pressure pulse duration and the plate can be treated as a rigid wall. Similarly, in this work, it is reasonable to compare the dynamic responses under same air-blast pressure pulse as under same transmitted impulse to the unit cells.

In this work, the impulse I is transmitted to the unit-cell sandwich structures at time=0. For the monolithic solid plate, this impulse is distributed uniformly through the thickness as a uniform initial velocity normal to the plate, $v = I/m$, where m refers to the mass of the monolithic solid plate. But for sandwich structures, the

impulse are only applied to the front substrate towards the blast pressure as a uniform initial velocity, where m is the mass for the front substrate [23]. In this work, different levels of impulse or initial velocity (10m/s, 20m/s 30m/s, 40m/s and 50m/s for unit-cell corrugated sandwich structures, and 10m/s, 30m/s, 50m/s, 70m/s and 90m/s for unit-cell trapezoid sandwich structures) are applied to the front substrate of sandwich structures and the dynamic responses are discussed in details.

3.3.2 Finite element modeling

The commercial package ABAQUS was used in this work for the finite element simulations. The unit-cell sandwich structures with corrugated and trapezoid layers were meshed by C3D8I elements. The C3D8I element is the first-order fully integrated C3D8 element enhanced by incompatible modes to improve its bending behavior [83]. The formulation of the first-order fully integrated elements leads to extra shear strain in bending, which is called parasitic shear. The incompatible elements can not only improve the bending analysis but can also reduce the computational time compared to second-order elements [52]. There are three layers of elements along the thickness direction of each layer.

The substrates and corrugated layers were modeled as tied together during the simulation without considering the failure, such as debonding between layers and fracture damage. The self-contact with no friction in tangential direction and hard contact in normal direction was defined for the whole model. The initial velocity was applied on the front substrate and the back substrate was fixed.

The explicit algorithm was selected and its stability was guaranteed in this simulation. And for all the simulations, the energy balance was checked out. Besides, the

damping in dynamic finite element simulation is very important. There are a number of built-in damping options available in ABAQUS: material damping, modal damping, structural damping and bulk viscosity. According to the analysis type, the bulk viscosity and material damping may be implemented. In ABAQUS/Explicit, bulk viscosity is introduced to control high frequency oscillations [52]. Since oscillations at high frequencies are not obvious in our simulation, the default values of bulk viscosity were implemented. For the material damping, since the elastic-plastic material behavior was defined, there was no need to introduce additional material damping. The reason is that material damping is often insignificant when compared to the plastic dissipative effect, since the energy is mainly dissipated in the form of plastic deformation.

3.3.3 Maximum core compression under different initial velocities

Generally, the unit-cell sandwich structures subjected to the initial velocity of the front substrate behave a one-dimensional compression motion. The displacement of the front substrate leads to the compression in the core section. In this section, the maximum core compression of the unit-cell sandwich structures with corrugated and trapezoid cores are discussed and the corresponding deformed shapes are also demonstrated.

3.3.3.1 Unit-cell corrugated sandwich structures

Figures 3.5-3.8 show the maximum core compressions for the unit-cell corrugated sandwich structures with BBBB, AACC, ABBC and gradually graded core arrangements subjected to initial velocities 10m/s, 20m/s, 30m/s, 40m/s and 50m/s.

Under the initial velocity 10m/s, the crushing for C layers or thinner layer is observed in AACC, ABBC and gradually graded corrugated core arrangements and the AACC arrangement has the largest core compression. The BBBB arrangement mainly behaves an elastic response under initial velocity 10m/s and has the smallest core compression.

For BBBB arrangement shown in Figure 3.5, the front (facing the blast loading) two B layers crush under initial velocity 20m/s. When the initial velocity increased to above 30m/s, all the corrugated B layers get crushed. When the initial velocity is larger than 40m/s, the core section of BBBB reaches high densification status. Based on observation, when the core compression is larger than 20mm, the core can be considered as high densification status.

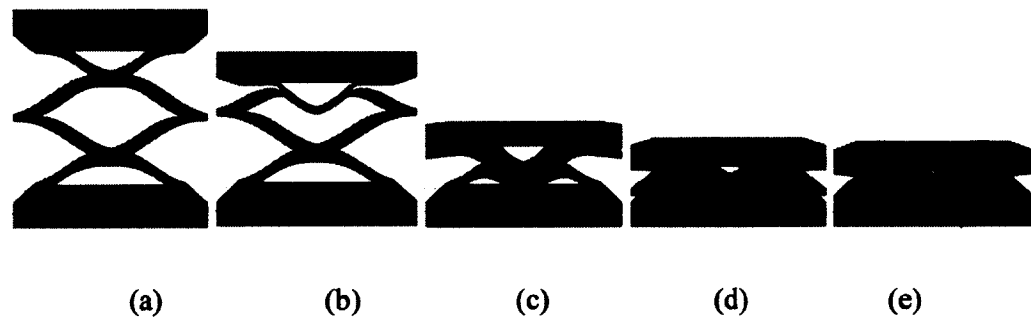


Figure 3.5 Maximum core compression of corrugated BBBB arrangement under initial velocity: (a) 10m/s (b) 20m/s (c) 30m/s (d) 40m/s and (e) 50m/s

Figure 3.6 shows the deformed shapes for AACC corrugated core arrangement subjected to different initial velocities. The A layers start to crush when the initial

velocity is 30m/s. When the initial velocity is larger than 40m/s, the core section gets fully crushed.

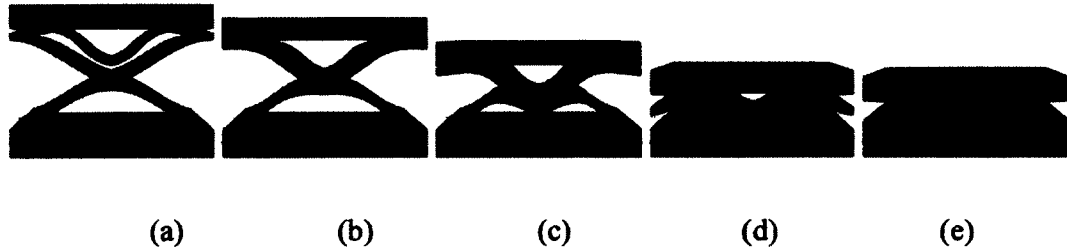


Figure 3.6 Maximum core compression of corrugated AACC arrangement under initial velocity: (a) 10m/s (b) 20m/s (c) 30m/s (d) 40m/s and (e) 50m/s

Figure 3.7 shows the deformed shapes for ABBC corrugated core arrangement subjected to different initial velocities. C layer starts to crush under initial velocity 10m/s. Under initial velocity 20m/s, the B layer which is further from the blast buckles. All the corrugated layers get crushed under initial velocity 40m/s and the ABBC arrangement reaches a high densification status.



Figure 3.7 Maximum core compression of corrugated ABBC arrangement under initial velocity: (a) 10m/s (b) 20m/s (c) 30m/s (d) 40m/s and (e) 50m/s

Figure 3.8 shows the deformed shapes for gradually graded corrugated core arrangement subjected to different initial velocities. This model gets crushed layer by layer from front substrate to back substrate. The back layer gets crushed until initial velocity 50m/s and the sandwich structure reaches high densification.

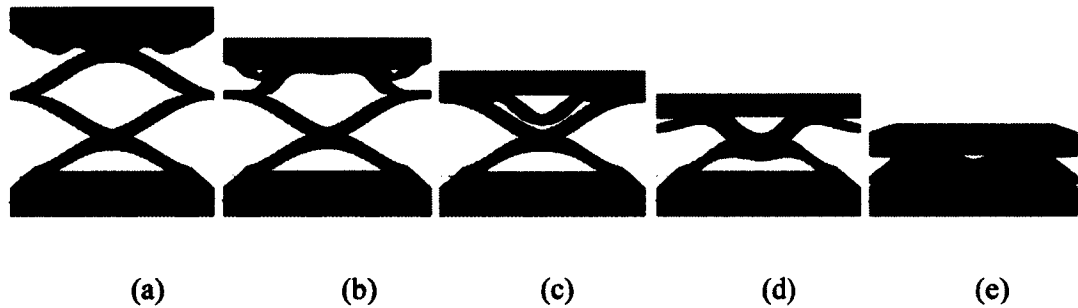


Figure 3.8 Maximum core compression of corrugated gradually graded core arrangement under initial velocity: (a) 10m/s (b) 20m/s (c) 30m/s (d) 40m/s and (e) 50m/s

The maximum core compressions under different initial velocities for the four corrugated core arrangements are summarized in Figure 3.9. We can see that the sandwich structure with gradually graded corrugated core gets high densification under a larger initial velocity, which indicates a larger impact tolerance than the others. Similar trend is found for ABBC arrangement, but not as obvious as that for gradually graded corrugated core arrangement. AACC has the largest core compression under the small initial velocities 10m/s and 20m/s.

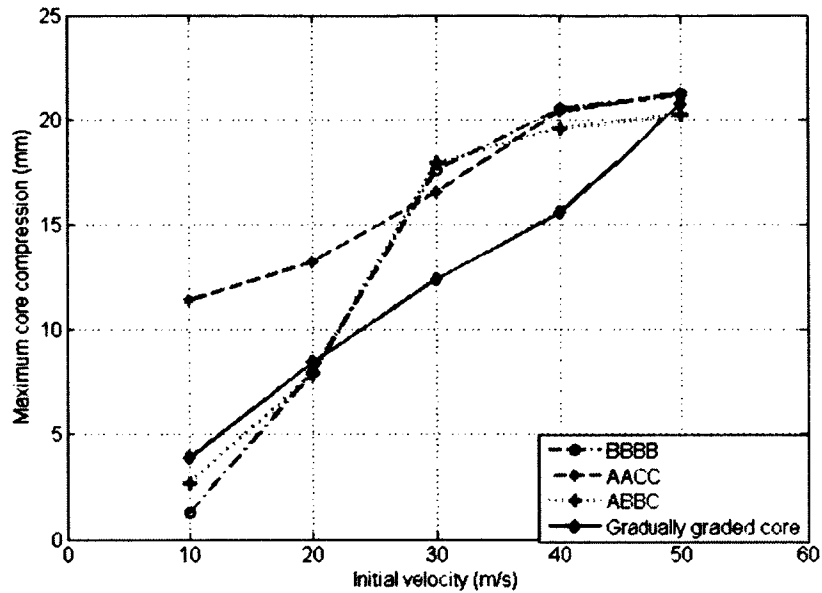


Figure 3.9 Maximum core compressions for unit-cell corrugated sandwich structures with various cores subjected to different initial velocities

3.3.3.2 Unit-cell trapezoid sandwich structures

Figures 3.10-3.13 show the maximum core compressions for the trapezoid sandwich structures with BBBB, AACC, ABBC and gradually graded core arrangements subjected to initial velocities 10m/s, 30m/s, 50m/s, 70m/s and 90m/s, respectively.

The deformed shapes for BBBB trapezoid core arrangement at its maximum core compression under different initial velocities are shown in Figure 3.10. The BBBB arrangement mainly behaves an elastic response under initial velocity 10m/s and has the smallest core compression among all the core arrangements. When increasing the initial velocity, the layers get crushed from front (facing the blast loading) to back. When the initial velocity is 90m/s, the BBBB core reaches high densification.

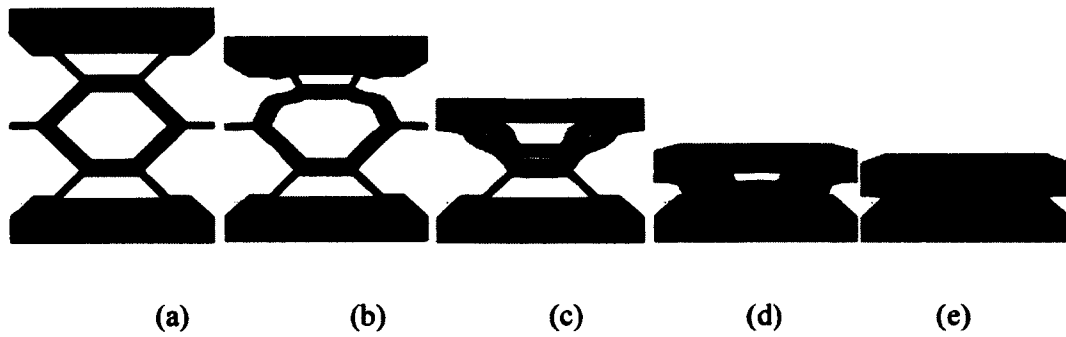


Figure 3.10 Maximum core compression of trapezoid BBBB arrangement under initial velocity: (a) 10m/s (b) 30m/s (c) 50m/s (d) 70m/s and (e) 90m/s

The deformed shapes for AACC trapezoid core arrangement at its maximum core compression under different initial velocities are shown in Figure 3.11. Subjected to initial velocity 10m/s, the front C layer is fully collapsed and the second C layer starts to crush. Under initial velocity 70m/s, all the layers get crushed. When the initial velocity is 90m/s, the core section of AACC reaches high densification status.

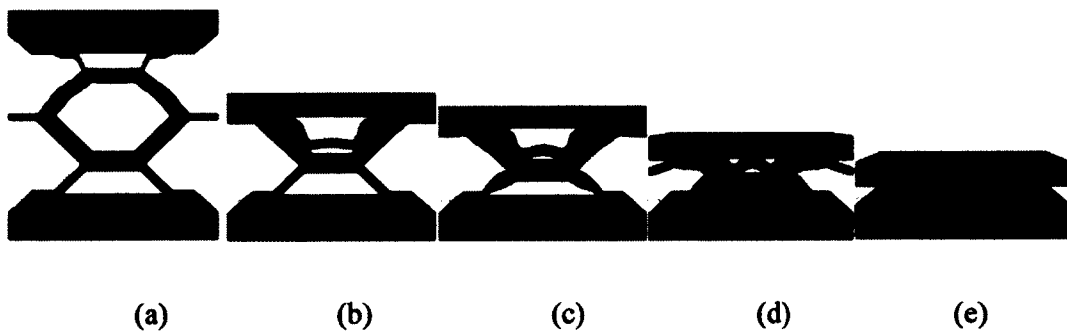


Figure 3.11 Maximum core compression of trapezoid AACC arrangement under initial velocity: (a) 10m/s (b) 30m/s (c) 50m/s (d) 70m/s and (e) 90m/s

The deformed shapes for ABBC trapezoid core arrangement at its maximum core compression under different initial velocities are shown in Figure 3.12. Under initial velocity 10m/s, only the front C layer gets crushed. With increased initial velocities, the layers get crushed from front to back. Under 90m/s initial velocity, the core doesn't reach the full densification status.

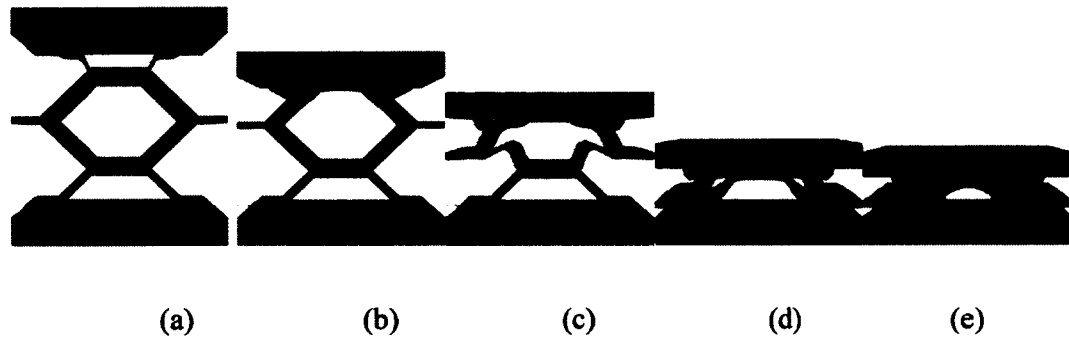


Figure 3.12 Maximum core compression of trapezoid ABBC arrangement under initial velocity: (a) 10m/s (b) 30m/s (c) 50m/s (d) 70m/s and (e) 90m/s

The deformed shapes for gradually graded trapezoid core arrangement at its maximum core compression under different initial velocities are shown in Figure 3.13. Under initial velocity 10m/s, only the front layer gets crushed. With increased initial velocities, the layers get crushed from front to back. Under 90m/s initial velocity, the core reaches its full densification.

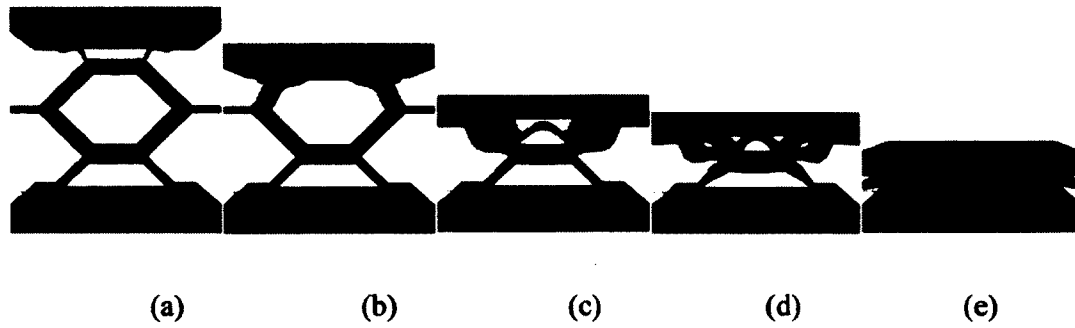


Figure 3.13 Maximum core compression of trapezoid gradually graded core arrangement under initial velocity: (a) 10m/s (b) 30m/s (c) 50m/s (d) 70m/s and (e) 90m/s

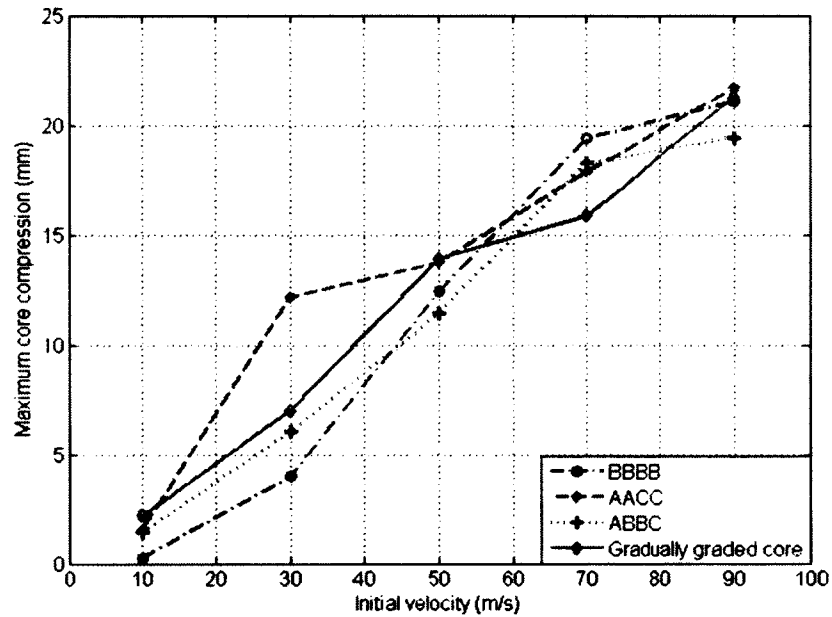


Figure 3.14 Maximum core compressions for unit-cell trapezoid sandwich structures with various cores subjected to different initial velocities

The maximum core compressions under different initial velocities for the four trapezoid core arrangements are summarized in Figure 3.14. Under low velocities 10m/s and 30m/s, BBBB has the smallest core compression. Except the ABBC

arrangement, all the models get fully crushed under initial velocity 90m/s. ABBC arrangement leads to a larger impact tolerance.

3.3.3.3 Comparison on the maximum core compressions of unit-cell corrugated and trapezoid sandwich structures

The maximum core compressions for unit-cell corrugated and trapezoid sandwich structures with various core arrangements subjected to different initial velocities are summarized in Figure 3.9 and Figure 3.14, respectively. Under the same initial velocities, such as 10m/s, 30m/s and 50m/s, the trapezoid sandwich structures have much smaller core compressions than corrugated sandwich structures. For the unit-cell corrugated sandwich structures, the BBBB, AACC and ABBC arrangements get high densification under initial velocity 40m/s, while the gradually graded core gets high densification under initial velocity 50m/s. For the unit-cell trapezoid sandwich structures, all the arrangements except ABBC get high densification under initial velocity 90m/s. Overall the trapezoid sandwich structures have larger loading tolerance. And the graded cores, gradually graded core among corrugated sandwich structures and ABBC core among trapezoid sandwich structures have larger loading tolerance.

3.3.4 Maximum compressive reaction force at the back face under different initial velocities

The maximum compressive reaction forces at the back face of the unit-cell corrugated sandwich structures with various cores under different initial velocities are summarized and compared in Figure 3.15. We can see that under low initial velocities 10m/s, 20m/s and 30m/s, the maximum compressive reaction forces are small and

don't increase much as the initial velocity increases. Under initial velocity 40m/s, the BBBB, AACC and ABBC reach high densification and the maximum compressive reaction forces for these arrangements get increased greatly. Under initial velocity 50m/s, the gradually graded core gets high densification and its maximum reaction force is increased by a large amount. We can see that when the sandwich structures get fully crushed, the corrugated sandwich structures transmit much larger compressive force to the support. When the sandwich structures get highly crushed, the AACC has the largest maximum compressive reaction force at the back face, and the ABBC and the gradually graded corrugated core have smaller maximum compressive reaction force at the back face.

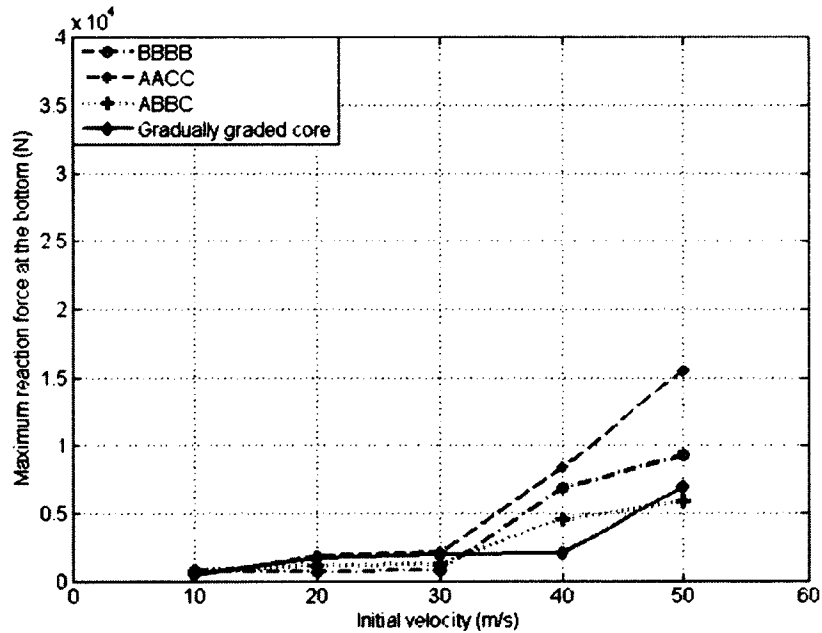


Figure 3.15 Maximum reaction force at the back face of unit-cell corrugated sandwich structures with various cores subjected to different initial velocities

The maximum compressive reaction forces at the back face of the unit-cell trapezoid sandwich structures with various cores under different initial velocities are summarized and compared in Figure 3.16. We can see that under initial velocities 10m/s, 30m/s, 50m/s and 70m/s, the maximum compressive reaction forces are small and don't increase much with the initial velocity increase. Under initial velocity 90m/s, the BBBB and AACC arrangements reach high densification and the maximum reaction force for these arrangements get increased greatly. The gradually graded core arrangement has a relatively smaller maximum compressive reaction force than BBBB and AACC, even after the gradually graded core gets fully crushed. Since the ABBC arrangement doesn't get fully crushed under 90m/s, the maximum compressive reaction force is the smallest. Similar to the results for unit-cell corrugated sandwich structures, when the unit-cell trapezoid sandwich structures get highly crushed, the AACC has the largest maximum compressive reaction force at the back face.

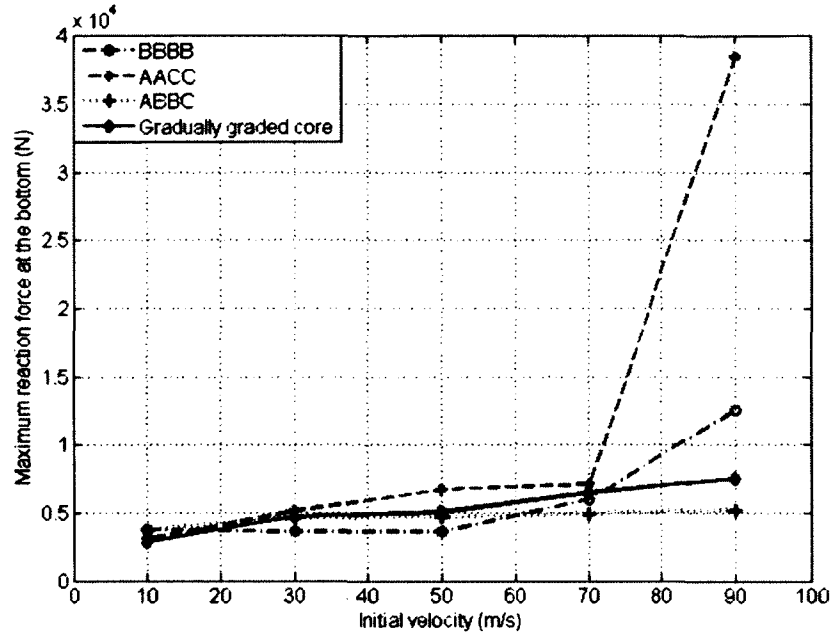


Figure 3.16 Maximum reaction force at the back face of unit-cell trapezoid sandwich structures with various cores subjected to different initial velocities

We also notice that under the same initial velocities 10m/s and 30m/s before the sandwich structures get fully crushed, the unit-cell trapezoid sandwich structures lead to larger compressive reaction force at their back faces. For both unit-cell corrugated and trapezoid sandwich structures, the maximum compressive reaction forces increase largely when the cores get highly crushed. So in order to protect the support, we should design the sandwich structures to avoid their high densification.

3.3.5 Energy plots

During the crushing progress, almost all the initial kinetic energy is transferred to plastic energy and the rest small amount of energy includes the kinetic energy, elastic strain energy and dissipated energy by damping. In the sandwich structures, the

plastic energy is all absorbed by the corrugated and trapezoid layers in the core section.

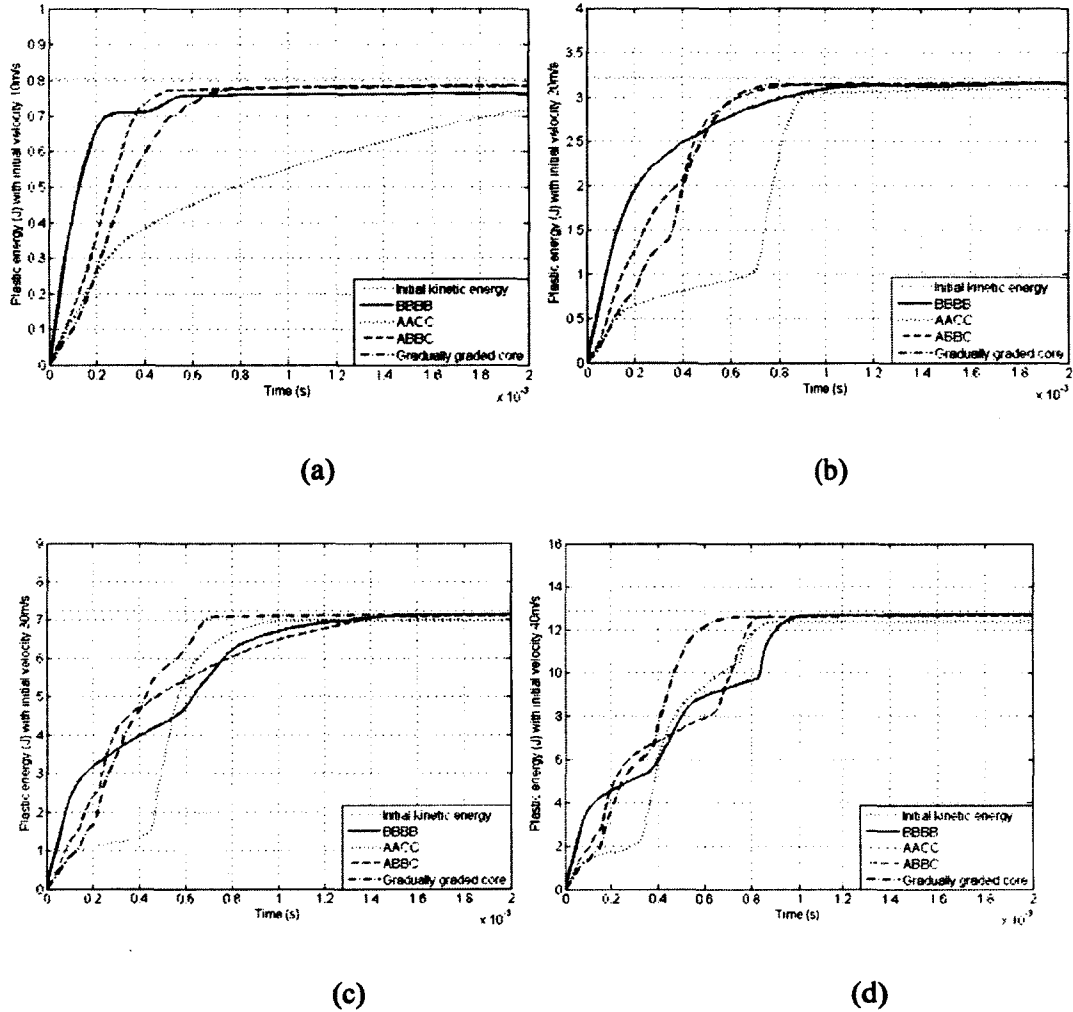


Figure 3.17 Plastic energy histories for unit-cell corrugated sandwich structures with various cores under initial velocity: (a) 10m/s (b) 20m/s (c) 30m/s and (d) 40m/s

The plastic energy time histories for unit-cell corrugated sandwich structures with various core arrangements under different initial velocities are plotted in Figure 3.17. Under initial velocities 10m/s, 20m/s, 30m/s and 40m/s, the initial kinetic energies are 0.805J, 3.22J, 7.245J and 12.88J, respectively. Under low initial velocity 10m/s and

20m/s, the AACC corrugated arrangement takes a longer time to absorb the plastic energy and reach the stable status, while ABBC and gradually graded corrugated core arrangements reach the stable status very fast. Under 30m/s and 40m/s, the gradually graded core absorbs the plastic energy faster than the others and its core compression is the smallest core compression (as shown in Figure 3.9).

The plastic energy time histories for unit-cell trapezoid sandwich structures with various cores under different initial velocities are plotted in Figure 3.18. Under initial velocities 10m/s, 30m/s, 50m/s and 70m/s (smaller than the required initial velocity for high densification), the initial kinetic energies are 0.805J, 7.245J, 20.125J and 39.445J, respectively.

Under initial velocity 10m/s, the BBBB arrangement still has large amount of remaining kinetic energy. ABBC and AACC arrangements have the similar plastic energy time history under 10m/s initial velocity. And the gradually graded core takes more time to absorb the plastic energy.

As the initial velocity increases, the BBBB arrangement takes longer time to absorb the plastic energy.

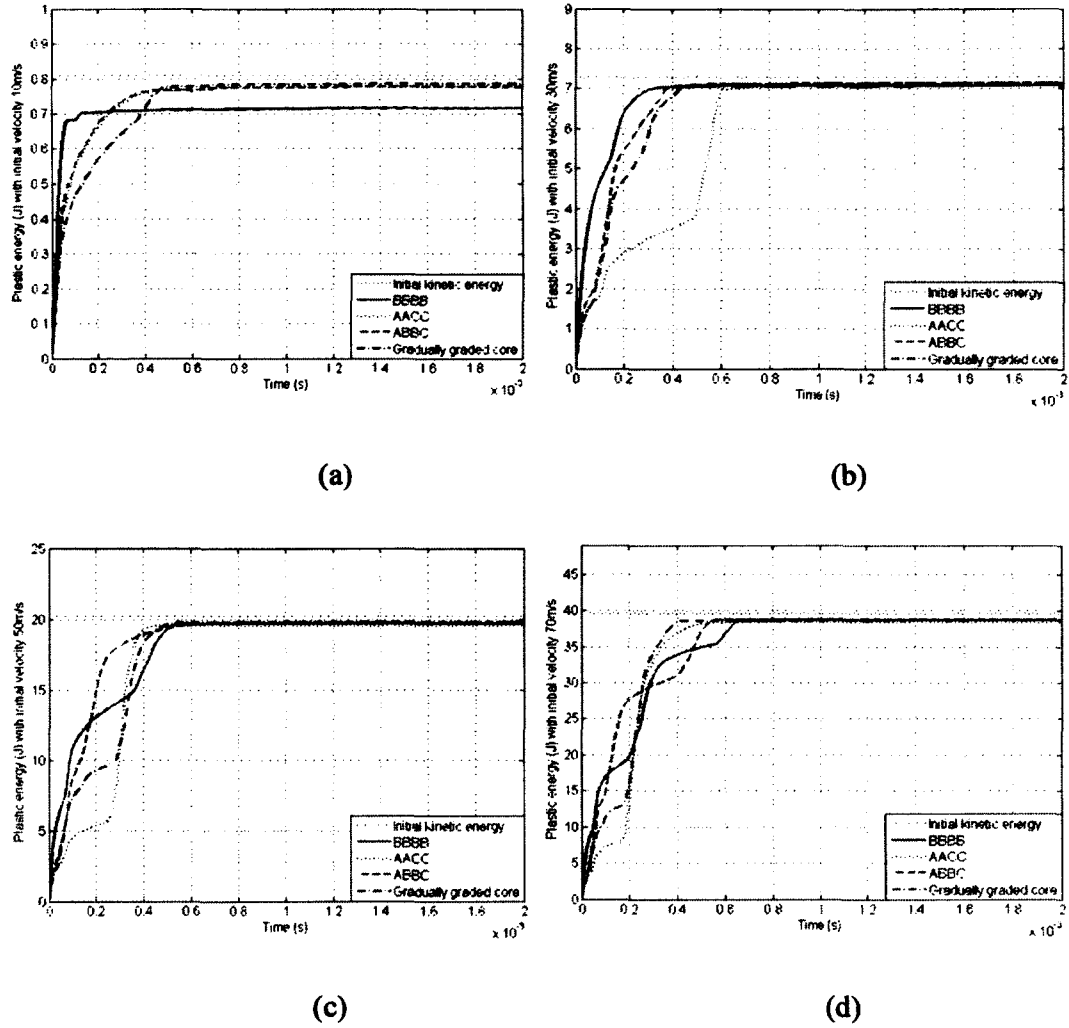


Figure 3.18 Plastic energy histories for unit-cell trapezoid sandwich structures with various cores under initial velocity: (a) 10m/s (b) 30m/s (c) 50m/s and (d) 70m/s

From the Figure 3.17 and Figure 3.18, we can see that under the same initial velocities 10m/s and 30m/s, the unit-cell trapezoid sandwich structures take shorter time to absorb the plastic energy than unit-cell corrugated sandwich structures.

3.3.6 Strain rate dependence

In this section, the core is considered to be made of homogeneous material with a relative density calculated by the volume of the layers divided by the volume of the core. So, the averaged compressive strain rate for the core can be found as dividing the average velocity of the front substrate by the height of the core. And the average velocity of the front substrate is calculated as dividing the maximum core compression by the time to reach the maximum core compression.

The plastic energies w.r.t the compressive strain in the core under different initial velocities 20m/s, 30m/s, 40m/s and 50m/s for corrugated BBBB arrangement are plotted in Figure 3.19. Here, we consider the core section is made of a homogeneous material with a relative density 0.08 to steel. The height of the core is 26mm for the corrugated BBBB arrangement. Under the initial velocities 20m/s, 30m/s, 40m/s and 50m/s, the corresponding compressive strain rates are 264.62/s, 419.62/s, 864.23/s and 1116.49/s, respectively.

At the same compressive strain, the BBBB arrangement under higher strain rate absorbs larger amount of plastic energy, which indicate that the stress is higher in the material under higher strain rate. Or when the BBBB arrangements absorb the same amount of plastic energy, the compressive strain is smaller under higher strain rate. All these indicate that with the strain-rate dependent material property, the resistance of the corrugated sandwich structure is larger under higher strain rate.

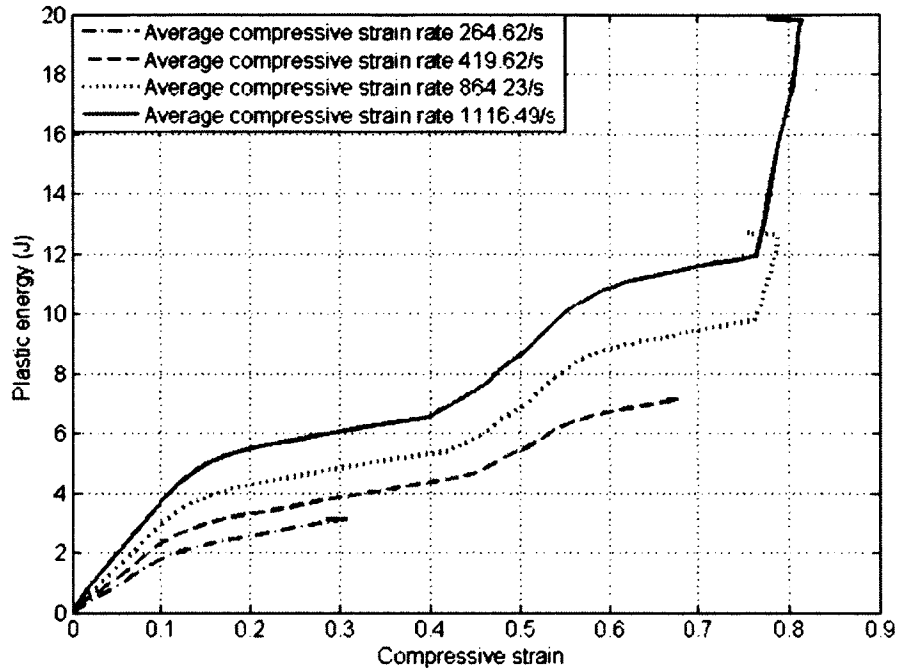


Figure 3.19 Plastic energy w.r.t compressive strain for unit-cell corrugated BBBB sandwich structures under average compressive strain rate: (a) 264.62/s (b) 419.62/s (c) 864.23/s and (e) 1116.49/s

The plastic energies w.r.t the compressive strain in the core under different initial velocities 30m/s, 50m/s, 70m/s and 90m/s for trapezoid BBBB arrangement are plotted in Figure 3.20. Similarly, we consider the core section made of a homogeneous material with a relative density 0.08 to steel, which is also the proportion of volume for B layer to the volume of the core. Then, following the same method, under the initial velocities 30m/s, 50m/s, 70m/s and 90m/s, the corresponding compressive strain rates in the cores of trapezoid BBBB arrangements are 444.95/s, 863.44/s, 1114.89/s and 1824.16/s, respectively.

Similar results are found for trapezoid sandwich structures and corrugated sandwich structures. The strain rate dependence leads to larger resistance of the trapezoid sandwich structures under higher strain rate.

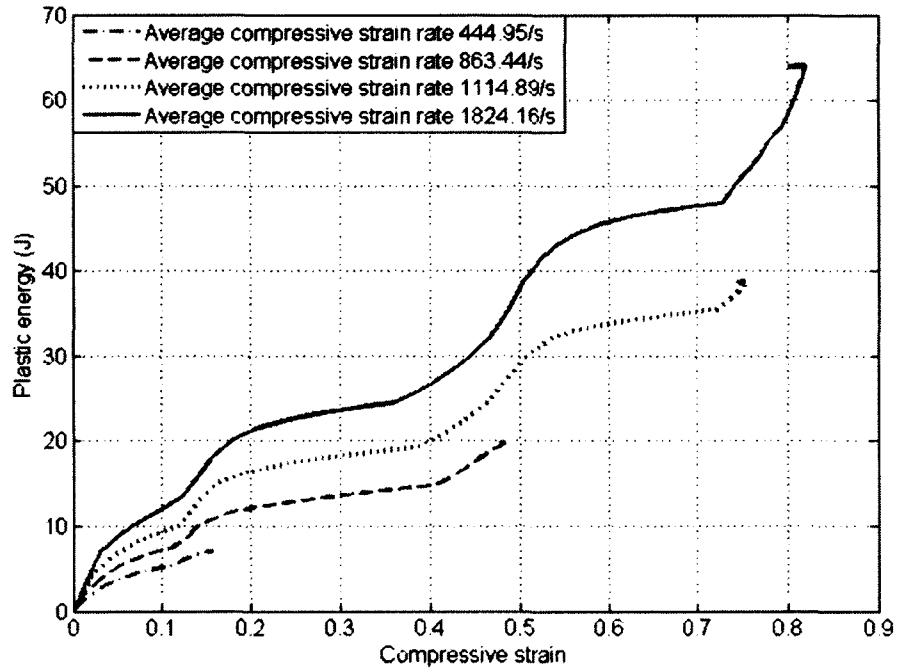


Figure 3.20 Plastic energy w.r.t compressive strain for unit-cell trapezoid BBBB sandwich structures under average compressive strain rate: (a) 444.95/s (b) 863.44/s (c) 1114.89/s and (d) 1824.16/s

3.4 Effects of geometric imperfections

Geometric imperfections introduced during the manufacture of these layers and the stacking of the sandwich structures can promote the buckling or crushing of these layers and reduce the load capacity of the structures. Since the shape of the imperfections can't be known precisely, several imperfection modes should be considered. It is important to include imperfection shapes with relatively short

wavelengths that promote localized buckling since such modes are observed under high velocity impact [60]. The imperfection shapes can be found by conducting quasi-static buckling eigenvalue analysis in ABAQUS/standard on the perfect structures. The mode shapes obtained from the buckling analysis can be saved in a file. If the same mesh is used for both buckling analysis and explicit dynamic analysis, the geometric imperfections are introduced to dynamic analysis by selecting a scale factor for certain mode.

3.4.1 Geometric imperfection shapes obtained from buckling analysis

This section talks about the geometric imperfection shapes for unit-cell corrugated and trapezoid sandwich structures with BBBB core arrangement obtained from the quasi-static buckling analysis in ABAQUS/Standard solver. The finite element models used for buckling analysis were fixed at the back substrate and subjected to uniformly distributed pressure loading on the front substrate. Besides, the mesh for the buckling analysis was the same as that used for explicit dynamic analysis, which was discussed in section 3.3.2.

3.4.1.1 Geometric imperfection shapes for unit-cell corrugated sandwich structure with BBBB core arrangement

The geometric imperfection shapes for corrugated BBBB arrangement obtained from quasi-static buckling analysis are shown in Figure 3.21. The Mode I and II are the lowest successive modes. The out-of-plane torsional mode is skipped, since it rarely happens in the manufacture process comparing to the Mode III. The amplitudes for the imperfections are exaggerated in Figure 3.21. In the dynamic analysis, scale factors will be chosen to set desired amplitude of the geometric imperfections.

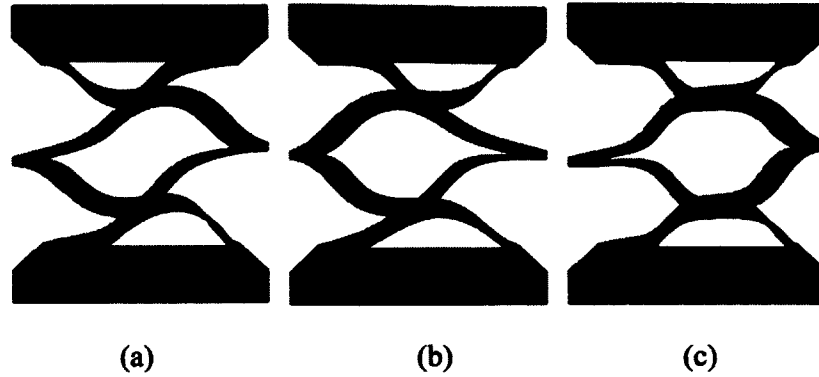


Figure 3.21 Imperfection shapes for unit-cell corrugated sandwich structure with BBBB core arrangement obtained from buckling analysis: (a) Mode I (b) Mode II and (c) Mode III

3.4.1.2 Geometric imperfection shapes for unit-cell trapezoid sandwich structure with BBBB core arrangement

The imperfection shapes for trapezoid BBBB arrangement obtained from quasi-static buckling analysis are shown in Figure 3.22. Similarly, the out-of-plane torsional mode is skipped.

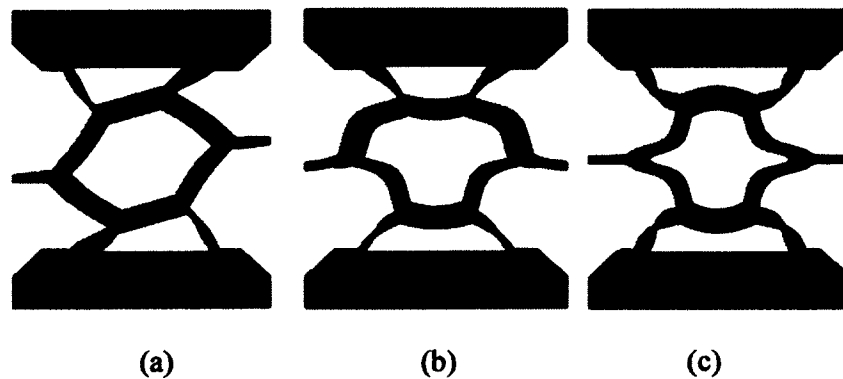


Figure 3.22 Imperfection shapes for unit-cell trapezoid sandwich structure with BBBB core arrangement obtained from buckling analysis: (a) Mode I (b) Mode II and (c) Mode III

3.4.2 Comparison on the geometric imperfection sensitivity of corrugated and trapezoid sandwich structures

In this part, the unit-cell corrugated and trapezoid sandwich structures with geometric imperfections subjected to different level of initial velocity are analyzed in ABAQUS/Explicit. The imperfection shapes for corrugated BBBB arrangement introduced to dynamic analysis are shown in Figure 3.23. The maximum imperfection deflections for the all the imperfection modes are kept as 0.5mm in this section.

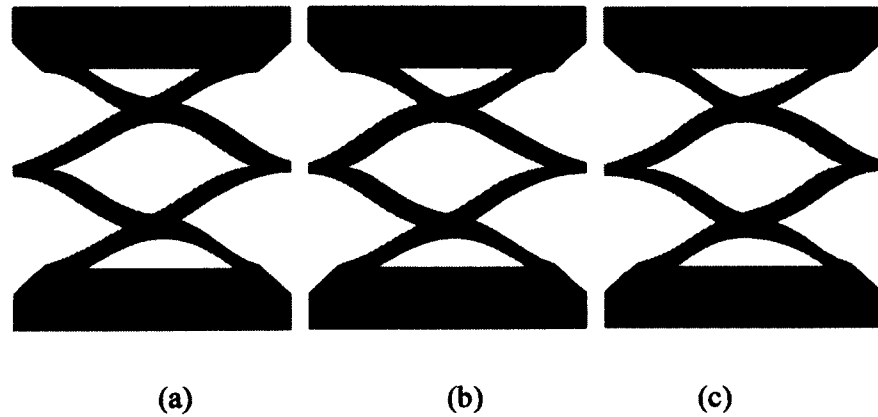


Figure 3.23 Imperfection shapes for unit-cell corrugated sandwich structure with BBBB core arrangement introduced to dynamic analysis: (a) Mode I (b) Mode II and (c) Mode III

The imperfection shapes for trapezoid BBBB arrangement introduced to dynamic analysis are shown in Figure 3.24. The maximum imperfection deflections for the all the three imperfection modes are also kept as 0.5mm.

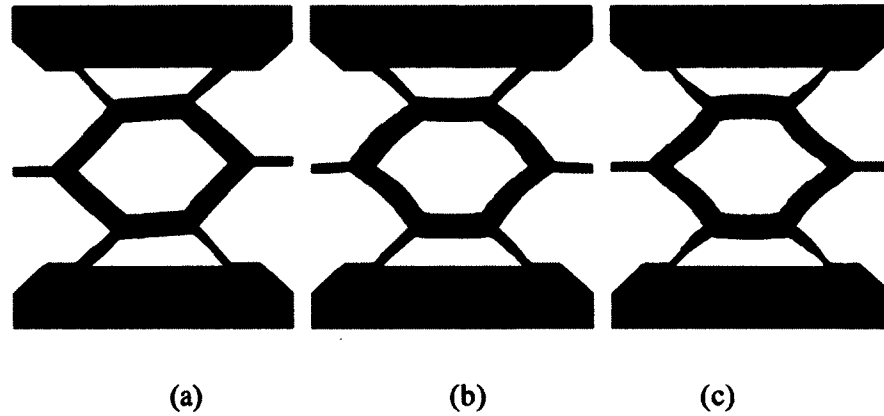


Figure 3.24 Imperfection shapes for unit-cell trapezoid sandwich structure with BBBB core arrangement introduced to dynamic analysis: (a) Mode I (b) Mode II and (c) Mode III

The maximum core compressions under different initial velocities for the corrugated BBBB core arrangement with three imperfection modes are summarized and compared with these for perfect corrugated BBBB arrangement in Figure 3.25. With Mode I imperfection, the maximum core compressions are larger than that without geometric imperfection. With Mode II imperfection, the maximum core compressions are larger than these without geometric imperfection under initial velocities 10m/s and 20m/s. Under initial velocities 30m/s and 40m/s, the effect of Mode II imperfection is not obvious and the difference in the maximum core compression is close to zero. With Mode III imperfection, the maximum core compressions are larger than these without imperfection under low initial velocities 10m/s and 20m/s, while the maximum core compressions are smaller than these without imperfection under high initial velocity 30m/s.

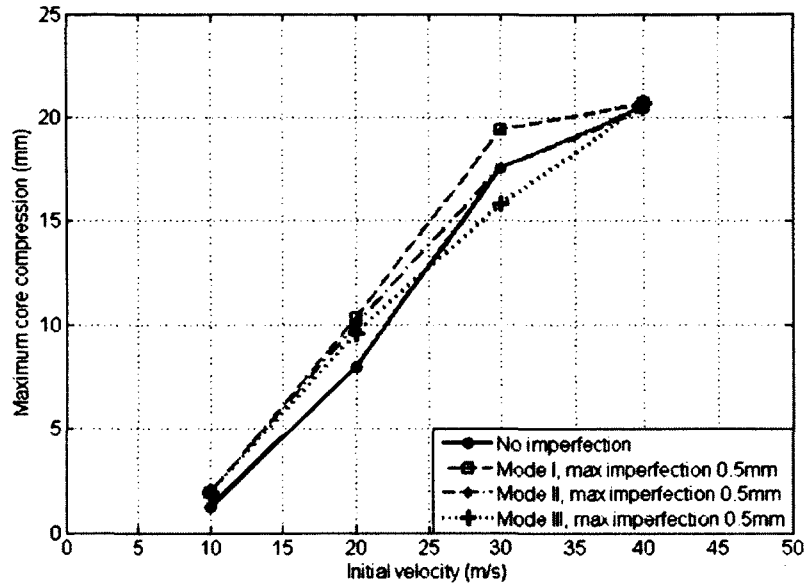


Figure 3.25 Maximum core compressions for unit-cell corrugated sandwich structure with BBBB core arrangement with and without geometric imperfection subjected to different initial velocities

The maximum core compressions under different initial velocities for the trapezoid BBBB core arrangement with three imperfection modes are summarized and compared with these for perfect trapezoid BBBB arrangement in Figure 3.26. With Mode I, II and III imperfections, the maximum core compression are much larger than that without geometric imperfection.

By comparing Figure 3.25 and Figure 3.26, we find that the trapezoid sandwich structure is more sensitive to the geometric imperfections than corrugated sandwich structure.

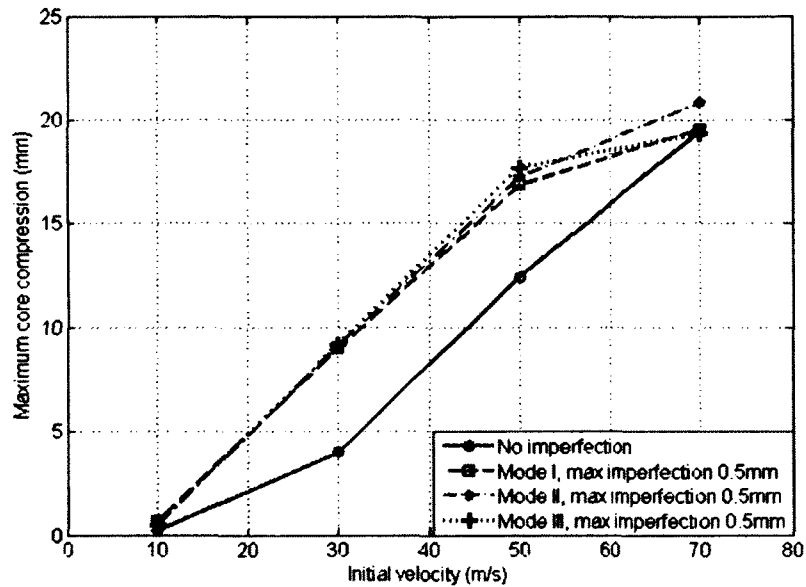


Figure 3.26 Maximum core compressions for unit-cell trapezoid sandwich structure with BBBB core arrangement with and without geometric imperfection subjected to different initial velocities

3.4.3 Effects of geometric imperfections on the dynamic response of unit-cell sandwich structures with trapezoid BBBB core arrangement

Since the sandwich structure with trapezoid BBBB core arrangement is very sensitive to the geometric imperfection, the effect of different level of geometric imperfections is also investigated in this work. The maximum geometric imperfections 0.1mm, 0.3mm and 0.5mm for the three modes are considered in this section.

Figure 3.27 shows the maximum core compressions for trapezoid BBBB core arrangement with Mode I imperfections. As expected, larger imperfection leads to larger difference between the structures with and without geometric imperfections. Under low initial velocity 10m/s, the Mode I geometric imperfection doesn't lead to much difference. As the initial velocity increases, the trapezoid BBBB core

arrangement with the maximum imperfection as 0.1mm leads to a little larger core compression, but much small than these with imperfections as 0.3mm and 0.5mm.

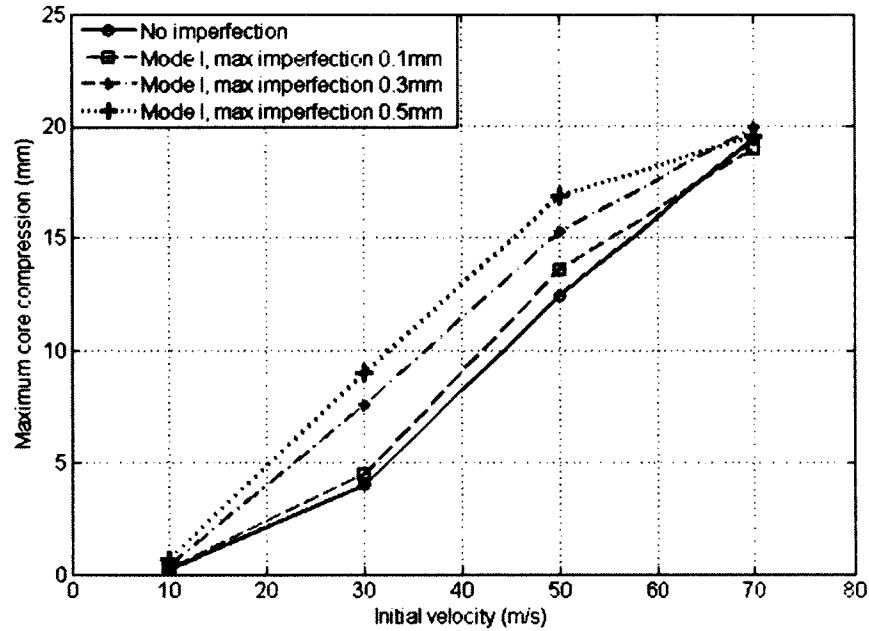


Figure 3.27 Maximum core compressions for trapezoid BBBB core arrangement with Mode I imperfections subjected to different initial velocities

Figure 3.28 shows the maximum core compressions for trapezoid BBBB core arrangement with Mode II imperfection. For the Mode II imperfection mode, we can see that with increasing imperfection values, the difference between structures with and without imperfections gets increased almost linearly.

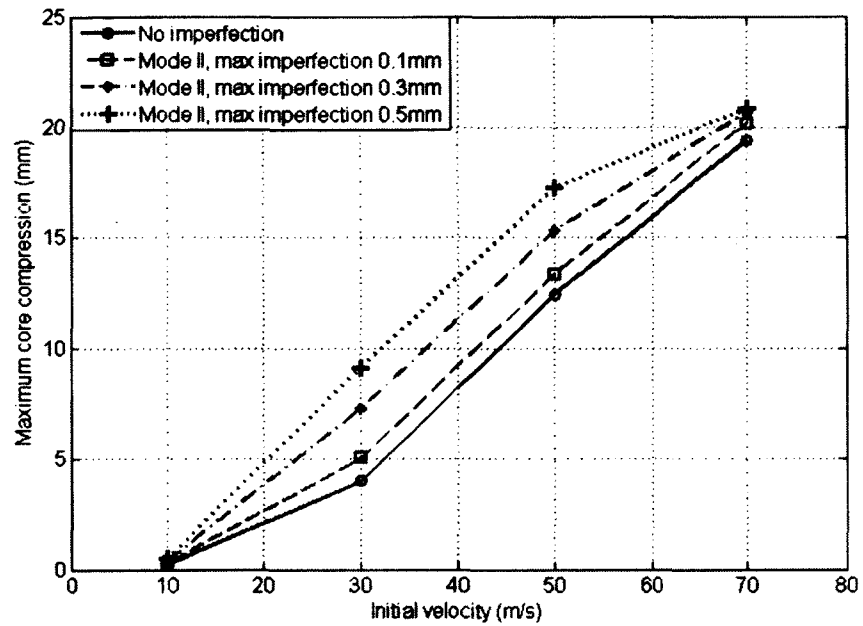


Figure 3.28 Maximum core compressions for trapezoid BBBB core arrangement with Mode II imperfections subjected to different initial velocities

Figure 3.29 shows the maximum core compressions for trapezoid BBBB core arrangement with Mode III imperfection. The trapezoid BBBB core arrangement with Mode III imperfection as 0.1mm doesn't lead to much difference, especially under low initial velocities. And the Mode III imperfections with maximum deflections as 0.3mm and 0.5mm lead to the similar results.

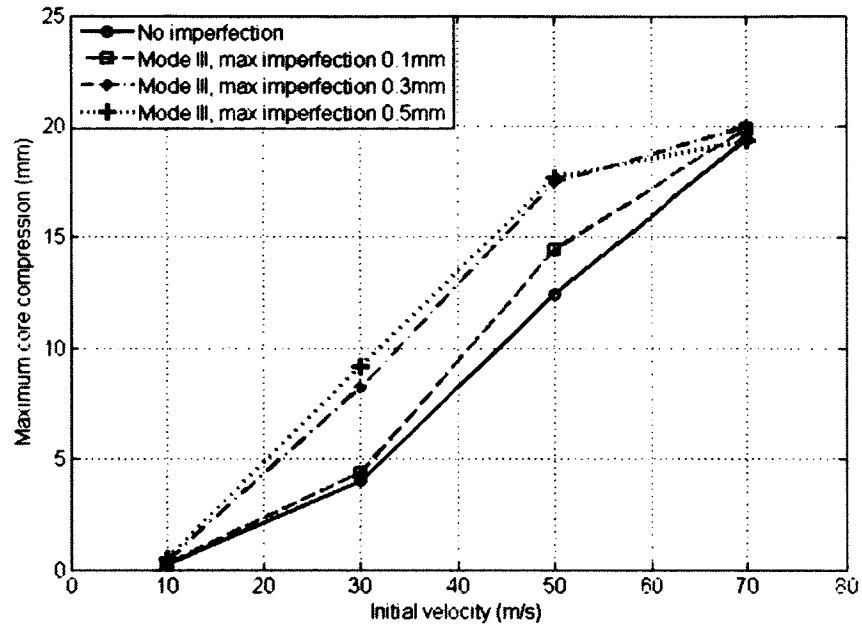


Figure 3.29 Maximum core compressions for trapezoid BBBB core arrangement with Mode III imperfections subjected to different initial velocities

3.5 Concluding remarks

In this work, the dynamic response of unit-cell corrugated and trapezoid sandwich structures with BBBB, AACC, ABBC and gradually graded core arrangements under different levels of initial velocities or impulse impact are investigated using finite element method in ABAQUS/Explicit. All the structures share the same mass. The following facts are found:

- 1) The unit-cell trapezoid sandwich structures have much smaller core compression than their corresponding unit-cell corrugated sandwich structures under the same initial velocity. The unit-cell corrugated sandwich structures get fully crushed under a smaller initial velocity than that for the unit-cell trapezoid sandwich structures.

- 2) The maximum compressive reaction forces at the back face of the sandwich structures increase greatly once the sandwich structures get high densification. Before the high densification status, the trapezoid sandwich structures lead to larger maximum compressive reaction force at the back face when subjected to the same initial velocity.
- 3) Among corrugated sandwich structures, the gradually graded core arrangement leads to larger load capacity and requires larger initial velocity to get high densification. And among trapezoid sandwich structures, the ABBC arrangement gets fully crushed under a larger initial velocity than other arrangements.
- 4) Since the sandwich structure is designed to protect the main structure it attached to, smaller maximum compressive reaction force is desired. In order to keep the compressive reaction force low, the sandwich structures shouldn't get fully crushed under design loading.
- 5) When the core section is treated as a homogeneous material, the average compressive strain rate can be calculated by dividing the average velocity by the height of the core section. From the plastic energy w.r.t the compressive strain curves, the strain-rate dependence material properties play an important role on increasing the loading tolerance of the sandwich structures under high strain rate.

Besides, the effects of geometric imperfections on the dynamic response of unit-cell corrugated and trapezoid BBBB core arrangements are discussed and compared. We found that the trapezoid sandwich structures are more sensitive to the geometric imperfections than corrugated sandwich structures.

Chapter 4 - Finite Element Procedure on the Dynamic Response of Rate-dependent Functionally Graded Steel Plates Subjected to Dynamic Air Pressure Loads

4.1 Introduction

Due to the benefit of utilizing graded core in the sandwich structures, we want to extend the stepwise graded core to a functionally graded material concept. A functionally graded material (FGM) is a material concept involving new advanced materials as well as traditional materials in which the volume fractions of the constituent materials vary smoothly resulting in graded macroproperties with a nonuniform microstructure [61, 62]. FGM can be designed for specific functions and applications. FGM has potential uses in aerospace engineering, the nuclear industry, the automotive industry, and civil infrastructure. There have been numerous articles published on the static and dynamic responses of linear-elastic FGMs. Zenkour [63] derived static displacement and stress responses of sandwich plates with a functionally graded (FG) interface layer based on shear deformation theories or classical plate theory. Qian et al. [64] analyzed the static deformations as well as the free and forced vibrations of a thick rectangular FG elastic plate using a higher-order shear and normal deformable plate theory with a meshless local Petrov-Galerkin method. Yang and Shen [65] investigated and parametrically studied the elastic dynamic response of temperature-dependent rectangular thin FG plates subjected to impulsive loads (a suddenly applied load, a step load, a triangular load, a sine load and an exponential load) with/without resting on an elastic foundation. Huang and Shen [66] investigated the vibration and dynamic response of a FG plate under

thermal environment. Considering the heat conduction and temperature-dependent material properties, the vibrations and dynamic responses were nonlinear, but the FGM still deformed within its elastic region. Reddy et al. [67-70] developed finite element models to analyze static and dynamic thermo-elastic responses of FG plates, cylinders, cylindrical shells and beams.

There has been some investigation of rate-independent elastic-plastic FGM properties. Williamson et al. [71] formulated an elastic-plastic finite element numerical model based on a modified rule of mixture which is called Tamura–Tomota–Ozawa (TTO) [72], and studied the residual stresses at the graded ceramic-metal interfaces during cooling. Giannakopoulos et al. [73] evaluated rate-independent elastic-plastic material properties for a FGM interface layer (between one ductile layer and one brittle layer) based on the TTO model and developed a subroutine in ABAQUS to investigate the cyclic thermal response of the layered composite. Gunes et al. [74] analyzed the elastic-plastic impact response of a circular FG plate under low velocities. The effective constitutive relation, density and Poisson's ratio of the ceramic-metal FGM were calculated by the TTO model and no strain-rate dependence was considered.

There is a strong need for the development of rate-dependent elastic-plastic constitutive relations for FG ductile materials. Rate-dependent elastic-plastic material models are the key to analyzing FGM subjected to medium and high rate dynamic loading. Li et al. [75, 76] investigated the influence of particle volume fraction, shape, and aspect ratio on the rate-dependent elastic-plastic behavior of a particle-reinforced metal-matrix composite at high strain rates. They used an axisymmetric unit cell model and conducted both experimental and computational investigations on the

mechanical behavior of $A359/SIC_p$ metal-matrix composite in compression under a wide range of strain rates. Based on the material model of FGM, Li et al. [77] examined the impact response of layered and graded plates with volume fractions of constituent materials varying through the thickness.

In this paper, we develop a new rate-dependent elastic-plastic FGM model based upon the constituent materials and their volume fractions. The rate-dependent elastic-plastic material properties of the constituent materials are experimentally determined and a hypothetical FGM steel plate with linear gradation is considered. The modified rule of mixture is used to calculate material properties through the local volume fractions of the constituent materials. We apply the TTO model to an FGM with two ductile constituent materials. Based on the rate-dependent elastic-plastic FGM model, an ABAQUS/VUMAT subroutine is developed and implemented to simulate the dynamic response of a rectangular FG plate under dynamic air pressure load generated by a shock tube. Experimental work was carried out to provide partial validation data for the response of a monolithic plate (Steel 1018) subjected to the dynamic air pressure loads. Finite element simulations are in a good agreement with experimental data for the monolithic plate.

This chapter is organized as follows. Section 4.2 presents rate-dependent material models for FGM and numerical implementations in ABAQUS. Section 4.3 shows the shock tube testing results for the monolithic steel 1018 plate. Section 4.4 details the finite element modeling for a monolithic plate and the FGM plate subjected to dynamic air pressure loads. Section 4.5 discusses the finite element simulation results. Section 4.6 concludes this chapter.

4.2 Strain-rate dependent models for FGM and numerical implementations

4.2.1 Strain-rate dependent material model

Rate-dependent material models for the constituent materials are developed herein.

Without considering temperature effect, the flow stress of a material σ is dependent on the equivalent plastic strain ε^{pl} and the equivalent plastic strain rate $\dot{\varepsilon}^{pl}$,

$$\sigma = \sigma(\varepsilon^{pl}, \dot{\varepsilon}^{pl}) \quad (4.1)$$

In commonly used rate-dependent plastic material models, such as Johnson-Cook model and Cowper-Symonds model, the strain-rate dependence is treated separately from the quasi-static stress-strain relation,

$$\sigma = \sigma_{qs}(\varepsilon^{pl})R(\dot{\varepsilon}^{pl}) \quad (4.2)$$

where $\sigma_{qs}(\varepsilon^{pl})$ shows the quasi-static flow stress which is a function of equivalent plastic strain ε^{pl} , and $R(\dot{\varepsilon}^{pl})$ is the strain-rate dependence which is a function of the equivalent plastic strain rate $\dot{\varepsilon}^{pl}$. There are three models available in ABAQUS/CAE to define strain-rate dependence [52], i.e. yield ratio model, Johnson-Cook strain-rate dependence [78] and Power-law strain-rate dependence [79]. Figure 4.1 shows general behavior of the Johnson-Cook, Power-law and linear strain-rate dependent models when they share the same domains of strain rate and strain-rate dependence.

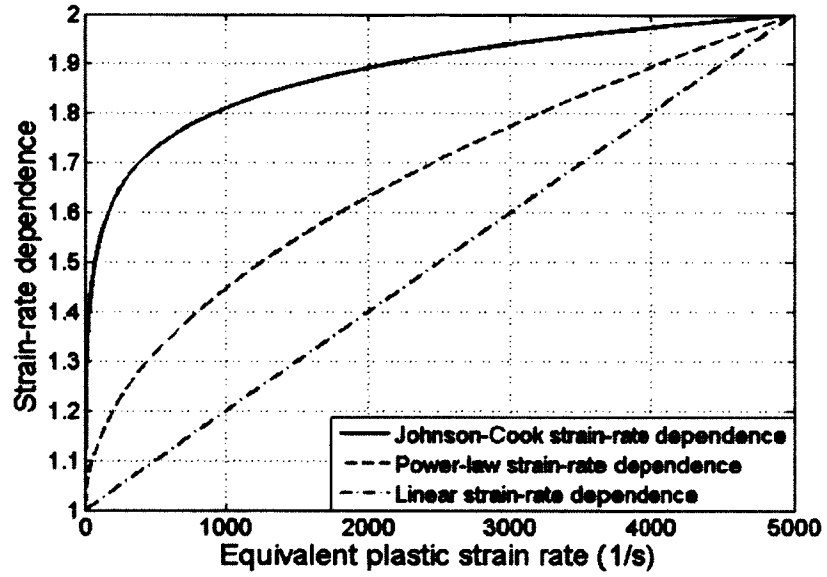


Figure 4.1 Comparison on strain-rate dependent models

In this paper, linear strain-rate dependence is selected due to the nature of experimental data of Steel 1018 (See Figure 4.2). The linear strain-rate dependence is defined as:

$$R = 1 + C \dot{\epsilon}^{pl} \quad (4.3)$$

where C is a constant representing a linear strain-rate dependence. A bilinear hardening model is widely used in representing the hardening curve due to its descriptive mathematical form. With the linear strain-rate dependence considered, the rate-dependent bilinear hardening model is given by

$$\sigma = (\sigma_y + E_p \epsilon^{pl}) (1 + C \dot{\epsilon}^{pl}) \quad (4.4)$$

where σ_y is the quasi-static yield stress, E_t is the tangent modulus, ε^{pl} refers to the equivalent plastic strain, $\dot{\varepsilon}^{pl}$ refers to the equivalent plastic strain rate and C is the strain-rate dependence factor.

4.2.2 Split-Hopkinson pressure bar tests

The Split-Hopkinson Pressure Bar (SHPB) Technique is used in this work to obtain the constitutive relations of steel 1018 for various high strain rates at room temperature. This methodology is popular for this type of test due to its ease of use and ability to decouple inertia from strain rate effects [54, 55]. Based upon the one-dimension wave propagation theory, the stress-strain curves for different strain rates can be obtained. The stress-strain curves of steel 1018 under strain rates (2000/s, 2500/s and 3100/s) obtained from SHPB tests (See Figure 4.2). In addition, the quasi-static stress-strain curve is obtained at a rate of 10^{-3} /s in compression (See Figure 4.2). The strain was determined directly from the instrument, i.e., from the displacement of the cross-head. For the elastic region we use well-known material properties such as Young's modulus=200GPa, Poisson's ratio=0.3. The rate-dependent elastic-plastic material model of steel 1018 is obtained by the curve-fitting method using the experimental data and Eq. (4.4) as shown in Figure 4.2.

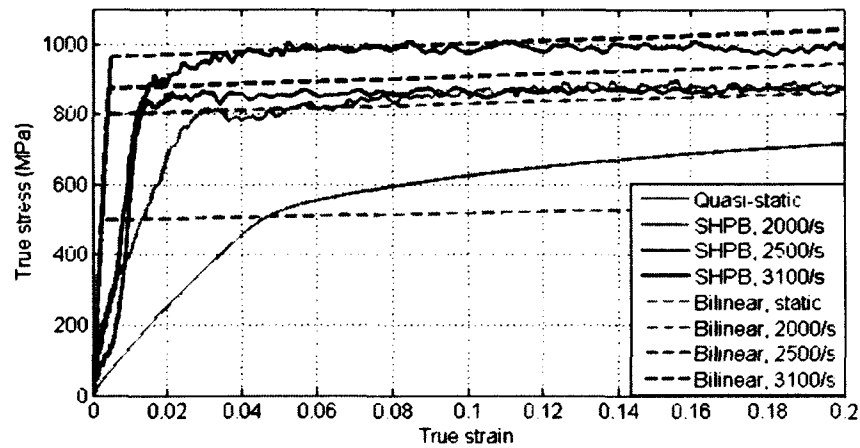


Figure 4.2 Stress-strain curves of steel 1018 at different strain rates

4.2.3 Hypothetic functionally graded plate

The FG ductile plate is assumed to be made of constituent materials steel 1018 and steel A36. The stress-strain curves of steel A36 at different strain rates are shown in Figure 4.3. The material property of steel A36 is obtained from MatWeb website [80]. Steel A36 and steel 1018 are all low-carbon steel and steel A36 is assumed to share similar strain-hardening behavior and strain-rate dependence. The FGM considered here has steel A36 as the front (facing the loading) plate, which is more compliant and can absorb more energy by its greater deformation, and steel 1018 as the back plate which has a larger yield stress. The Young's moduli of these two materials are 200GPa.

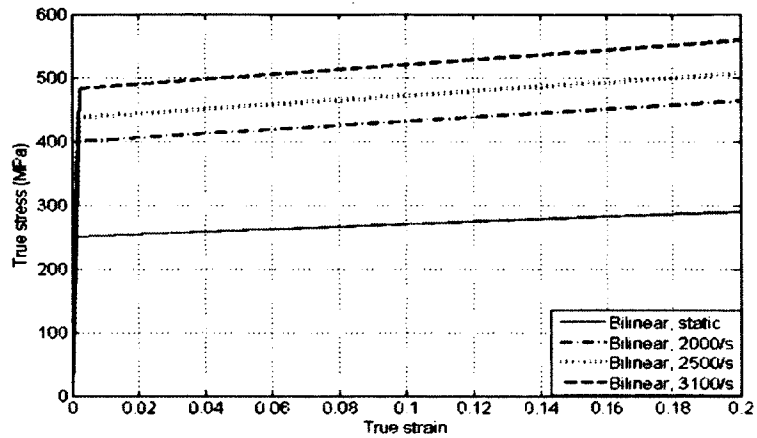


Figure 4.3 Stress-strain curves of steel A36 at different strain rates [80]

Linear gradation between the front and back faces is assumed as shown in Figure 4.4. The linear gradation is obtained by changing the volume fractions of the constituent materials linearly along the thickness direction

$$V_1 = 1 - \frac{1}{h}z, V_2 = \frac{1}{h}z \quad (4.5)$$

where V_1 is the volume fraction of steel 1018, V_2 is the volume fraction of steel A36, h is the thickness of the specimen, and z is the coordinate in the thickness direction.

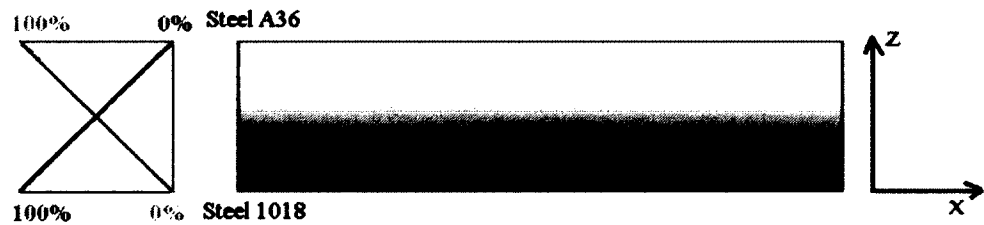


Figure 4.4 A schematic plot of linearly graded FG steel plate

4.2.4 Rate-dependent FGM model

The rate-dependent FGM model is derived based on the modified rule of mixture. Besides, isoparametric graded element concept is used to calculate the material properties at the Gauss points. In isoparametric graded finite elements [81], material properties can be interpolated from the nodal properties of the graded element using isoparametric shape functions. Material properties are the Young's modulus (E), the tangent modulus (E_t), the mass density (ρ), etc.,

$$P = \sum_{i=1}^N N_i P_i \quad (4.6)$$

In this paper, the quasi-static elastic-plastic material parameters for FGM at each Gauss point are computed using a modified rule of mixture. The modified rule of mixture is also called the TTO model, which was first proposed by Tamura *et al* [72]. The TTO model relates the uniaxial stress and strain of a two-phase composite to the corresponding uniaxial stresses and strains of two constituent materials by

$$\sigma_c = V_1 \sigma_1 + V_2 \sigma_2, \varepsilon_c = V_1 \varepsilon_1 + V_2 \varepsilon_2 \quad (4.7)$$

where σ_i , ε_i and V_i ($i=1,2$) denote the average stresses, average strains and volume fractions of the constituent phases, respectively, and σ_c and ε_c denote the uniaxial stress and strain of the two-phase composite, respectively. To relate the constitutive curves of the two phases, an additional parameter Q is introduced to the TTO model.

$$Q = \frac{\sigma_1 - \sigma_2}{\varepsilon_2 - \varepsilon_1} \quad (4.8)$$

The parameter Q shows the ratio of stress to strain transfer. Large Q values correspond to the iso-strain condition and small Q values approach the iso-stress condition. The value of Q needs to be found by comparing with experimental results and depends upon numerous factors including compositions, flow stress ratio and strain hardening of the constituent phases, their microstructural arrangement and the applied strain. The constitutive law of an FGM can be obtained by relating the constitutive curves of the constituent materials through parameter Q at any fixed strain rate, as shown in Figure 4.5.

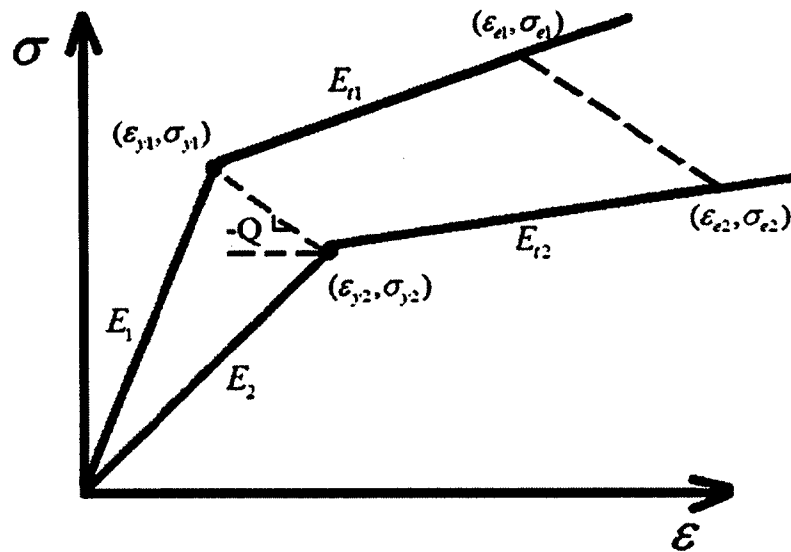


Figure 4.5 Concept of modified rule of mixture at a fixed strain rate

The Q value is assumed to uniquely define the boundary between elastic and plastic stress-strain curves at a fixed strain rate. The material parameters of constituent materials used are shown in Table 4.1.

Table 4.1 Material parameters for constituent materials

Material	Young's Modulus	Yield Point	Tangent Modulus	Plastic Hardening Model
1	E_1	$(\varepsilon_{y1}, \sigma_{y1})$	E_{t1}	$\varepsilon_1 = \sigma_{y1} + E_{t1} \varepsilon^{pl}$
2	E_2	$(\varepsilon_{y2}, \sigma_{y2})$	E_{t2}	$\varepsilon_2 = \sigma_{y2} + E_{t2} \varepsilon^{pl}$

Jin et al. [82] calculated the FGM property by TTO model with a power-law hardening model for the ductile constituent material and investigated the effect of parameter Q. From Jin's work, the TTO model is not sensitive to the parameter Q. In this work, the parameter Q value is uniquely defined by the yielding points of ductile constituent materials as:

$$Q = \frac{\sigma_{y1} - \sigma_{y2}}{\varepsilon_{y2} - \varepsilon_{y1}} \quad (4.9)$$

The volume fractions of the constituent materials are assumed to change linearly with respect to the coordinates of material calculation points in the thickness direction. The elastic-plastic material properties of FGM are derived in what follows.

1) Linear elastic region

The effective Young's modulus for a FGM is obtained by $E = \frac{\sigma_c}{\varepsilon_c}$. In the elastic

region, the stress-strain relations of the constituent materials follow:

$$\sigma_i = E_i \varepsilon_i, (i = 1, 2) \quad (4.10)$$

Substituting Eq. (4.7) and (4.10) into the effective Young's modulus equation, the Young's modulus of FGM can be expressed by strains of constituent materials.

$$E = \frac{V_1\sigma_1 + V_2\sigma_2}{V_1\varepsilon_1 + V_2\varepsilon_2} = \frac{V_1E_1\varepsilon_1 + V_2E_2\varepsilon_2}{V_1\varepsilon_1 + V_2\varepsilon_2} \quad (4.11)$$

Substituting Eq. (4.10) into Eq. (4.8), the parameter Q can be rewritten in terms of strains,

$$Q = \frac{\sigma_1 - \sigma_2}{\varepsilon_2 - \varepsilon_1} = \frac{E_1\varepsilon_1 - E_2\varepsilon_2}{\varepsilon_2 - \varepsilon_1} \quad (4.12)$$

Reorganizing the above Eq.(4.12), the relation between strains of constituent materials is given by

$$\frac{\varepsilon_2}{\varepsilon_1} = \frac{Q + E_1}{Q + E_2} \quad (4.13)$$

Then substituting Eq. (4.13) into Eq. (4.11), the effective Young's modulus of FGM is obtained,

$$E = [V_2E_2 \frac{Q + E_1}{Q + E_2} + V_1E_1] / [V_2 \frac{Q + E_1}{Q + E_2} + V_1] \quad (4.14)$$

2) At yield point

The parameter Q is selected based on the yield points of the constituent materials as shown in Eq. (4.9), these two constituent materials reach their yield points as well. The relation between the stress and strain for each constituent material at the yield point still follows Eq. (4.10). The yield stress and strain of a FGM can be expressed as

$$\sigma_y = V_1\sigma_{y1} + V_2\sigma_{y2}, \quad \varepsilon_y = V_1\varepsilon_{y1} + V_2\varepsilon_{y2} \quad (4.15)$$

3) Plastic region

Every point in the constitutive curve of material 1 is related to one specific point in the constitutive curve of material 2 through the slope $-Q$, as shown in Figure 4.5. When the material behaves inelastically, the stress-strain relation is assumed to follow the bilinear hardening curve. For a point in material 2 $(\varepsilon_{e2}, \sigma_{e2})$, its corresponding point in material 1 $(\varepsilon_{e1}, \sigma_{e1})$ can be found by substituting the bilinear hardening model,

$$Q(\varepsilon_{e2} - \varepsilon_{e1}) = \sigma_{e1} - \sigma_{e2} = \sigma_{y1} + E_{t1}(\varepsilon_{e1} - \varepsilon_{y1}) - \sigma_{e2} \quad (4.16)$$

The corresponding point along material 1 is

$$\varepsilon_{e1} = \frac{Q\varepsilon_{e2} - \sigma_{y1} + E_{t1}\varepsilon_{y1} + \sigma_{e2}}{Q + E_{t1}}, \quad \sigma_{e1} = \sigma_{y1} + E_{t1}(\varepsilon_{e1} - \varepsilon_{y1}) \quad (4.17)$$

Then corresponding point along the constitutive curve of a FGM can be found by

$$\sigma_e = V_1\sigma_{e1} + V_2\sigma_{e2}, \quad \varepsilon_e = V_1\varepsilon_{e1} + V_2\varepsilon_{e2} \quad (4.18)$$

And the tangent modulus of the FGM can be calculated based on Eq. (4.18),

$$E_T = \frac{\sigma_e - \sigma_y}{\varepsilon_e - \varepsilon_y} \quad (4.19)$$

4.2.5. VUMAT implementation of rate-dependent FGM model

The VUMAT subroutine in ABAQUS/Explicit and UMAT subroutine in ABAQUS/Standard provide interfaces to define the elastic-plastic material model and

leave more freedom to users. Different from the UMAT subroutine, the VUMAT subroutine is called for blocks of material calculation points and there is no need to update the Jacobian matrix in the explicit integration scheme [52].

A schematic of the VUMAT subroutine and its implementation into ABAQUS are shown in Figure 4.6. It is written based on the J_2 flow theory with isotropic hardening model. The subroutine is able to read material parameters of constituent materials and calculate material properties of the FGM at each material point based on the modified rule of mixture.

At the beginning of the finite element simulation, material constitutive models of constituent materials are constructed from the VUMAT inputs. In following steps, the volume fractions at material calculation points and the constitutive models of constituent materials are exported to the hardening subroutine VUHARD, and the material properties of FGM at each material calculation point will be calculated. In each analysis step, the material is considered to be purely elastic and the trial elastic stresses are calculated at first. Then the von Mises stress can be calculated by trial elastic stresses and used to judge whether the material yields or not. If it doesn't yield, the trial elastic stresses are the true stresses and the analysis continues to the next step. If it yields, the equivalent plastic strain is updated according to the von Mises stress by Newton-Raphson iteration method. Once the equivalent plastic strain is found, the stresses and strains will be updated based on the J_2 flow theory.

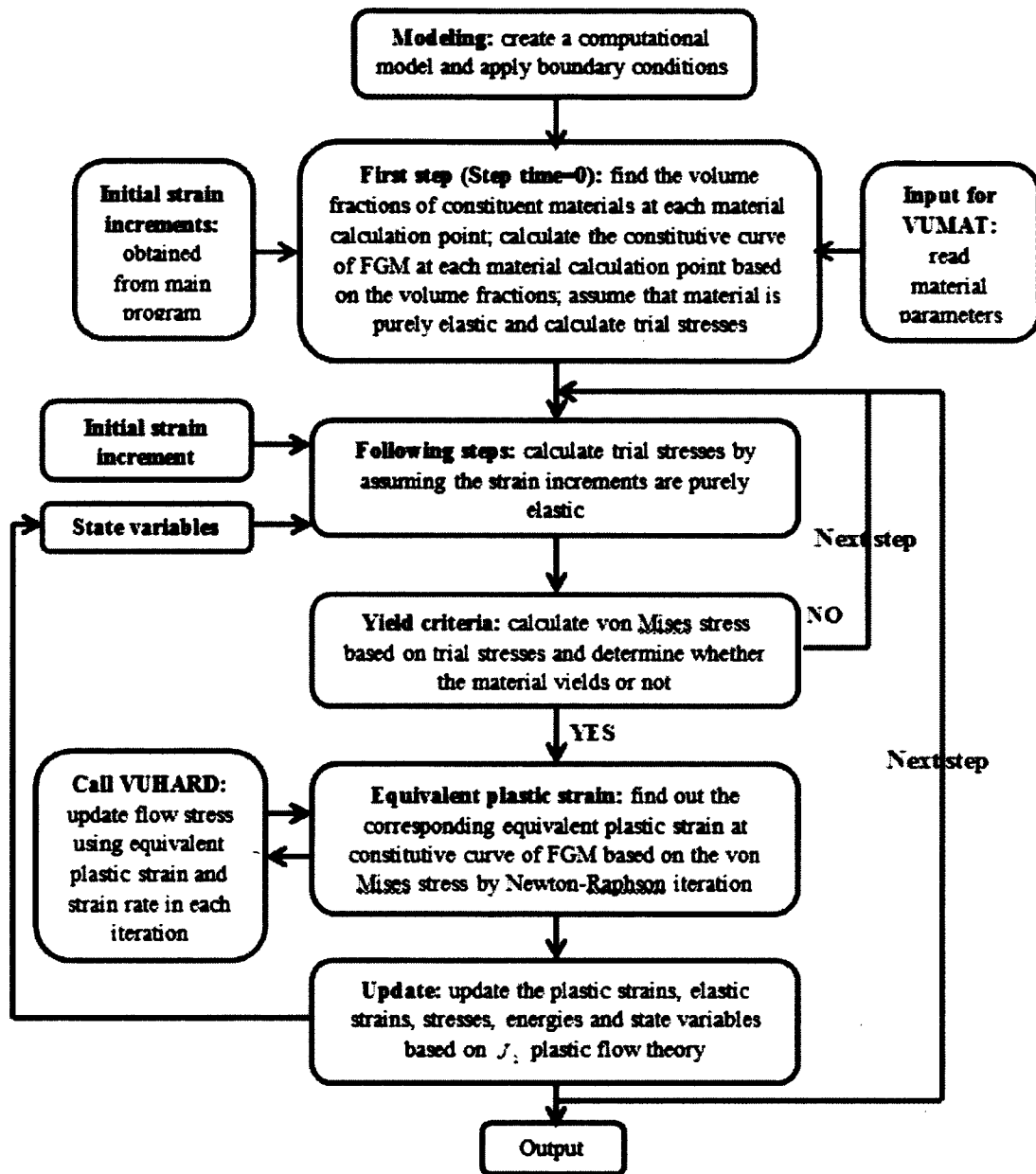


Figure 4.6 Flow chart of VUMAT implementation in ABAQUS

4.3 Shock tube testing on dynamic response of a monolithic plate

The shock tube testing was carried out on a monolithic plate made of steel 1018. The shock tube facility available at the University of Rhode Island (Prof. Arun Shukla)

[44-46] is used in this study to generate the dynamic air pressure loads. The shock tube is divided into a high-pressure driver section and a low-pressure driven section, which are separated by a destructible diaphragm. The pressure difference between these two sections becomes higher when pressurizing the high-pressure driver section. When the pressure difference reaches a critical value, the diaphragm ruptures and the resulting rapid release of gas forms a one-dimensional shock wave front. When the shock wave reaches the specimen, the dynamic air pressure load is applied to the specimen.

The dynamic air pressure load generated by the shock tube is measured by the sensor which is mounted 20mm away from the nozzle as shown in Figure 4.7. The dynamic air pressure load has an exponential decay behavior, which is typical for blast loading. The plate is simply supported and located with zero stand-off distance from the nozzle, as shown in Figure 4.7(b). The size of the plate is 0.203m (8in.) in length, 0.0508m (2in.) in width and 0.003m (0.125in.) in thickness. The span between the two supports is around 0.152m (6in.). From the shock tube testing, the time history of the monolithic plate deformation was obtained by a high-speed camera system as shown in Figure 4.8. During the testing, the rectangular monolithic plate bent to its largest deformation of 14.67mm under the dynamic air pressure load at 2.5ms, and then oscillated until it reached its stable permanent plastic deformation state.

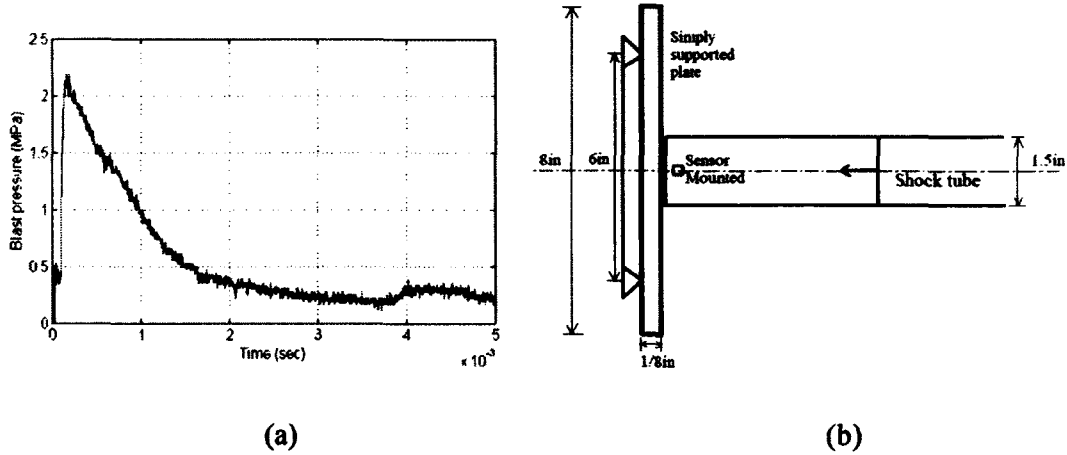


Figure 4.7 (a) Dynamic air pressure load generated by the shock tube; (b) shock tube testing setup

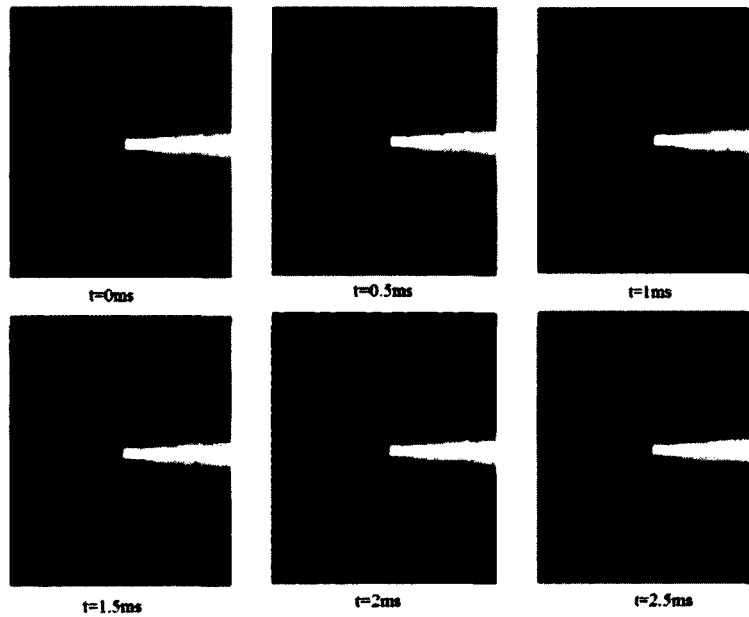


Figure 4.8 Deformation history of Steel 1018 plate during shock tube testing

4.4 Dynamic finite element modeling

Identical finite element meshes were used for monolithic plate and FGM plate as shown in Figure 4.9. Due to model symmetry, a quarter model was built to reduce computational time. Contact with frictionless tangential behavior and hard normal behavior is defined to simulate the simple support between the specimen and the rigid support. The model is meshed using the first-order C3D8I incompatible element, which is the first-order fully integrated C3D8 element enhanced by incompatible modes to improve its bending behavior [83]. The formulation of the first-order fully integrated elements leads to extra shear strain in bending, which is called parasitic shear. The incompatible elements can not only improve the bending analysis but can also reduce the computational time compared to second-order elements. Due to the high rate dynamic air pressure loading during shock tube testing, the explicit algorithm is selected and its stability is guaranteed in this simulation.

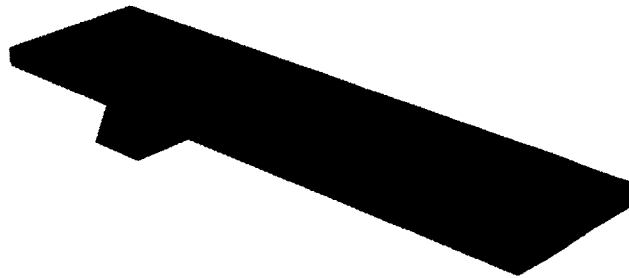


Figure 4.9 3D Finite element mesh for both monolithic and FGM plates (No. of Elements: 24576; No. of Nodes: 29961).

Due to the fluid-structure interaction, it is very challenging to determine the spatial distribution of the pressure loading at each time increment from the shock tube experiment. We observe that when the plate undergoes large deformation, the actual

loading area is extended to beyond the muzzle area and the pressure loading at the extended area decays as it moves outward from the shock tube muzzle (see the paper [56] for more information). In this paper, we do not perform fluid-structure analysis but approximate the pressure load history which may be able fit such interaction. In this work, the radius of the loading area is extended from 0.75in (radius of muzzle) to 1.5in, shown in Figure 4.10. The pressure load at the muzzle area is approximately the same as the measured pressure loading, as shown in Figure 4.7(a). And the pressure load in the extended area is assumed to have a second-order decay behavior.

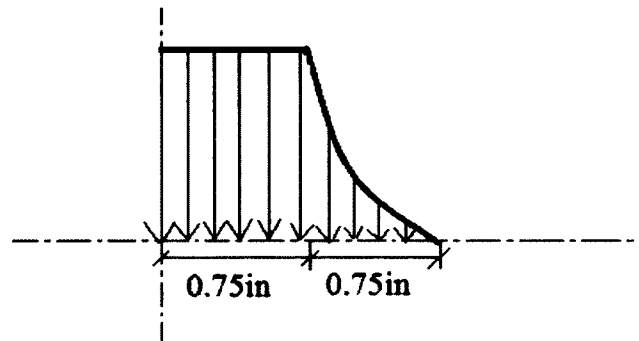


Figure 4.10 Spatial distribution of the dynamic air pressure loading

The simulation of Steel 1018 is carried out with material property implemented by the developed VUMAT subroutine and existed bilinear plastic model in ABAQUS/CAE. So the user subroutine can be validated by comparing the simulation results with the shock tube testing data and with existing material models in ABAQUS/CAE. Then the dynamic behavior of an FG plate under dynamic air pressure loading is investigated. As a comparative study, simulations of three monolithic plate models made of steel 1018, steel A36 and effective material are also carried out. The effective material property is calculated by considering the averaged material

property of steel 1018 and A36. In other words, the effective material is made of uniformly distributed, 50% steel 1018 and 50% steel A36. The material models are all implemented in the VUMAT subroutine by changing the volume fractions of steel 1018 and steel A36.

Besides, the damping in dynamic finite element simulations is very important. There are a number of built-in damping options available in ABAQUS: material damping, modal damping, structural damping and bulk viscosity. According to the analysis type, the bulk viscosity and material damping may be implemented. In ABAQUS/Explicit, bulk viscosity is introduced to control high frequency oscillations [52]. Since oscillations at high frequencies are not obvious in our model, the default values of bulk viscosity are implemented. For the material damping, since the elastic-plastic material behavior is defined, there is no need to introduce additional material damping. The reason is that material damping is often insignificant when compared to the plastic dissipative effect, since the energy is mainly dissipated in the form of plastic deformation.

4.5 Finite element results and discussion

4.5.1 Dynamic response of Steel 1018

The displacement history of the center point of the monolithic plate (steel 1018) obtained from finite element simulation is compared with shock tube experimental data in Figure 4.11. The displacement obtained from simulation with developed user subroutine matches very well with that with existing bilinear model in ABAQUS/CAE. The maximum deflection from the simulation is 14.33mm which happens around 1.6ms and the maximum deformation from the shock tube test is

found to be 14.67mm which occurs around 2.5ms. The finite element simulations provide reasonably good comparison with the experiment results. The difference between simulation and test results may be mainly due to the fluid-structure interaction and somewhat due to contact conditions at the supports. As it can be seen from testing (see Figure 4.8) that the bonding was destroyed and left more freedom to the specimen; however, the specimen is assumed to be bonded to the support by wire.

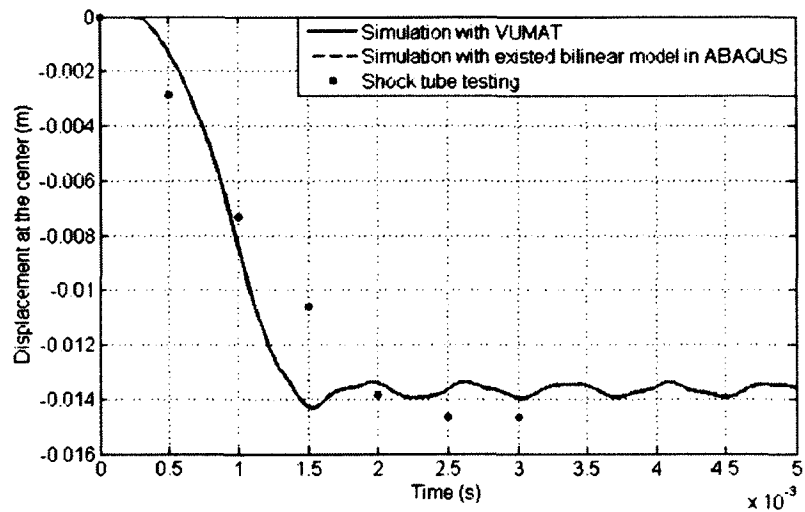


Figure 4.11 Comparison of displacement histories of the center point in Steel 1018 plate

Comparison of energy quantities can provide the relative contribution of each energy quantity to the system. Energy balance must be kept during the ABAQUS/Explicit analysis and indicates whether the analysis is stable. In this model, the energy balance can be written as

$$E_{total} = E_I + E_V + E_{KE} - E_W - E_{PW} - E_{CW} = const \quad (4.20)$$

where E_I is the internal energy, E_V is the viscous energy dissipated, E_{KE} is the kinetic energy, E_W is the work done by the externally applied loads, E_{PW} is the work done by contact penalties and E_{CW} is the work by constraint penalties. Theoretically, the total energy E_{total} should be constant. But due to the computational procedure, variation of E_{total} within 1% is accepted and expected [52]. In this work, all the simulations keep the energy balance.

The internal energy is a summation of the elastic strain energy E_E , the plastic dissipation E_P and the artificial strain energy E_A ,

$$E_I = E_E + E_P + E_A \quad (4.21)$$

The energy quantities of the monolithic plate are shown in Figure 4.12. The external work is determined by integrating the product of load and the displacement for the entire finite element model. The external work increases until the plate bends to its maximum deformation, and then vibrates while the plate oscillates until it reaches its permanent deflection. The plastic dissipation accumulates starting from 0.6ms and the plastic dissipation increments become smaller as the dynamic air pressure load decays. When the plastic dissipation increases, the kinematic energy decreases correspondingly.

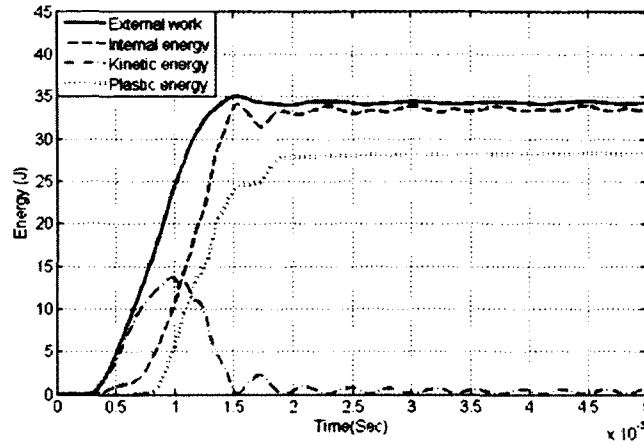


Figure 4.12 Energy histories of a monolithic plate (steel 1018) subjected to dynamic air pressure load

4.5.2 Dynamic response of functionally graded plate

As mentioned before, the FGM plate is simulated and compared with results of monolithic plates with steel 1018, steel A36 and effective material. The displacement histories at these plate centers are plotted in Figure 4.13. As expected, the monolithic plate with steel A36 has the largest deformation (maximum 17.71mm) at the center, which is due to its lower strain hardening property. The monolithic plate made of steel 1018 has the smallest deformation (maximum 14.33mm) at the center. The displacements of the effective material and the FGM are slightly larger than that of steel 1018, but much smaller than that of steel A36. The maximum displacement at the center of the monolithic plate with effective material property is 15.82mm, while the maximum displacement of the FGM plate is 15.34mm. With the same overall volume fractions of constituent materials, the deformation of the FGM plate is smaller than that of monolithic plate with the effective material property.

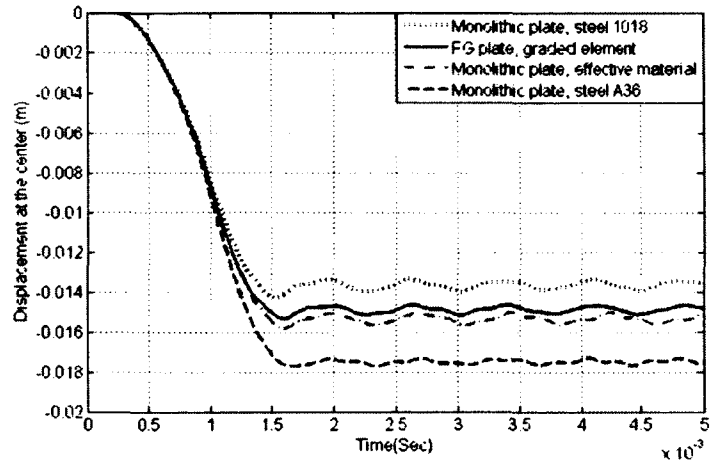
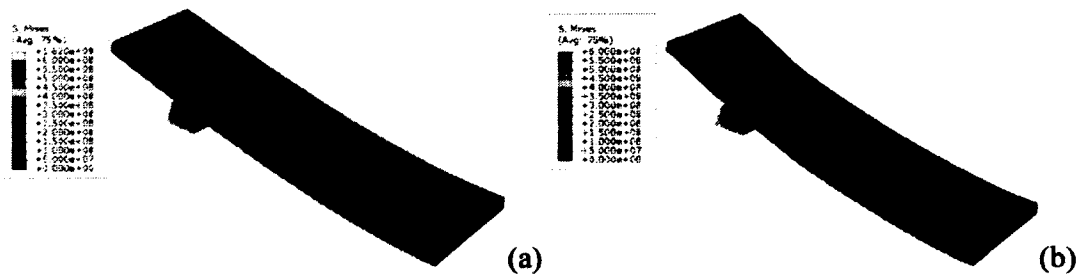


Figure 4.13 Displacement histories for the center point of four material configurations.

All are the FEM results.

Figure 4.14 shows the von Mises stress contours for the material sets at the time of maximum deformation. We observe that Steel A36 experiences largest deformations (See Figure 4.13) among the four material sets, but possesses least stresses due to its lowest strain hardening behavior, and vice versa for Steel 1018. As expected, we also see that the stresses in the FG plate and the effective plate are in between Steel 1018 and A36.



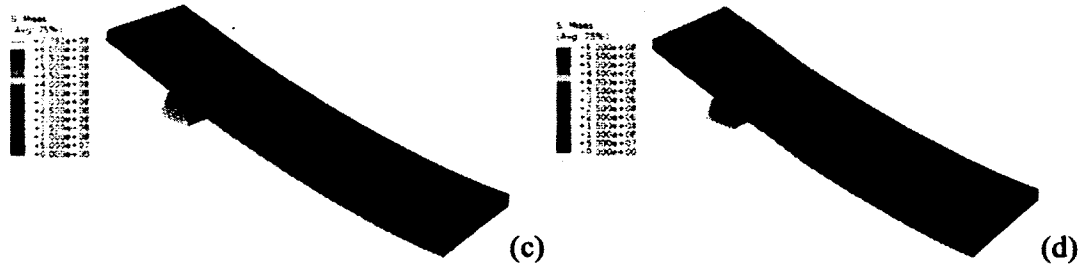


Figure 4.14 Von Mises stress contours at the time of maximum deformation: (a) Steel 1018 plate at 1.54ms; (b) Steel A36 plate at 1.66ms; (c) FG plate at 1.60ms; (d) Plate with effective material at 1.60ms

Figure 4.15 shows the time histories of von Mises stresses at the center of the front (facing the loading) face and the center of the back face for the four material sets. For the monolithic plates, the von Mises stresses at the center of front and back faces have similar magnitudes. Steel A36 has the smallest, and Steel 1018 has the largest, and as expected, the stress magnitude of monolithic plate with effective property is in between. The von Mises stresses in the FG plate vary with the location due to material gradation. Material gradation reflects the behavior of each constituent material, For example, the stress on the front face of the FG plate follows the path of Steel A36 that is placed on top region, and the stress on the back face of the FG plate follows Steel 1018 placed on back region.

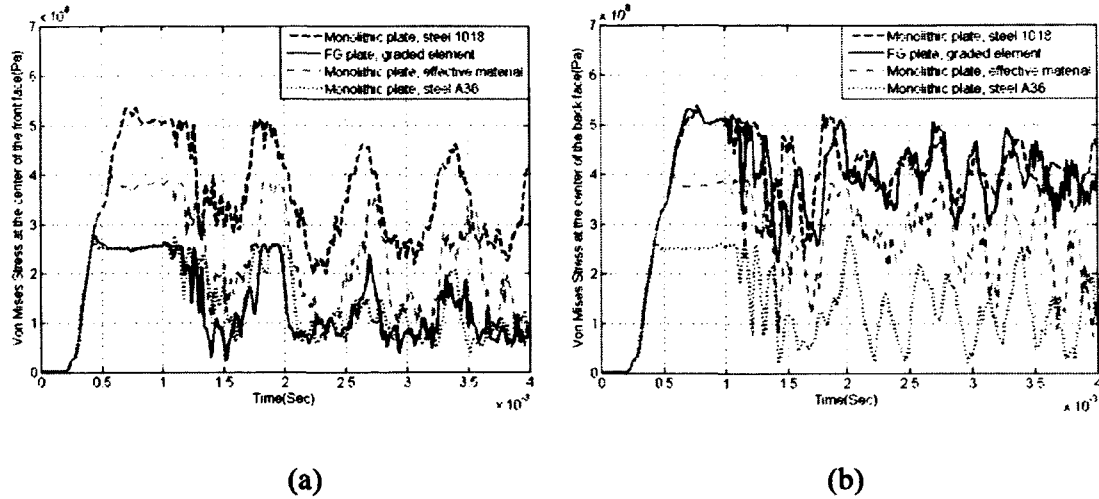


Figure 4.15 Time histories of von Mises stresses at the center of (a) front face and (b) back face

Figure 4.16(a) shows external work history. The external work increases till the plate bends to its maximum displacement and oscillates little bit when the plate bounces back and forth until its permanent deflection. The external work is largest in Steel A36, and smallest in Steel A36, and in between in the FGM and the effective plate. The external work for the FGM plate is smaller than that for the effective plate. Similar behavior is observed for the internal energy history plots in Figure 4.16(b). Figure 4.16(c) shows kinetic energy history. The kinetic energy of a monolithic plate with steel A36 is the largest, while that of plate with steel 1018 is the smallest. Figure 4.16(d) shows plastic dissipation history. The plastic dissipation increments decay as the magnitude of dynamic pressure load decays with time. The plastic dissipation of a monolithic plate with steel A36 is the largest, while that for the monolithic plate with steel 1018 is the smallest. The plastic dissipation of plate with FGM is smaller than that of a plate with an effective material.

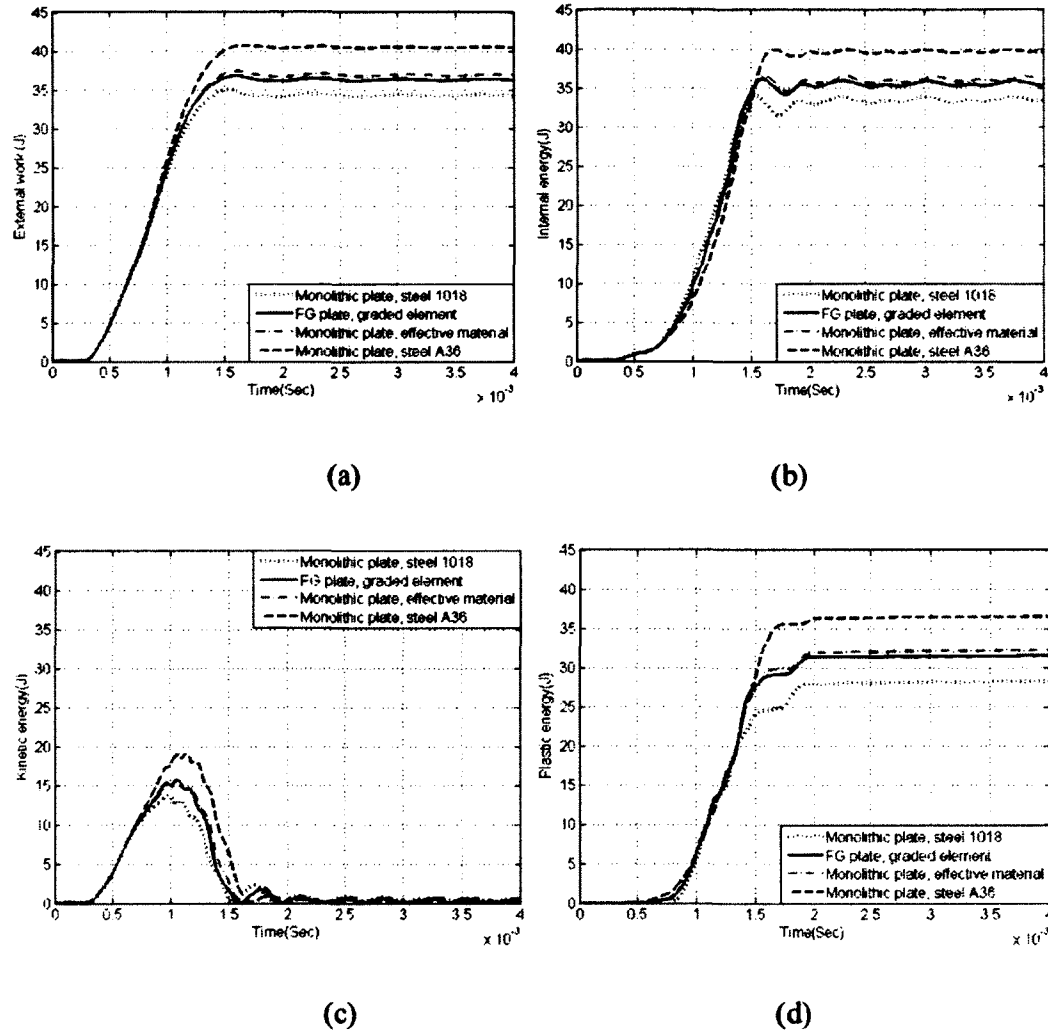


Figure 4.16 Energy histories of plates with four material models: (a) External work (b) Internal energy (c) Kinetic energy (d) Plastic dissipation.

4.6 Concluding remarks

This paper addresses the development of rate-dependent constitutive model of FGM from the constitutive models of constituent materials based on the modified rule of mixture. The FGM considered is composed with two ductile constituent materials (steel 1018 and steel A36) with linear gradation along its thickness direction. And, the

linear strain-rate dependence and bilinear hardening model are used for the constituent materials. Based on the developed rate-dependent elastic-plastic model for FGM, a VUMAT subroutine is developed and implemented in the finite element simulation on the dynamic response of FGM plate subjected to dynamic air pressure load which is generated by shock tube facility.

The displacement history, stress histories at critical locations and energy histories of the FGM plate obtained from the finite element simulation are well compared with monolithic plates with various material sets (constituent materials and effective material). The displacement and energy plots of FGM plate are between those plots of monolithic plates which are made of constituent materials (steel 1018 and steel A36). With the same overall volume fractions of constituent materials, the displacement and energies of FGM plate are smaller than those of plate with effective material property. To provide validation data, the comparison between experimental and computational results of monolithic plate (steel 1018) under dynamic air pressure loads are carried out as well. The developed modeling procedure is limited to an FGM with two ductile materials. And fluid-structure interaction is not considered and will be pursued in the future. The advantage of FGM upon the advancement of the technology to manufacture and realize its applications is to make dissimilar materials more compatible, optimize the dynamic response of the system [84], e.g. dissipate more energy and reduce the displacement, etc.

Chapter 5 – Conclusions and Future Work

This work mainly focuses on the dynamic responses of sandwich structures with various core arrangements subjected to blast loading. In this work, the dynamic responses of corrugated sandwich plates with various homogeneous and graded core arrangements under shock tube loading are investigated by finite element method. Based on the comparison of the maximum back face deflection, maximum back face velocity, plastic energy absorption, stress histories and contact force, the corrugated sandwich plate with the gradually graded core has a better overall performance.

A parametric study on unit-cell corrugated and trapezoid sandwich structures with given mass and various core arrangements subjected to idealized air-blast loading is also carried out. We find that the sandwich structures with graded cores can prevent the structure to get fully crushed. It is also shown that the trapezoid sandwich structures have larger impact tolerance, but the trapezoid sandwich structures are more sensitive to the initial geometric imperfections than corrugated sandwich structures.

Due to the benefits of the graded cores, a modified rule of mixture and linear strain-rate dependence are used to derive the rate-dependent elastic-plastic constitutive relations for functionally graded (FG) material. The derived constitutive relations are implemented in ABAQUS/Explicit through a VUMAT subroutine to investigate the dynamic response of a FG plate subjected to shock tube loading.

The future work includes the fluid-structure coupling simulation about the shock tube testing and further optimization of the sandwich structures.

Appendix – Functionally Graded Material Composed of Two Ductile Constituent Materials with Power-law Strain Hardening Model

The strain-rate dependence in this work is treated separately from quasi-static stress-strain relations. The quasi-static elastic-plastic material parameters for FGM at each material calculation point are derived based on the constitutive relations of constituent materials using a modified rule of mixture. In Chapter 4, the constituent materials have bilinear strain hardening model. In the appendix, the constituent materials follow power-law strain hardening model in the plastic region.

The TTO model relates the uniaxial stress and strain of a two-phase composite to the corresponding uniaxial stresses and strains of two constituent materials by [72]

$$\sigma_c = V_1\sigma_1 + V_2\sigma_2, \varepsilon_c = V_1\varepsilon_1 + V_2\varepsilon_2 \quad (\text{A.1})$$

where σ_i , ε_i and V_i ($i=1,2$) denote the average stresses, average strains and volume fractions of the constituent phases, respectively. σ_c and ε_c denote the uniaxial stress and strain of the two-phase composite, respectively.

To relate the constitutive curves of the two phases, an additional parameter Q is introduced to the TTO model [72].

$$Q = \frac{\sigma_1 - \sigma_2}{\varepsilon_2 - \varepsilon_1} \quad (\text{A.2})$$

The parameter Q shows the ratio of stress to strain transfer. The constitutive curve of a FGM can be obtained by relating the constitutive curves of the constituent materials through parameter Q , as shown in Figure A.1.

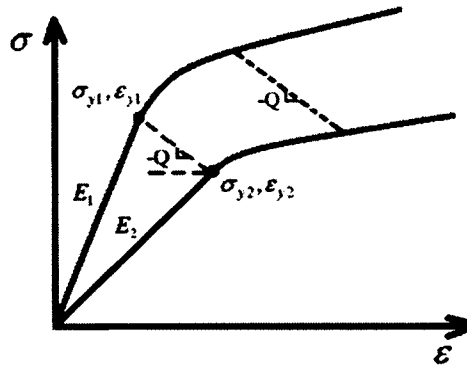


Figure A.1 Concept of modified rule of mixture

In this work, the TTO model is applied to calculate the material properties of a FGM which is composed of two ductile constituent materials with power-law strain hardening model. The material parameters of constituent materials are denoted in Table A.1. Different from the ceramic-metal FGM, the Q value here uniquely defines the boundary between linear and nonlinear stress-strain curves. In this work, the parameter Q value is uniquely defined by the yielding points of ductile constituent materials as:

$$Q = \frac{\sigma_{y1} - \sigma_{y2}}{\epsilon_{y2} - \epsilon_{y1}} \quad (\text{A.3})$$

Table A.1. Material parameters for constituent materials

Material	Young's Modulus	Yield Point	Plastic Hardening Model
1	E_1	$(\varepsilon_{y1}, \sigma_{y1})$	$\varepsilon_1 = \varepsilon_{y1} \left(\frac{\sigma_1}{\sigma_{y1}} \right)^{n_1}$
2	E_2	$(\varepsilon_{y2}, \sigma_{y2})$	$\varepsilon_2 = \varepsilon_{y2} \left(\frac{\sigma_2}{\sigma_{y2}} \right)^{n_2}$

The volume fractions of the constituent materials are assumed to change linearly with respect to the coordinates of material calculation points in the thickness direction. In what follows, the elastic-plastic material properties of FGM are derived.

1) The linear elastic region

The effective Young's modulus for a FGM is obtained by $E = \frac{\sigma_c}{\varepsilon_c}$. In the elastic region,

the stress-strain relations of the constituent materials follow:

$$\sigma_i = E_i \varepsilon_i, (i = 1, 2) \quad (A.4)$$

Substituting Eq. (A.1) and (A.4) into the effective Young's modulus equation, the Young's modulus of FGM can be expressed by strains of constituent materials.

$$E = \frac{V_1 \sigma_1 + V_2 \sigma_2}{V_1 \varepsilon_1 + V_2 \varepsilon_2} = \frac{V_1 E_1 \varepsilon_1 + V_2 E_2 \varepsilon_2}{V_1 \varepsilon_1 + V_2 \varepsilon_2} \quad (A.5)$$

Substituting Eq. (A.4) into Eq. (A.2), the parameter Q can be rewritten in terms of strains,

$$Q = \frac{\sigma_1 - \sigma_2}{\varepsilon_2 - \varepsilon_1} = \frac{E_1 \varepsilon_1 - E_2 \varepsilon_2}{\varepsilon_2 - \varepsilon_1} \quad (\text{A.6})$$

Reorganizing the above Eq. (A.6), the relation between strains of constituent materials is given by

$$\frac{\varepsilon_2}{\varepsilon_1} = \frac{Q + E_1}{Q + E_2} \quad (\text{A.7})$$

Then substituting Eq. (A.7) into Eq. (A.5), the effective Young's modulus of FGM is obtained,

$$E = [V_2 E_2 \frac{Q + E_1}{Q + E_2} + V_1 E_1] / [V_2 \frac{Q + E_1}{Q + E_2} + V_1] \quad (\text{A.8})$$

2) Yield point

Since the parameter Q is selected based on the yield points of the constituent materials as shown in Eq. (A.3), when the FGM reaches its yield point, these two constituent materials reach their yield points as well. The relation between the stress and strain for each constituent material at the yield point still follows Eq. (A.4). The yield stress and strain of a FGM can be expressed as

$$\sigma_y = V_1 \sigma_{y1} + V_2 \sigma_{y2}, \quad \varepsilon_y = V_1 \varepsilon_{y1} + V_2 \varepsilon_{y2} \quad (\text{A.9})$$

3) The plastic region

Every point in the constitutive curve of material 1 is related to one specific point in the constitutive curve of material 2 through the slope $-Q$, as shown in Figure A.1. When the

material behaves inelastically, the stress-strain relation follows the power-law hardening curve. Substituting the power-law hardening model of these two materials into Eq. (A.2), we get:

$$\sigma_1 - \sigma_2 = Q(\varepsilon_2 - \varepsilon_1) = Q \left[\varepsilon_{y2} \left(\frac{\sigma_2}{\sigma_{y2}} \right)^{n_2} - \varepsilon_{y1} \left(\frac{\sigma_1}{\sigma_{y1}} \right)^{n_1} \right] \quad (\text{A.10})$$

Reorganizing Eq. (A.10), the relation between the stresses of the constituent materials can be shown as

$$\sigma_1 + Q\varepsilon_{y1} \left(\frac{\sigma_1}{\sigma_{y1}} \right)^{n_1} = \sigma_2 + Q\varepsilon_{y2} \left(\frac{\sigma_2}{\sigma_{y2}} \right)^{n_2} \quad (\text{A.11})$$

To calculate the constitutive model of FGM, points along the constitutive curve of one phase (for example, material 2) are selected at fixed interval. Each given point along the constitutive curve of material 2 has its corresponding point along the constitutive curve of material 1. For example, given the number k -th point along the constitutive curve of material 2 ($\varepsilon_{2k}, \sigma_{2k}$), the corresponding number k -th point along the constitutive curve of material 1 can be found through

$$\sigma_{1k} + Q\varepsilon_{y1} \left(\frac{\sigma_{1k}}{\sigma_{y1}} \right)^{n_1} = \sigma_{2k} + Q\varepsilon_{y2} \left(\frac{\sigma_{2k}}{\sigma_{y2}} \right)^{n_2} \quad (\text{A.12})$$

Eq. (A.12) can be solved by Newton-Raphson iteration method. Then the corresponding point along the constitutive curve of a FGM can be found by

$$\sigma_k = V_1\sigma_{1k} + V_2\sigma_{2k}, \varepsilon_k = V_1\varepsilon_{1k} + V_2\varepsilon_{2k} \quad (\text{A.13})$$

When a sufficient number of points are calculated, a precise piecewise-linear constitutive model of the FGM can be obtained.

References

- [1] September 11 attacks. http://en.wikipedia.org/wiki/September_11_attacks, 2012.
- [2] The Visual Site Analysis Code. The Alfred E. Murrah Federal Building. <http://www.visac.ornl.gov/HelpFiles/nse2004/okcity3.jpg>, 2007. Oak Ridge National Laboratory.
- [3] E. Sciolino. Bombings in Madrid: the attack; 10 bombs shatter trains in Madrid, killing 192. *The New York Times*, March 12, 2004.
- [4] A. Cowell. Subway and bus blasts in London kill at least 37. *The New York Times*, July 08, 2005.
- [5] USS Cole bombing. http://en.wikipedia.org/wiki/USS_Cole_bombing, 2012.
- [6] C.W. Lampson. The blast and radiation from an atomic bomb. *In Proceedings of the Conference on Building in the Atomic Age*. Department of Civil and Sanitary Engineering, Massachusetts Institute of Technology, 1952.
- [7] P. Smith and J. Hetherington. *Blast and ballistic loading of structures*. Butterworth Heinemann, 1994.
- [8] N. Kambouchev. Analysis of blast mitigation strategies exploiting fluid-structure interaction. PhD dissertation. Massachusetts Institute of Technology, 2007.
- [9] J.D. Anderson. *Fundamentals of aerodynamics*, 3rd edition. McGraw-Hill Science/Engineering/Math, 1984.
- [10] US Army, US Navy, US Air Force. Structures to resist the effects of accidental explosions. UFC 3-340-02, December 5, 2008.

- [11] G.I. Taylor. The formation of a blast wave by a very intense explosion. I. Theoretical discussion. *Proceedings of the Royal Society of London. Series A, Mathematical and Physical Sciences*, 201(1065):159-174, 1950.
- [12] G.I. Taylor. The formation of a blast wave by a very intense explosion. II. The atomic explosion of 1945. *Proceedings of the Royal Society of London. Series A, Mathematical and Physical Sciences*, 201 (1065): 175-186, 1950.
- [13] J. Neumann. The point source solution. *Blast waves*, Chapter 2, Los Alamos Scientific Laboratory of the University of California, Los Alamos, New Mexico, 1947.
- [14] G.G. Bach and J.H. Lee. Higher-order perturbation solutions for blast waves. *AIAA Journal*, 7(4): 742-744, 1969.
- [15] G.G. Bach and J.H. Lee. An analytical solution for blast waves. *AIAA journal*, 8:271-275, 1970.
- [16] S. Murata. New exact solution of the blast wave problem in gas dynamics. *Chaos, Solitons & Fractals*, 28:327-330, 2005.
- [17] H.L. Brode. Numerical solution of spherical blast waves. *Journal of Applied Physics*, 26(6): 766-775, 1955.
- [18] H.L. Brode. Blast wave from a spherical charge. *The Physics of Fluids*, 2(2), 217, 1958.
- [19] W.E. Baker. *Explosions in air*. University of Texas Press, Austin, Texas, 1973.
- [20] G. F. Kinney. *Explosive shocks in air*. MacMillan, New York, 1962.
- [21] N. Jones. *Structural impact*. Cambridge: Cambridge University Press: 1989.

- [22] G.I. Taylor. The pressure and impulse of submarine explosion waves on plates. In: G.K. Batchelor, editor. *The scientific papers of Sir Geoffrey Ingram Taylor. Vol. III: aerodynamics and the mechanics of projectiles and explosions*. Cambridge: Cambridge University Press: 287-303, 1963.
- [23] Z. Xue and J.W. Hutchinson. A comparative study of impulse-resistant metal sandwich plates. *International Journal of Impact Engineering*, 30: 1283-1305, 2004.
- [24] N. Kambouchev, L. Noels and R. Radovitzky. Nonlinear compressibility effects in fluid-structure interaction and their implications on the air-blast loading of structures. *Journal of Applied Physics*, 100, 2006.
- [25] American Society of Civil Engineers. The Pentagon Building Performance Report, 2003.
- [26] S.B. Smith. General reaction of buildings to atomic blast. In *Proceedings of the Conference on Buildings in the Atomic Age*. Department of Civil and Sanitary Engineering, MIT, 1952.
- [27] A.G. Hanssen, L. Enstock and M. Langseth. Close-range blast loading of aluminum foam panels. *International Journal of Impact Engineering*, 27(6): 593-618, July, 2002.
- [28] H.N.G. Wadley. Multifunctional periodic cellular metals. *Philosophical Transactions of the Royal Society, A, Mathematical Physical & Engineering Sciences*, 364, 31-68, 2006.
- [29] M.R. Amini, J.B. Isaacs and S. Nemat-Nasser. Effect of polyurea on the dynamic response of steel plates. *Proceedings of the 2006 SEM Annual Conference and Exposition on Experimental and Applied Mechanics*, St. Louis, MO, June 4-7, 2006.

- [30] K.P. Dharmasena, H.N.G. Wadley, Z. Xue, J.W. Hutchinson. Mechanical response of metallic honeycomb sandwich panel structures to high-intensity dynamic loading. *International Journal of Impact Engineering* 35 (9): 1063–1074, 2008.
- [31] C.C. Liang, M. Yang, P. Wu. Optimum design of metallic corrugated core sandwich panels subjected to blast loads. *Ocean Engineering*, 28: 825–861, 2001.
- [32] G.N. Nurick, G.S. Langdon, Y. Chi and N. Jacob. Behavior of sandwich panel subjected to intense air blast – Part 1: experiments. *Composite Structures*, 91(4): 433-441, 2009.
- [33] Z. Xue and J.W. Hutchinson. Preliminary assessment of sandwich plates subject to blast loads. *International Journal of Mechanical Sciences*, 45:687-705, 2003.
- [34] N.A. Fleck and V.S. Deshpande, The resistance of clamped sandwich beams to shock loading. *Journal of Applied Mechanics*, 71, March 2004.
- [35] H.J. Rathbun, D.D. Radford, Z. Xue, M.Y. He, J. Yang, V.S. Deshpande, N.A. Fleck, J.W. Hutchinson, F.W. Zok and A.G. Evans. Performance of metallic honeycomb-core sandwich beams under shock loading. *International Journal of Solids and Structures*, 43: 1746-1763, 2006.
- [36] G.J. McShane, D.D. Radford, V.S. Deshpande and N.A. Fleck. The response of clamped sandwich plates with lattice cores subjected to shock loading. *European Journal of Mechanics A/Solids*, 25: 215-229, 2006.
- [37] M.T. Tilbrook, V.S. Deshpande and N.A. Fleck. The impulsive response of sandwich beams: analytical and numerical investigation of regimes of behavior. *Journal of the Mechanics and Physics of Solids*, 54: 2242-2280, 2006.

- [38] Y. Liang, A.V. Spuskanyuk, S.E. Flores, D.R. Hayhurst, J.W. Hutchinson, R.M. McMeeking and A.G. Evans. The response of Metallic Sandwich Panels to Water Blast. *Journal of Applied Mechanics*, 74:81-99, Jan 2007.
- [39] D.D. Radford, G.J. McShane, V.S. Deshpande, and N.A. Fleck. The response of clamped sandwich plates with metallic foam cores to simulated blast loading. *International Journal of Solids and Structures*, 43(7-8): 2243-2259, 2006.
- [40] D.D. Radford, N.A. Fleck and V.S. Deshpande. The response of clamped sandwich beams subjected to shock loading. *International Journal of Impact Engineering*, 32(6): 968-987, 2006.
- [41] C. Wu, D.J. Oehlers, M. Rebentrost, J. Leach and A.S. Whittaker. Blast testing of ultra-high performance fibre and FRP-retrofitted concrete slabs. *Engineering Structures*, 31(9): 2060-2069, 2009.
- [42] C.A. Ross, M.R. Purcell and E.L. Jerome. Blast response of concrete beams and slabs externally reinforced with fiber reinforced plastics (FRP). In: *Proceedings of the XV structures congress*, 673, 1997.
- [43] L. Muzsynski and M. Purcell. Composite reinforcement to strengthen existing structures against air blast. *Journal of Composite for Construction*, 7(2), 93-97, 2003.
- [44] N. Gardner, E. Wang, P. Kumar, A. Shukla. Blast mitigation in a sandwich composite using graded core and polyurea interlayer. *Experimental Mechanics* 2011.
- [45] E. Wang, A. Shukla. Analytical and experimental evaluation of energies during shock wave loading. *International Journal of Impact Engineering*, 37:1188-1196, 2010.

- [46] A. Kidane, A. Shukla. Dynamic constitutive behavior of Ti/TiB FGM under thermo-mechanical loading. *Journal of Material Science*, 43: 2771–2777, 2008.
- [47] S.A. Tekalur, A. Shukla and K. Shivakumar. Blast resistance of polyurea based layered composite materials. *Composite Structures*, 84: 271-281, 2008.
- [48] A.F. Avila. Failure mode investigation of sandwich beams with functionally graded core. *Composite Structures*, 81: 323-330, 2007.
- [49] N.A. Apetre, B.V. Sankar and D.R. Ambur. Low-velocity impact response of sandwich beams with functionally graded core. *International Journal of Solids and Structures*, 43: 2479-2496, 2006.
- [50] E. Wang, N. Gardner and A. Shukla. The blast resistance of sandwich composites with stepwise graded cores. *International Journal of Solids and Structure*, 46:3492-3502, 2009.
- [51] N. Gardner and A. Shukla. The blast response of sandwich composites with a graded core: equivalent core layer mass vs. equivalent core layer thickness. *Conference Proceedings of the Society for Experimental Mechanics Series Dynamic Behavior of Materials*, 1(99): 281-288, 2011.
- [52] ABAQUS 6.9 Documentation.
- [53] J.T. Wright. Thermo-dynamic response of ASME A913 grade65 steel and graded, corrugated sandwich panels under shock loading. M.S. Thesis. University of Rhode Island, 2012.
- [54] U.S. Lindholm. Some experiments with the split Hopkinson pressure bar. *Journal of the Mechanics and Physics of Solids*, 12(5): 317-335, 1964.

- [55] Gama BA, Lopatnikov SL, Gillespie Jr JW. Hopkinson bar experimental technique: A critical review. *Applied Mechanics Reviews*, 57(4): 223-250, 2004.
- [56] P. Kumar, J. LeBlanc, D.S. Stargel and A. Shukla. Effect of plate curvature on blast response of aluminum panels. *International Journal of Impact Engineering*, 46: 74-85, 2012.
- [57] Z. Xue and J.W. Hutchinson. Crush dynamics of square honeycomb sandwich cores. *International Journal for Numerical Methods in Engineering*, 65: 2221-2245, 2006.
- [58] E. Ferri, V.S. Deshpande and A.G. Evans. The dynamic strength of a representative double layer prismatic core: a combined experimental, numerical, and analytical assessment. *Journal of Applied Mechanics*, 77, 2010.
- [59] R.H. Cole. Underwater explosions. Princeton: Princeton University Press, 1948.
- [60] G.R. Abrahamson and J.N. Goodier. Dynamic flexural buckling of rods within an axial plastic compression wave. *Journal of Applied Mechanics*, 33:241-247, 1966.
- [61] T. Hirai. Functionally gradient materials and nanocomposites. In: J.B. Holt, M. Koizumi, T. Hirai, Z.A. Munir (Eds.), *Proceedings of the Second International Symposium on Functionally Gradient Materials, Ceramic Transactions*. The American Ceramic Society, Westerville, Ohio, 34: 11–20, 1993.
- [62] B. Ilchner. Processing-microstructure–property relationships in graded materials. *Journal of the Mechanics and Physics of Solids*, 44(5): 647–656, 1996.
- [63] A.M. Zenkour. A comprehensive analysis of functionally graded sandwich plates: Part I- Deflection and stresses. *International Journal of Solids and Structures*, 42: 5224-5242, 2005.

- [64] L.F. Qian, R.C. Batra and L.M. Chen. Static and dynamic deformations of thick functionally graded elastic plates by using higher-order shear and normal deformable plate theory and meshless local Petrov–Galerkin method. *Composites: Part B Engineering*, 35(6-8): 685–697, 2004.
- [65] J. Yang and H.-S. Shen. Dynamic response of initially stressed functionally graded rectangular thin plates. *Composite Structures*, 54(4): 497-508, 2001.
- [66] X.-L. Huang and H.-S. Shen. Nonlinear vibration and dynamic response of functionally graded plates in thermal environments. *International Journal of Solids and Structures*, 41(9-10): 2403-2427, 2004.
- [67] J.N. Reddy. Analysis of functionally graded plates. *International Journal for Numerical Methods in Engineering*, 47(1-3): 663-684, 2000.
- [68] G.N. Praveen and J.N. Reddy. Nonlinear transient thermoelastic analysis of functionally graded ceramic-metal plates. *International Journal of Solids and Structures*, 35(33): 4457-4476, 1998.
- [69] J.N. Reddy and C.D. Chin. Thermomechanical analysis of functionally graded cylinders and plates. *Journal of Thermal Stresses*, 21(6): 593-626, 1998.
- [70] A. Chakraborty, S. Gopalakrishnan and J.N. Reddy. A new beam finite element for the analysis of functionally graded materials. *International Journal of Mechanical Sciences*, 45(3): 519-539, 2003.
- [71] R.L. Williamson, B.H. Rabin and J.T. Drake. Finite element analysis of thermal residual stresses at graded ceramic-metal interfaces. Part I. Model description and geometrical effects. *Journal of Applied Physics*, 74(2): 1310-1320, 1993.

- [72] I. Tamura, Y. Tomota and M. Ozawa. Strength and ductility of Fe-Ni-C alloys composed of austenite and martensite with various strengths. *The microstructure and design of alloys: proceedings of the third international conference on the strength of metals and alloys*, Cambridge, England, 1: 611-615, 1973.
- [73] A.E. Giannakopoulos, S. Suresh, M. Finot and M. Olsson. Elastoplastic analysis of thermal cycling layered materials with compositional gradients. *Acta Metal. Mater*, 43(4): 1335-1354, 1995.
- [74] R. Gunes, M. Aydin, M.K. Apalak and J.N. Reddy. The elasto-plastic impact analysis of functionally graded circular plates under low-velocities. *Composite Structures*, 93(2): 860-869, 2011.
- [75] Y. Li and K.T. Ramesh. Influence of particle volume fraction, shape and aspect ratio on the behavior of particle-reinforced metal-matrix composites at high rates of strain. *Acta Mater*, 46(16): 5633-5646, 1998.
- [76] Y. Li, K.T. Ramesh and E.S.C. Chin. Dynamic characterization of layered and graded structures under impulsive loading. *International Journal of Solids and Structures*, 38(34-35): 6045-6061, 2001.
- [77] Y. Li, K.T. Ramesh, E.S.C. Chin. The compressive viscoplastic response of an A359/SiCp metal matrix composite and of the A359 aluminum alloy matrix. *International Journal of Solids and Structures*, 37(51): 7547-7562, 2000.
- [78] G.R. Johnson and W.H. Cook. A constitutive model and data for metals subjected to large strains, high strain rates and high temperatures. *In: Proceedings of the 7th International Symposium on Ballistics*, The Hague, the Netherlands, 1-7, 1983.

- [79] G.R. Cowper and P.S. Symonds. Strain hardening and strain rate effect in the impact loading of cantilever beams. *Division of Applied Mathematics Report*, Brown University, No.28, 1957.
- [80] ASTM A36 steel material properties, MatWeb: <http://www.matweb.com>
- [81] J.-H. Kim and G.H. Paulino. Isoparametric graded finite elements for nonhomogeneous isotropic and orthotropic materials. *Journal of Applied Mechanics*, 69(4): 502-514, 2002.
- [82] Z.H. Jin, G.H. Paulino and R.H. Dodds. Cohesive fracture modeling of elastic–plastic crack growth in functionally graded materials. *Engineering Fracture Mechanics*, 70: 1885–1912, 2003.
- [83] R.D. Cook, D.S. Malkus, M.E. Plesha and R.J. Witt. *Concepts and Applications of Finite Element Analysis*, fourth ed., John Wiley & Sons, Inc., 2001.
- [84] G. Anandakumar and J.-H. Kim, “On the Modal Behavior of a Three-Dimensional Functionally Graded Cantilever Beam: Poisson’s ratio and Material Sampling Effects,” *Composite Structures*, 92:1358-1371, 2010.